Fall 2019

Deep understanding of degradation in lithium ion batteries through experimental and first-principles study

Yufang He

Department: Mechanical and Aerospace Engineering

DEEP UNDERSTANDING OF DEGRADATION IN LITHIUM ION BATTERIES THROUGH EXPERIMENTAL AND FIRST-PRINCIPLES STUDY

by

YUFANG HE

A DISSERTATION

Presented to the Faculty of the Graduate School of the

MISSOURI UNIVERSITY OF SCIENCE AND TECHNOLOGY

In Partial Fulfillment of the Requirements for the Degree

DOCTOR OF PHILOSOPHY

in

MECHANICAL ENGINEERING

2019

Approved by:

Jonghyun Park, Advisor
Jie Gao
Daoru Han
Xinhua Liang
Julia Medvedeva

PUBLICATION DISSERTATION OPTION

This dissertation consists of the following four articles that have been submitted for publication, or will be submitted for publication as follows:

Paper I: Pages 8-30 have been submitted to the *Journal of Physical Chemistry*.

Paper II: Pages 31-62 have been submitted to *Nature Communication*.

Paper III: Pages 63-88 are intended for submission to *ACS Applied Material & Interfaces.*

Paper IV: Pages 89-106 are intended for submission to *Electrochemica Acta*.

ABSTRACT

The growing interests in Lithium-ion Batteries (LIBs) have significantly accelerated the development of active materials. However, the key challenge is that electrode materials suffer from degradation, which include transition metal dissolution, solid electrolyte interphase (SEI) layer formation, and mechanical fracture. To address these issues, applying an ultrathin coating onto active materials via Atomic Layer Deposition (ALD) is an efficient way. Although numerious works have been done for active material performance improvement via ALD technology, the fundamental enhancement mechanisms of ALD coating on battery performance improvement are not yet known. Therefore, this dissertation consists of four papers, which focused on the ALD coating impact on Li intercalation, metal dissolution, Li ion diffusivity and interfacial property of SEI layer via first-principles study. Paper I explained why CeO_2 coating has better performance than Al_2O_3 coating material via faster Li diffusion, facile intercalation, and less mechanical damage of coating. Paper II discovered an unexpected metal dissolution that ultrathin CeO_2 coating intensifies the Mn dissolution of LMO and it was confirmed in several ways, including ICP-OES measurement, Mn vacancy formation energy calculation, COOP analysis, PDOS analysis, and cell level performance. Paper III revealed that the ALD CeO_2 coating thickness impact on Li ion diffusivity in coated LMO is related to surface and bulk diffusion domination and phase transition of coating layers. Paper IV demonstrated that the fracture strength of inorganic components of SEI layer was higher than organic component, implying that the inorganic-organic interface can effectively block electron transport from electrolyte to anode particles to prevent futher oxidation of active materials.

ACKNOWLEDGMENTS

First, I would like to thank my advisor, Dr. Jonghyun Park, who provides consistent invaluable support for my research. I deeply appreciate the great opportunities, wonderful working environment and all required resources offered by Dr. Park. It is my great honor to work with Dr. Park during the PhD study. I would like to express my sincere gratitude to all my committee members, Dr. Xinhua Liang, Dr. Jie Gao, Dr. Daoru Han, and Dr. Julia Medvedeva, for kindly offering suggestions and support for my research. I am very grateful to Hiep Pham and other colleagues. I also appreciate all my friends for their help and support during my PhD journey. Finally, I would like to appreciate my lovely family member my grandmother, Mulan Sun, my father, Jianhua He, my mother, Meihua Shi and my brother, Yuanfang He for their constant encouragement, support, and love.

TABLE OF CONTENTS

Page

LIST OF ILLUSTRATIONS

Page

PAPER I

PAPER II

PAPER IV

LIST OF TABLES

Page

PAPER I

PAPER II

PAPER III

SECTION

1. INTRODUCTION

Lithium ion batteries (LIBs) have attracted great attention as an advanced energy storage system due to its high energy density, high power density, and long cycle life. LIBs can be considered as the most successful story of modern electrochemistry in the last two decades, having found implementation in a wide range of applications from portable devices to the electric vehicle. LIB technology is advancing rapidly and, thus, an increasing number of researchers have focused on this field. Areas of LIB research are typically divided between its components, which consist of cathode, anode, separator, electrolyte solution and the current collector. The principle mechanism of LIB involves the movement of Li ions from the negative electrode (anode) to the positive electrode (cathode) during discharge, and back when charging. Therefore, a significant amount of research has focused on improving materials (predominantly in electrodes) to enhance Li ion mobility. Some widely researched anode intercalation materials are graphite, Si, and $Li_4Ti_5O_{12}$ (LTO), while the cathode materials include $LiCoO_2$, $LiFePO_4$, $LiMn_2O_4$, $Li[NiCoAl]O_2$, and $Li[NiMnCo]O_2$.

Despite its advantages, LIBs still suffer from degradation phenomena, the most significant of which are contributed by solid electrolyte interphase (SEI) layer formation, electrode mechanical fracture, and transition metal dissolution of active material. The SEI layer could serve as a protective layer formed on the electrode particle surface but becomes increasingly unstable during cycling, which causes faster aging of cells. The volume change of particles will cause stress during Li ion intercalation, which leads to

mechanical fracture of the material and accelerating capacity loss. The cathode active materials suffer from transition metal dissolution, especially at elevated temperatures, occurring on the cathode surface, which will increase the loss of active material and reaction resistance. Furthermore, the dissolved metal ions will transport through the electrolyte and deposit onto the anode surface, which will accelerate SEI layer formation, hinder Li ion intercalation and further increase reaction resistance. Finally, this results in energy fade and power fade, in particular at elevated temperature. Mn dissolution is an example of metal dissolution occurring in Mn-based cathode particles. One of Mn dissolution mechanisms is related disproportional of Mn^{3+}, where Mn^{3+} is unstable and can be easily converted to Mn^{4+} and the easily dissolved Mn^{2+}. The other Mn dissolution mechanism is due to hydrofluoric (HF) acid attack on the cathode surface. To prevent the critical challenge of metal dissolution and its branching issues, several strategies have been employed, such as elemental doping and adding electrolyte additive, but one of the most significant has been through surface coating technology.

Surface coating technology is the most efficient and facile way to improve battery performance. Among the many techniques that have been used to obtain surface coatings, Atomic Layer Deposition (ALD) is one of the most advanced methods and can achieve uniform, conformal, and pinhole-free coatings. ALD film coating can prevent side reaction between active material and electrolyte, modify particles surface structures, and protect active materials from serious degradation. Previous work showed that ultrathin film ALD coating could improve Li ion diffusivity and conductivity, leading to enhanced cycling stability and specific capacity of LIBs. Although a multitude of works has been done to develop and study this coating strategy

in LIBs, the fundamental physical mechanism of the surface coating on LIB active materials is yet to be fully captured. Therefore, our objective is to study the physics behind the surface coating to reveal the central reasoning to its enhancement of battery performance through the first-principles study. Density functional theory (DFT) is the first-principles (ab initio) approach of the electronic structure using Schrödinger's equation within a set of approximations, in which the material property is determined by the function of electron density. There are two key theorems in DFT. One theorem is that the ground state energy E is a unique functional of the electron density. The other theorem is that the electron density that minimizes the energy of the overall functional is the true ground state electron density. Thus, a problem for many-body electron systems can be studied as a set of single-electron wave functions that only depends on three spatial variables, which is known as Kohn–Sham equations. The first-principles study can be applied in electrochemistry field to investigate the fundamental battery degradation mechanism.

This dissertation deals with the fundamental mechanism of battery performance improvement via first-principles study. Paper I investigated the mechanism of Li ion intercalation into ALD coating and active material. The previous study showed that an ultrathin CeO_2 film coated $LiMn_2O_4$ significantly improved capacity and cycling performance compared to uncoated samples and Al_2O_3-coated samples at room and elevated temperatures. However, the mechanism of the improvement afforded by the ultrathin film coating layer remains unclear. In this paper, our objective is to clarify our experimental observation: why CeO_2-coated $LiMn_2O_4$ showed improved performance over Al_2O_3-coated $LiMn_2O_4$. To reveal the interfacial reaction between active material

and coating layer, Li ions intercalation preference and barrier energy of Li ions transport of coated active materials were investigated by first-principles calculation. The formation energy was calculated as a function of Li ion concentration to study how easily Li ions could intercalate through the coating. The energy change and barrier energy of Li ions were then inspected by considering the interaction between the active material and coating layer. Furthermore, to investigate the transport properties, Li ion diffusivity in $Li_xAl_2O_3$ and Li_xCeO_2 coating was calculated as a function of Li ion concentration in the coating layer.

Paper II studied ALD coating material impact on transition metal dissolution of cathode particles. An ideal cathode material should possess high operating potential, superior capacity, a long life cycle, and a sufficiently broad range of working temperatures. Although metal oxide cathodes satisfy these criteria, they suffer from an inevitable degradation process. The major reason for cathode degradation has been identified as structural changes in the material due to phase transformations, alternation of intrinsic properties, dissolution of transition metal ions, and increases in polarization voltage. Several strategies, such as reduction of particle size and surface modification of the active materials powder by coating have been proposed to overcome the dissolution process. In particular, surface modification, through the ALD method, where atomically thin layers of metal oxides can be controlled when deposited, has shown significant improvement both in capacity and in the life cycle. Stable metal oxides, such as ZnO, ZrO_2, SiO_2, TiO_2, $AlPO_4$, Al_2O_3, and CeO_2 notably improved battery performance and, as a result, it is believed that ALD coating strategies may preserve and stabilize a cathode particle by protecting particles from dissolution. In this work, the possible reduction of

metal dissolution after CeO_2 and Al_2O_3 ALD coatings were investigated. However, surprisingly, we observed that ultra-thin CeO_2 coating intensified the Mn dissolution of LMO during cycling of LIBs, whereas ultra-thin Al_2O_3 coating tended to inhibit Mn dissolution. A detailed DFT study was carried out to explain these experimental observations. First, the manganese vacancy formation energy was calculated, along with the bonding strengths of Mn-O of uncoated, Al_2O_3 coated, and CeO_2 coated particles via Crystal Orbital Overlap Population (COOP) calculations. Further, the projected Density-of-States (DOS) calculation of Mn was used to confirm the electronic occupancy of the Mn atom for each case. Finally, the discharging performance of uncoated LMO, Al_2O_3 coated LMO and CeO_2 coated LMO were inspected at room temperature and elevated temperature from the cell level.

Paper III focused on the ALD coating thickness impact on Li diffusivity in cathode particles. Previous work showed that the impact of the carbon coating thickness on the electrochemical performance of $LiFePO_4$/C composites. It demonstrated that carbon coating thickness of about 1-2 nm shows the best reversible capacity. $LiMn_2O_4$ particles coated with 1.02 nm ZnO ALD layers showed the best cycling performances among different ALD films coating thicknesses, which implied that the cycling performances of coated LMO particles can be easily optimized by accurately tuning coating thickness via varying ALD growth cycles. The Al_2O_3 coated Si electrode showed that the exchange current density and reaction rate constant reach maximum when coated with 0.55-1.1 nm ALD Al_2O_3 coating, while thick ALD Al_2O_3 coatings result in poor Li ion conductivity. Therefore, this work focuses on the phase transition impact and surface diffusion versus bulk diffusion domination impact on Li ion diffusivity in cathode

particles via performing the first-principles calculations. This work disclosed that Li diffusivity decreases with increasingly amorphous and crystal CeO_2 coating thickness and remained at a relatively constant value when coating thickness further increases. Besides, we found that Li ion diffuses very fast on CeO_2 coated LMO surface due to the surface diffusion domination. Also, Li ion diffuses faster on LMO surface in CeO_2 coated LMO due to the interaction between LMO active material and CeO_2 coating layer.

Paper IV investigated the interfacial property of SEI layer components. The SEI layer is formed on the negative electrode surface due to the side reaction between electrode and electrolyte. During the initial cycles, the SEI layer typically acts as an ionic conductor for Li ions but not an electronic conductor, thereby protecting the electrode from the further reductive decomposition of the electrolyte. However, upon prolonged cycling, the SEI layer does not keep its initial configuration and properties, which results in the capacity loss due to consuming Li ions, the increase of the interfacial resistance and accelerating LIBs capacity fade. During SEI layer decomposition, electrons and solvents could pass through the defective SEI layer, leading to further electrolyte decomposition and decrease in LIB performance. Various research has been conducted which focus on understanding the SEI structure and the mechanisms of its formation. The SEI layer on negative electrode consists of the inner layer and outer layer, where the inner layer comprised of the doubly reduced compounds, such as Li_2CO_3, Li_2O, and LiF, and the outer layer is the organic layer, which consists of alkyl dicarbonate species such as Li_2EC, Li_2EDC and Li_2BDC. The Young's moduli of SEI layer components range from 2.4GPa to 58.1GPa in the order of polymeric, organic and amorphous inorganic components. Although various works are focusing on the SEI layer, the interfacial

stability of the SEI layer is not sufficient investigated. Therefore, in this work, we mainly investigated the interfacial property of SEI layer components. The separation response of SEI layer components (such as LiF/Li_2CO_3, LiF/Li_2O, LiF/Li_2EC and Li_2EC/Li_2EDC) was studied. It revealed that the fracture strength of inorganic-inorganic interface higher than the organic-organic interface.The inorganic and organic interface is unstable due to the repulsive interaction between the two components.

PAPER

I. FIRST-PRINCIPLES STUDY OF ULTRATHIN FILM COATING ON CATHODE PARTICLES IN LITHIUM ION BATTERIES

ABSTRACT

An ultrathin film coating via Atomic Layer Deposition (ALD) is a viable approach for significantly enhancing Lithium-Ion Battery (LIB) performance. Despite several demonstrations of this improvement, the fundamental understanding on the role of ultrathin film coating is still unclear, especially regarding the interaction between coating layers and active materials. In this work, first-principles calculations focused on energetic preferences, lithium ion transport, and structural changes of coating layer are conducted to understand an experimental observation that CeO_2 coatings exhibit better performance in capacity and cycling than Al_2O_3 coatings. The study reveals that the barrier energy of Li ion transportation from CeO_2 coating to active material is lower than that from Al_2O_3 coating, suggesting easier intercalation of Li ions into the active materials. This systematic study provides us an important clue about the beneficiary role of ALD coating in LIB performance and capacity retention.

1. INTRODUCTION

The performance of current battery technology cannot keep pace with the booming demand of long-lasting and efficient energy storage in transportation and stationary applications. Higher energy and power density, outstanding cycling performance, and enhanced safety for Lithium-Ion Battery (LIBs) are the needs of the

hour to run with the increased capability, speed, and versatility of consumer electronics. Active cathode materials have a major contribution in improving battery performance and lifetime. Several families of materials have attracted attention in the field of next-generation long-life rechargeable LIBs. However, all electrode materials for LIBs suffer from degradation phenomena, including solid electrolyte interphase (SEI) layer formation, surface stress, mechanical fracture, and transition metal dissolution of active material[1-4]. The SEI layer could serve as a protective layer formed on anode particle surface, but it becomes unstable during cycling, which causes faster aging of cells. The developed stress due to the volume change during Li ion intercalation causes mechanical fracture of the material accelerating capacity loss. Another key challenge is the dissolution of transition metal ions at elevated temperatures. During the dissolution of transition metal ions, the structure of transition metal based cathodes undergo changes, which in turn reduces the number of the available positions for Li ion intercalation. Additionally, some metals (e.g., Mn^{4+}), which have higher oxidation ability, can cause the decomposition of electrolyte solvent. Fortunately, several approaches, such as the substitution of Mn by doping materials and wrapping $LiMn_2O_4$ (LMO) in a conductive thin layer, can arrest these processes and provide longer cycle-life. As cell aging in both cycling and storage mode is rooted primarily from the side reactions at electrode-electrolyte interfaces, surface modification through the coating on active material particles is an efficient way to improve battery performance and cycle life. The coating materials investigated, to date, in LIB applications include diverse carbon, metal oxides (Al_2O_3, ZrO_2, ZnO, and SiO_2) [5-7], and metal phosphate ($AlPO_4$) [8-9]. The majority of the coating strategies were based on the sol-gel methods which require a heat treatment

after the coating process [7-11]. These coating technologies can cause an unstable interface and poor longevity of performance due to possible incomplete coating or an overly thick coating [12]. In contrast, an ultrathin film coating, with a thickness at sub-nanometer levels, has the potential for augmenting the electron and Li ion conductivity for coating materials. Atomic Layer Deposition (ALD) is an efficient approach to create such ultra-thin films, in which strong chemical bonds are created to maintain the physical integrity between the substrate and the coating layer. Recently, ultrathin film coatings on the active material surface, including $LiNiO_2$ [13], $LiCoO_2$ [14-16], $LiMn_2O_4$ [17], Fe_3O_4-rGO[18], have been claimed to significantly improve cell performance. Also, Li-excessed $LiNiO_2$, $LiCoO_2$ and $LiMn_2O_4$ [19-20] active materials have exhibited better performance when coated with Al_2O_3 ALD ultrathin film. In particular, an ultrathin CeO_2 film coated $LiMn_2O_4$ have significantly improved capacity and cycling performance compared to uncoated samples and Al_2O_3-coated samples at room and high temperatures [21]. Whilst a large number of experiments have been conducted to observe the improved performance, a few works have been done to understand the role of ALD coating in enhancing battery performance. Researchers have provided the guidance of high-performance LIB by identifying the reduced oxygen evolution and thermal stability of Al_2O_3-coated $LiNiO_2$ surface using first-principles calculation [13]. The thermodynamic and kinetic properties of surface coatings play a vital role in the electrochemical performance of LIBs. To identify Li ion transportation in crystalline and amorphous coatings, density functional theory (DFT) calculations and statistical mechanics have been combined. It was concluded that Li ion had slower diffusion in crystalline α-AlF_3, α-Al_2O_3, m-ZrO_2, and c-MgO coating due to a larger migration barrier (>0.9 V).

However, am-Al_2O_3 and am-AlF_3 showed smaller Li ion migration barriers thus, had significantly faster diffusion than their crystalline counterparts [22]. Li ion diffusivity in lithium lanthanum titanium oxides (LLTO) [23], Li_2NiO_2 and Li_xCoO_2 structure displayed that the activation barrier was very sensitive to the lithium concentration [24-25]. Besides, Li ion diffusion characteristics in Al_2O_3 coating on $LiMn_2O_4$ [26-29] and SiO_2 coating on Si [30-31] have been observed at different Li ion concentrations.

Despite several previous studies, the role of the ultrathin film coating layer remains unclear. Particularly, studies about the coating layer encapsulated active material have not been done methodically in literature focusing on kinetic and thermodynamic aspects. In this paper, our objective is to clarify our experimental observation [21]: why CeO_2-coated $LiMn_2O_4$ showed improved performance than Al_2O_3-coated $LiMn_2O_4$. To reveal the interfacial reaction between active material and coating layer, Li ion intercalation preference and barrier energy of Li ion transportation of coated active materials were investigated by first-principles calculation. $LiMn_2O_4$ slab structure with 001, 110 and 111 surface orientation has been studied extensively [32] and showed $LiMn_2O_4$ with 001_Li_2 surface orientation structure had lowest surface stability. Therefore, only $LiMn_2O_4$ with 001_Li_2 slab structure has been prioritized. The formation energy was calculated as a function of Li ion concentration to study how easily Li ion could intercalate coating. Also, the energy change and barrier energy of Li ion has been calculated by considering the interaction between active material and coating. Furthermore, to investigate the transport properties, Li ion diffusivities in $Li_xAl_2O_3$ and Li_xCeO_2 coating were calculated as a function of Li ion concentration in the coating

layer. Finally, the structural change was studied during the lithiation process through the radial distribution functions (RDF) and charge state calculation.

2. COMPUTATIONAL DETAILS

2.1. THEORETICAL CALCULATIONS

Density functional theory calculations and Ab initio molecular dynamics simulations have been performed by using VASP code[38]. The Perdew−Burke−Ernzerhof (PBE) exchange and correlation functional and the projector augmented wave (PAW) method were applied [39]. The electronic wave functions were expanded on a plane wave basis set of 400eV for $Li_xAl_2O_3$ and Li_xCeO_2 system, and 600 eV for Al_2O_3-coated $LiMn_2O_4$ and CeO_2-coated $LiMn_2O_4$ system. The amorphous $Li_xAl_2O_3$ structure contained 10×x Li, 20 Al, and 30 O, and the amorphous Li_xCeO_2 structure contained 10×x Li, 10 Ce, and 20 O in the cubic supercell. The amorphous structures were created by using quench processing [27], which included heating, equilibration, and cooling processes. Li ion concentration value x ($0 \leq x \leq 4$), and 7 cases (x=0.0, 0.2, 1.0, 2.0, 3.0, 3.5, 4.0) were considered to study the formation energy, volume expansion, structure evolution.

2.2. THE FORMATION ENERGY CALCULATION

The Formation energy [26, 40] of $Li_xAl_2O_3$ and Li_xCeO_2 was defined as follows:

$$E_{f(x)} = E_{tot}(Li_xAl_2O_3/Li_xCeO_2) - xE_{tot}(Li) - E_{tot}(Al_2O_3/CeO_2) \quad (1)$$

where $E_{tot}\,(Li_xAl_2O_3)$ and $E_{tot}\,(Li_xCeO_2)$ are the total energy per $Li_xAl_2O_3$ unit and per Li_xCeO_2 unit respectively, $E_{tot}\,(Li)$ is the total energy per atom of bcc Li bulk, and E_{tot}

(Al_2O_3) and *E_{tot} (CeO_2)* are the total energy per Al_2O_3 unit and per CeO_2 unit, respectively.

2.3. VOLUME EXPANSION AND LI DIFFUSIVITY CALCULATION

For volume expansion calculation, both shape and volume were allowed to change with 3 k points and 520 eV cutoff energy [26, 28, 40]. To calculate Li ion diffusivity in $Li_xAl_2O_3$ and Li_xCeO_2 as a function of Li ion concentration, the Nosé-Hoover thermostat [26, 40-45] was used to control the temperature, and ab initio MD simulations were performed for 10 ps to obtain the mean square displacement at T = 1200 K, 1600 K, 2000 K, and 2400 K, respectively. Based on the Einstein relation

$$r^2(t) = 6Dt \tag{2}$$

The diffusion coefficient was calculated at high temperature 1200K, 1600K, 2000K, and 2400K, respectively. This is because it is more accurate to calculate self-diffusion in high temperatures by using the DFT calculation [12]. The *D* values obtained from the Einstein relation at high temperatures were used to extrapolate the *D* value at *T* = 300K according to the Arrhenius law:

$$D = D_0 \exp(-E_D / k_B T) \tag{3}$$

where D_0 is the pre-exponential factor, E_D is the activation energy for diffusion, and k_B is the Boltzmann constant.

2.4. LI ION TRANSPORTATION MECHANISM

To study Li ion transportation in ultrathin CeO_2 and Al_2O_3 film coatings, the mechanism from different aspects has been studied. From the thermodynamic aspect, the

most stable configuration of $Li_xAl_2O_3$ and Li_xCeO_2 has been found, and the lower formation energy, which means that Li ion can easily intercalate, has been studied. From the mechanical aspect, volume expansion has been calculated to study the difference of thickness change of the Al_2O_3 and CeO_2 coatings during Li ion intercalation – this is associated with the mechanical damage of coating itself. From the atomistic and electronic structural aspect, the radial distribution function and the charge state of atoms were calculated to investigate the structure evolution of amorphous $Li_xAl_2O_3$ and Li_xCeO_2. From the kinetic aspect, Li ion concentration impact on Li ion diffusivity in the amorphous coating was studied. The active material impact on Li ion transportation has also been considered, which was ignored by previous work[26]. To identify how Li ion further intercalate $LiMn_2O_4$ after passing through coating, the Al_2O_3(12Al, 18O) and CeO_2-(7Ce, 14O) coated $LiMn_2O_4$ (16 Li, 32 Mn and 64 O) structure [32] with Li-terminated 001 surface orientation (001_Li_2) was prepared. Li ion transportation from Al_2O_3 and CeO_2 coatings to active material $LiMn_2O_4$ particles was investigated.

2.5. ENERGY CHANGE DURING LI ION INTERCALATION

By comparing the total energy change of Al_2O_3 and CeO_2-coated $LiMn_2O_4$ before Li ion intercalation, after Li ion intercalation into the coating and after Li ion intercalation into LMO particles, it can be determined when Li ion tends to intercalate coating from the thermodynamic aspect. The total energy of Al_2O_3/Mn_2O_4, $Li_xAl_2O_3/Mn_2O_4$, $Al_2O_3/Li_xMn_2O_4$, CeO_2/Mn_2O_4, Li_xCeO_2/Mn_2O_4 and $CeO_2/Li_xMn_2O_4$ were calculated. To further study Li ion transportation from coating to active material, barrier energy was calculated during Li ion transportation by performing the CINEB

(climbing nudged elastic band) method [22, 24-25, 33]. Three images between the initial configuration and final configuration were selected to calculate the Li ion transportation barrier energy.

3. RESULTS AND DISCUSSION

3.1. FORMATION ENERGY CALCULATION

First, to examine how easily Li ion can intercalate Al_2O_3 coating and CeO_2 coating, the formation energy of $Li_xAl_2O_3$ and Li_xCeO_2 as a function of Li ion concentration was compared. The system size of $Li_xAl_2O_3$ and Li_xCeO_2 was determined by a convergence test (Figure S1). The lowest formation energy for Li_xCeO_2 and of $Li_xAl_2O_3$ was about -1.495eV and -1.018eV when x was 3.5 (Figure 1). The formation energy value of $Li_xAl_2O_3$ agreed well with the reported value [26]. Also, the calculated Li to Al atomic ratio of 1.75 (Figure 1) at the lowest formation energy was similar to the reported value of 1.6 from the experimental study and 1.7 from the modeling study [14, 26]. Compared to the formation energy of $Li_xAl_2O_3$, the formation energy for Li_xCeO_2 was much lower at different Li ion concentrations, which suggested Li ion could intercalate into the coating layer more easily for the CeO_2 coating than for the Al_2O_3 coating layer. In other words, Li ion could pass the CeO_2 coating more easily. This was a thermodynamic evidence that CeO_2 coating had better battery performance than the Al_2O_3 coating did. After Li ions passed through the coating, eventually, the Li ions must intercalate into the active materials to complete the redox reactions. In a previous study[26], based on the formation energy calculation, Li ions preferred to stay in the coating layer as long as the formation energy was lower. However, those Li ions may intercalate into the

active material sooner or later. As the coating layer may change the Li ion intercalation behavior of the active material, it was necessary to consider the active material along with the coating layer to capture the actual physics. To study the effective properties, 0.5 nm thickness of CeO_2 coating layer was added on top of the active material ($LiMn_2O_4$). Then, the energies from three stages of intercalation processes were compared: before-intercalation, Li ions residing in the layer, and the final stage with the Li ion intercalated into the active material. First, the total energy of the coated active material, in the absence of the Li ion, has been evaluated. To examine whether Li ions wanted to intercalate in the coating material, the total energy of the coating material with one Li ion inside has been calculated. It was found that the total energy of one Li ion intercalated Al_2O_3 coating was 5.71eV lower than before Li ion intercalation (Table 1), suggesting that Li ion desired to intercalate the coating layer. Next, to see whether Li ion further desired to intercalate through the active material from the coating layer, the total energy of Al_2O_3-coated $LiMn_2O_4$ with one Li ion inside the $LiMn_2O_4$ was calculated. It was found that the total energy of Li ion inserted into $LiMn_2O_4$ was 2.53 eV higher than that of Li ion intercalated in the coating layer (Table 1). Similar steps have been repeated for CeO_2-coated $LiMn_2O_4$. The total energy of one Li ion in CeO_2 coating is 3.42 eV lower than that of the case before Li ion intercalation into the coating layer and 1.59 eV lower than that of Li ion intercalation into $LiMn_2O_4$ (Table 1). Therefore, for both Al_2O_3 and CeO_2 coating layers, one Li ion tends to stay in the coating layer rather than in the intercalated active material.

As the next step, two Li ions' intercalation processes have been tested. As listed in Table 2, the final stage with two Li ions intercalated into the active material showed

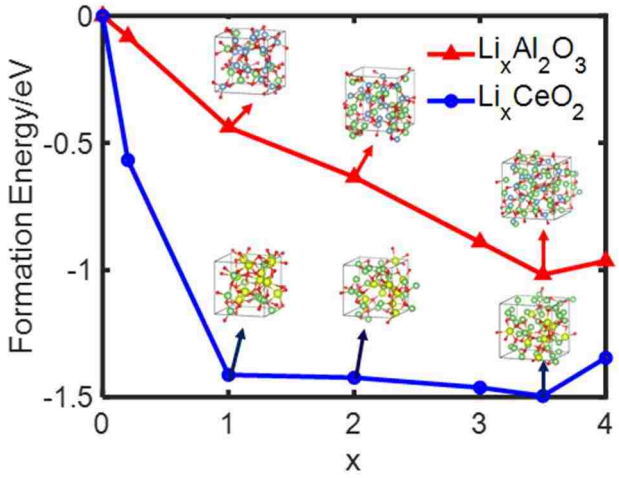

Figure 1. Formation energy of $Li_xAl_2O_3$ and Li_xCeO_2 as a function of lithium content without active material.

Table 1. Energy change during one Li ion intercalation[a].

structure	$E_{coating}$	E_{LMO}
Al_2O_3/LMO	-5.71eV	2.53eV
CeO_2/LMO	-3.42eV	1.59eV

([a]Energy change before Li ion intercalation, one Li ion intercalation into the coating, and one Li ion intercalation into LMO. $E_{coating}$ is the energy change after one Li ion intercalation into the coating, and E_{LMO} is the energy change after one Li ion intercalation into the LMO particle.)

the lowest energy level for both coating materials. The energy change for each step was 9.89 eV and 2.02 eV for the Al_2O_3 coating layer, and 2.58 eV and 2.98 eV for the CeO_2 coating layer. These results implied that two Li ions would further intercalate into the active material after intercalating into the coating layer from thermodynamic aspect. When the coating layer is only considered as the literature work did, the intercalated Li ions will accumulate in the layer until it reaches its lowest energy level. However, it turns

out that this is not true. There is an experimental evidence that the coating thickness undergoes a limited amount of volume change instead of full volume change during the intercalation process[20]. The energy barrier to the intercalation may allow accumulation of Li ions inside the layer, and the accumulated Li ions induce the observed volume change.

Table 2. Energy change during two Li ion intercalation [a].

structure	$E_{coating}$	E_{LMO}
Al_2O_3/LMO	-9.89eV	-2.02eV
CeO_2/LMO	-2.58eV	-2.98eV

([a]Energy change before two Li ions intercalation, two Li ions intercalation into the coating and two Li ions intercalation into the LMO particle. $E_{coating}$ is the energy change after one Li ion intercalation into the coating, and E_{LMO} is the energy change after one Li ion intercalation into the LMO particle.)

3.2. THE BARRIER ENERGY OF LI ION INTERCALATION

To further examine how Li ions transport from coating to the active material, the barrier energy of Li ions intercalation to the active material from the coating layer was calculated by using the CINEB (climbing nudged elastic band) method [22, 24-25, 33]. As shown in Figure 2, the Li ion barrier energy of Al_2O_3-coated $LiMn_2O_4$ was 1.26 eV and barrier energy for CeO_2-coated $LiMn_2O_4$ was 0.86 eV. The energy barrier will prevent the intercalated Li ions passing through the coating layer and moving to the active material immediately. Furthermore, the barrier energy for the CeO_2 coating was lower than that for the Al_2O_3 coating, so it was easier for Li ions to intercalate into the active material with the CeO_2 layer. This could be one piece of evidence for better battery performance with the CeO_2 coating layer.

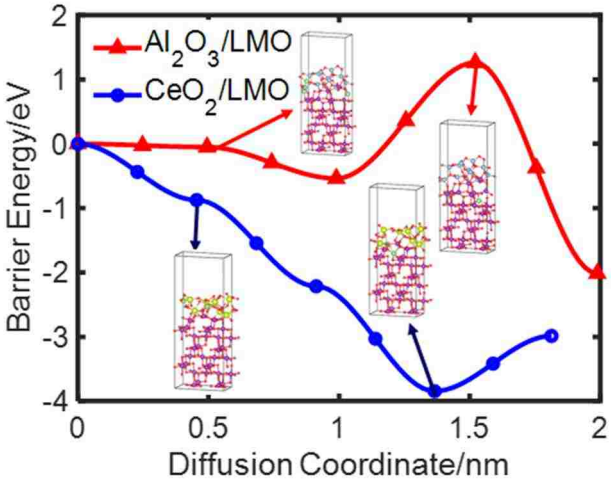

Figure 2. Barrier energy of Al_2O_3 and CeO_2-coated $LiMn_2O_4$ with two Li ions intercalation.

3.3. THE TRANSPORT PROPERTY OF AL_2O_3 AND CEO_2 COATING

Another important property of coating material that affects the battery performance is Li ion diffusivity. To investigate this transport property of Al_2O_3 and CeO_2 coating, the mean square displacement of Li ions at 1200, 1600, 2000 and 2400K was calculated based on the Einstein relation $< r^2(t) >= 6Dt$ (Figure S2-11). Then, according to the Arrhenius law $D = D_0 \exp(-E_D / k_B T)$, Li ion diffusivity could be obtained at 300K [26]. It was found that the diffusion coefficient of $Li_xAl_2O_3$ and Li_xCeO_2 was increased when Li ion concentration increased. The diffusion coefficient of Li_xCeO_2 was higher than that of $Li_xAl_2O_3$ (Figure 3&Table S1) at different Li ion concentrations, which could be another reason for the better battery performance for the CeO_2 coated particles than that of the Al_2O_3 coated particles.

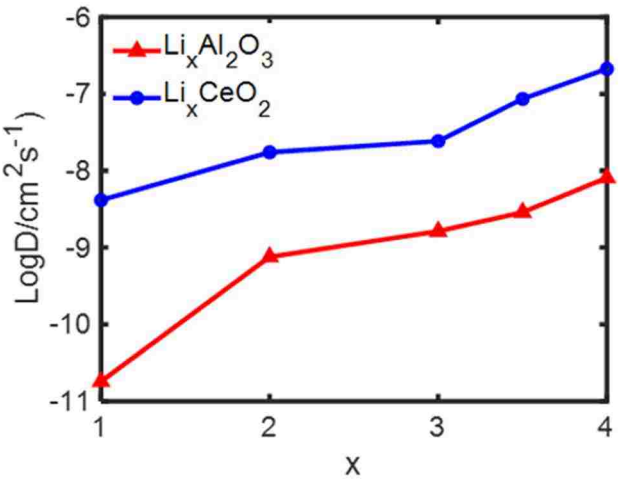

Figure 3. Li ion diffusion coefficients of $Li_xAl_2O_3$ and Li_xCeO_2.

3.4. VOLUME CHANGES DURING LI ION INTERCALATION

One important concern is the mechanical damage of the coating layer itself due to the volume changes during intercalation and deintercalation of Li ions. To study the coating expansion during lithiation, the volume expansion of $Li_xAl_2O_3$ and Li_xCeO_2 was calculated. As seen in Figure 4, the volume expansion of $Li_xAl_2O_3$ and Li_xCeO_2 increased almost linearly as a function of Li ion concentration. For instance, the volume expansion ratio of $Li_xAl_2O_3$ at x = 3.5 was $V/V_0 = 2.08$, which well matched with the experimentally observed value ($V/V_0 = 2.25$) [34]. At a low Li ion concentration, the volume expansion value of the CeO_2 coating layer was little owing to the faster Li ion diffusion and lower barrier energy. The Li ion concentration in the CeO_2 coating layer will not be high because Li ions always tend to intercalate LMO particles immediately after passing through the coating. However, Li ions stay longer in the Al_2O_3 coating layer, which will cause a higher volume expansion. Higher volume expansion means a

longer distance for Li ions to pass before reaching LMO particles and mechanical damage of the coating itself. Therefore, there was a higher possibility of damage of the Al_2O_3 coating layer was than that of the CeO_2 coating layer, which also could explain why CeO_2 coating can improve LIB performance more.

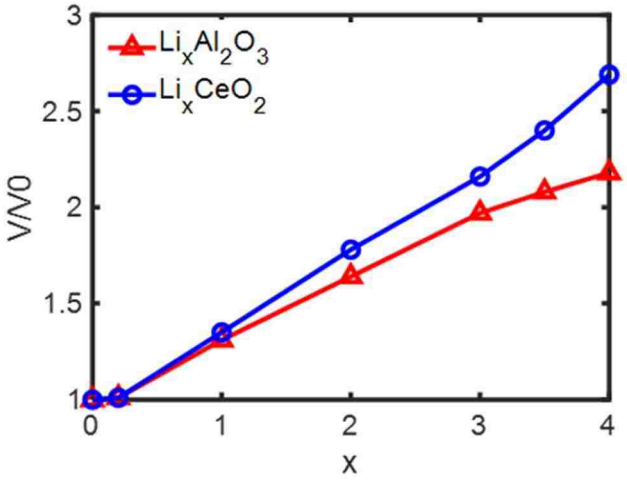

Figure 4. Comparison of the volume expansion of $Li_xAl_2O_3$ and Li_xCeO_2 without active material.

3.5. PHYSICAL CHANGE DURING LI ION INTERCALATION

To further obtain insight into physical change during intercalation, more detailed structural changes of the coating materials have been studied by ab initio MD simulations. First, through analyzing the radial distribution function (RDF), it was found that the Li-O bond length of $Li_xAl_2O_3$ (Figure 5A) and Li_xCeO_2 (Figure 5D) was about 2.0 Å, which agreed well with the experimental data of 1.9 Å of Li_2O_2 [26, 35]. The Li–O

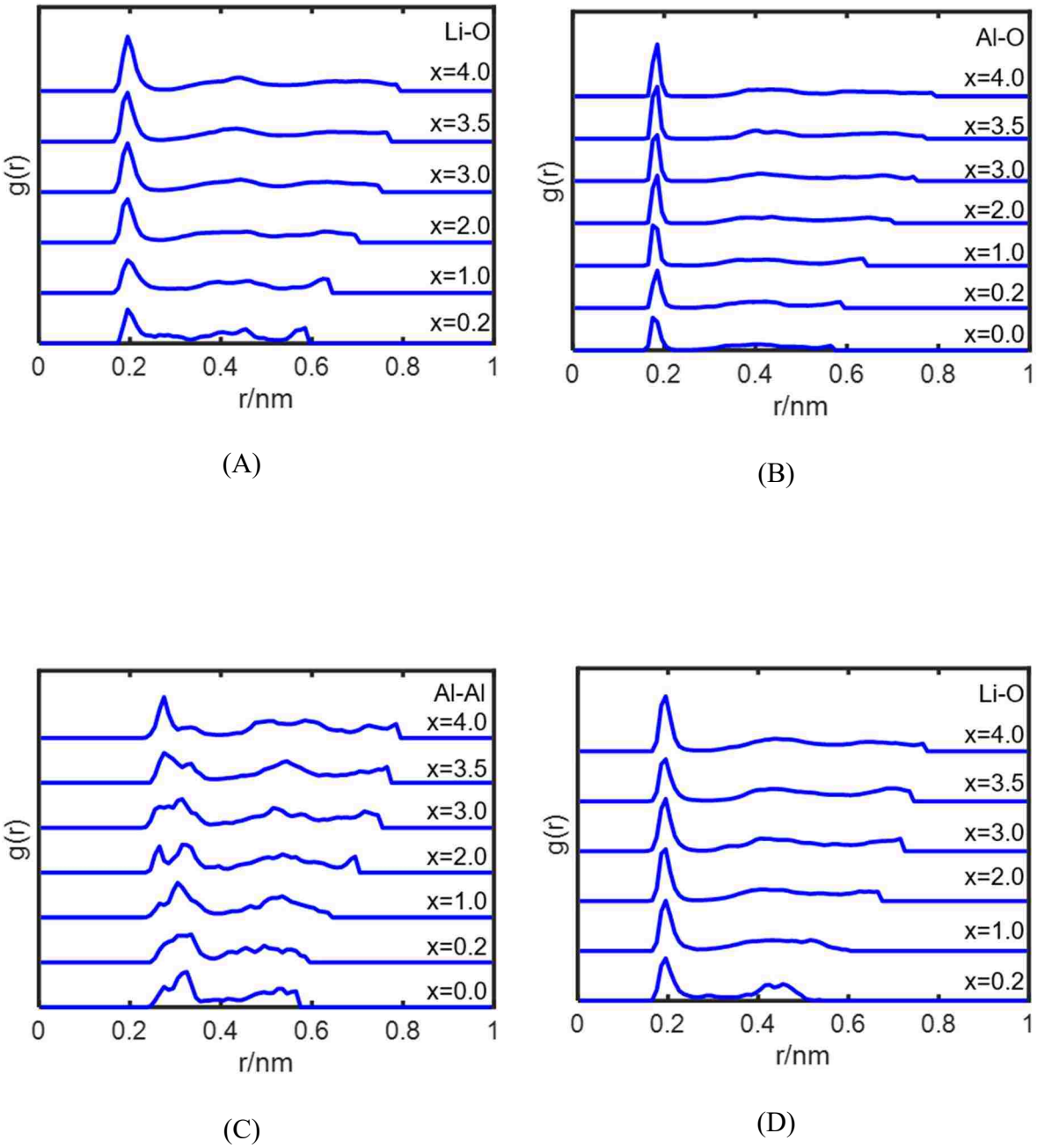

Figure 5. Radial distribution function of Li-O (A), Al-O (B), Al-Al(C) in $Li_xAl_2O_3$ and Li-O(D), Ce-O(E), Ce-Ce(F) in Li_xCeO_2.

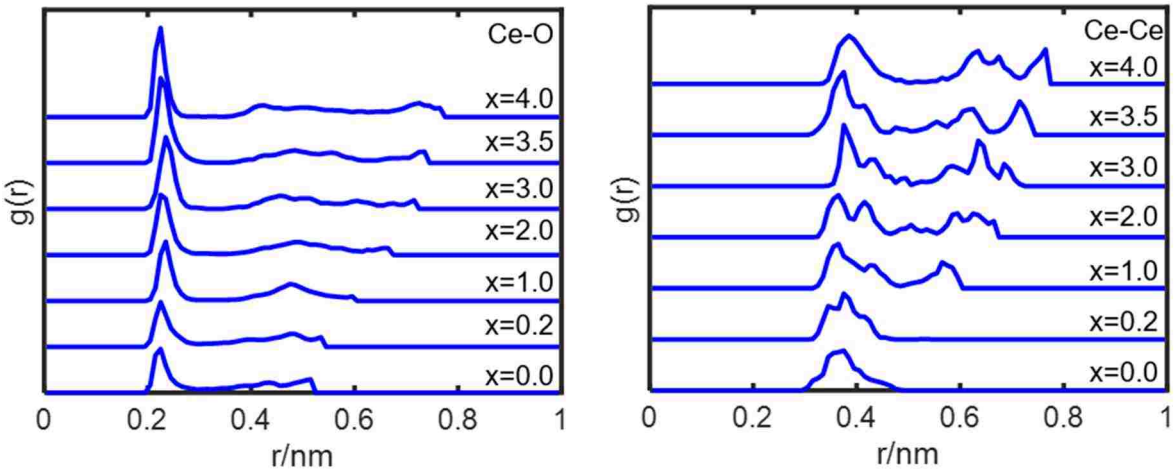

(E) (F)

Figure 5. Radial distribution function of Li-O (A), Al-O (B), Al-Al(C) in $Li_xAl_2O_3$ and Li-O(D), Ce-O(E), Ce-Ce(F) in Li_xCeO_2 (cont.).

bond length of 2.0 Å and Al−O bond length of 1.8 Å and Ce–O bond length of 2.2 Å remained unchanged with increasing Li ions (Figure 5A, B, D&E). The Al–O bond length of 1.8 Å was the same as the reported value[26], and the Ce−O bond length of 2.2 Å agreed well with the reported Ce–O bond length of 2.15 Å[36]. However, the Al−Al and Ce–Ce bond length kept changing during lithiation. At low Li ion concentration, the Al−Al bond length was 3.2 Å and the Ce−Ce bond length was 3.8 Å (Figure 5F). The Ce−Ce bond length was 3.8 Å (Figure 5F) at concentration x = 0, which agreed well with the reported Ce–Ce bond length of 3.826 Å of cubic CeO_2[37]. As Li ion concentration increased, the Al-Al bond length altered from 3.2 Å (x=0) to 2.8 Å (x=0) (Figure 5C), which was the same as the reported data[26] and Ce-Ce bond length peak changed from 3.8 Å (x=0) to 3.6 Å (x=4) (Figure 5F), indicating that individual Al and Ce atoms had a variety of charge states during lithiation. Also, Bader charge analysis was used to

quantify the charge distribution of atoms in $Li_xAl_2O_3$ and Li_xCeO_2 coating during lithiation. Charge analysis can reflect the amorphous structure alternation. During lithiation, Al changed from +2.5 (x = 0) to +1.0 (x = 4) and Ce had a significant change

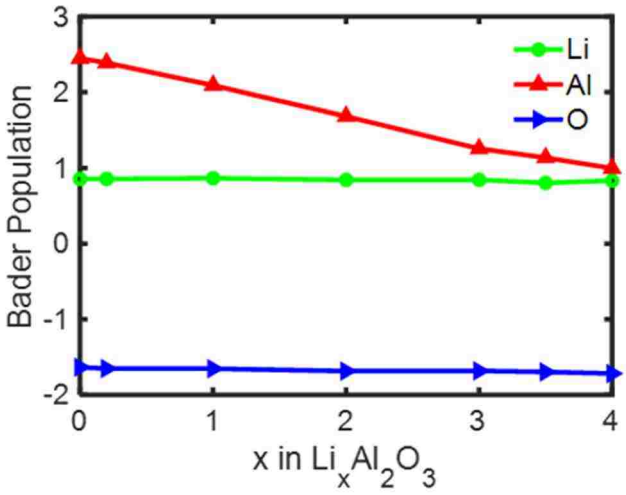

(A)

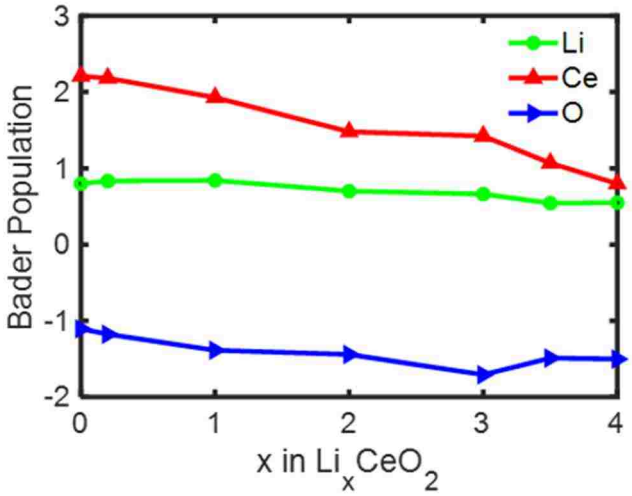

(B)

Figure 6. Bader population of $Li_xAl_2O_3$ (A) and Li_xCeO_2 (B).

from +2.2 (x = 0) to +1.1 (x = 4). Meanwhile, charge states of Li and O of amorphous $Li_xAl_2O_3$ and Li_xCeO_2 structure exhibited a slight variation (Figure 6A&B), which agreed well with the reported value[26]. It suggested that individual Al and Ce atoms had various charge states during lithiation, which was consistent with RDF results. The various charge states of Al and Ce mainly originated from the incoming Li ions.

4. CONCLUSIONS

In this work, the study of amorphous Al_2O_3 and CeO_2-coated $LiMn_2O_4$ demonstrates sufficient reason behind the improved performance of CeO_2-coated active material than that of Al_2O_3-coated active material. In view of the lower formation energy of Li_xCeO_2 than that of $Li_xAl_2O_3$, Li ions can effortlessly intercalate into CeO_2 coating than Al_2O_3 coating. Considering the $LiMn_2O_4$ active material along with Al_2O_3 and CeO_2 coating layers, energy change during Li ion intercalation was calculated to find that two ions start to intercalate $LiMn_2O_4$ after passing through Al_2O_3 and CeO_2 coating. However, there is a barrier energy needed to overcome. Our finding shows that barrier energy of Li ion transportation from CeO_2 coating to active material is lower than that of Al_2O_3 coating, suggesting easy intercalation of Li ions in $LiMn_2O_4$ from CeO_2 coating than Al_2O_3 coating. As a result, more Li ions want to stay behind in $LiMn_2O_4$ while it is coated with the Al_2O_3 layer, leading to the volume expansion observed experimentally. Kinetically, Li ions in Li_xCeO_2 coating diffuse faster than in $Li_xAl_2O_3$ coating, resulting in the better performance of the cell. In summary, this work yields a clear clue for the reason of why ALD coating is beneficial to LIB and also gives us evidence why CeO_2

ALD coating has improved performance than other binary coating material during the lithiation process from the fundamental study at electronic level.

REFERENCES

[1] Verma, P.; Maire, P.; Novák, P., A review of the features and analyses of the solid electrolyte interphase in Li-ion batteries. Electrochimica Acta 2010, 55 (22), 6332-6341.

[2] Sarkar, S., Patel, R. L., Liang, X., & Park, J, Unveiling the Role of CeO_2 Atomic Layer Deposition Coatings on $LiMn_2O_4$ Cathode Materials: An Experimental and Theoretical Study. ACS applied materials & interfaces 2017, 9 (36), 30599-30607.

[3] Ebner, M., Marone, F., Stampanoni, M., & Wood, V, Visualization and quantification of electrochemical and mechanical degradation in Li ion batteries. Science 2013, 342 (6159), 716-720.

[4] Etacheri, V.; Marom, R.; Elazari, R.; Salitra, G.; Aurbach, D., Challenges in the development of advanced Li-ion batteries: a review. Energy & Environmental Science 2011, 4 (9), 3243.

[5] Cho, J.; Kim, Y.; Park, B., Novel $LiCoO_2$ cathode material with Al_2O_3 coating for a Li ion cell. Chemistry of Materials 2000, 12 (12), 3788-3791.

[6] Sun, Y.; Lee, Y.; Yoshio, M.; Amine, K., Synthesis and electrochemical properties of ZnO-coated $LiNi_{0.5}Mn_{1.5}O_4$ spinel as 5 V cathode material for lithium secondary batteries. Electrochemical and Solid State Letters 2002, 5 (5), A99-A102.

[7] Chen, Z.; Dahn, J. R., Studies of $LiCoO_2$ coated with metal oxides. Electrochemical and Solid State Letters 2003, 6 (11), A221-A224.

[8] Appapillai, A. T.; Mansour, A. N.; Cho, J.; Shao-Horn, Y., Microstructure of $LiCoO_2$ with and without "AlPO4" nanoparticle coating: Combined STEM and XPS studies. Chemistry of Materials 2007, 19 (23), 5748-5757.

[9] Bai, Y.; Liu, N.; Liu, J.; Wang, Z.; Chen, L., Coating material-induced acidic electrolyte improves $LiCoO_2$ performances Electrochemical and Solid State Letters 2006, 9 (12), A552-A556.

[10] Zhang, Y.; Sun, C. S.; Zhou, Z., Sol-gel preparation and electrochemical performances of $LiFe_{1/3}Mn_{1/3}Co_{1/3}PO_4/C$ composites with core-shell nanostructure. Electrochemistry Communications 2009, 11 (6), 1183-1186.

[11] Sun, Y.; Myung, S.; Park, B. C.; Prakash, J.; Belharouak, I.; Amine, K., High-energy cathode material for long-life and safe lithium batteries. Nature Materials 2009, 8 (4), 320-324.

[12] Chen, Z.; Qin, Y.; Amine, K.; Sun, Y. K., Role of surface coating on cathode materials for lithium-ion batteries. Journal of Materials Chemistry 2010, 20 (36), 7606.

[13] Kang, J.; Han, B., First-Principles Study on the Thermal Stability of $LiNiO_2$ Materials Coated by Amorphous Al_2O_3 with Atomic Layer Thickness. ACS Appl Mater Interfaces 2015, 7 (21), 11599-603.

[14] Jung, Y. S.; Cavanagh, A. S.; Riley, L. A.; Kang, S. H.; Dillon, A. C.; Groner, M. D.; George, S. M.; Lee, S. H., Ultrathin direct atomic layer deposition on composite electrodes for highly durable and safe Li-ion batteries. Adv Mater 2010, 22 (19), 2172-6.

[15] Lee, J.-T.; Wang, F.-M.; Cheng, C.-S.; Li, C.-C.; Lin, C.-H., Low-temperature atomic layer deposited Al_2O_3 thin film on layer structure cathode for enhanced cycleability in lithium-ion batteries. Electrochimica Acta 2010, 55 (12), 4002-4006.

[16] Jae Ha Woo, J. E. T., Andrew S. Cavanagh, Yong Seok Choi,Seul Cham Kim, Steven M. George,Kyu Hwan Oh, and Se-Hee Lee, Nanoscale Interface Modification of $LiCoO_2$ by Al_2O_3 Atomic Layer Deposition for Solid-State Li Batteries. Journal of the Electrochemical Society 2012, 159 (7).

[17] Yoon Seok Jung, A. S. C., Yanfa Yan,; Steven M. George, a. A. M., Effects of Atomic Layer Deposition of Al2O3 on the Li[Li0.20Mn0.54Ni0.13Co0.13]O2 Cathode for Lithium-Ion Batteries. Journal of the Electrochemical Society 2011, 158 (12).

[18] Wu, Q.-H.; Qu, B.; Tang, J.; Wang, C.; Wang, D.; Li, Y.; Ren, J.-G., An Alumina-Coated Fe_3O_4-Reduced Graphene Oxide Composite Electrode as a Stable Anode for Lithium-ion Battery. Electrochimica Acta 2015, 156, 147-153.

[19] [Zhang, X.; Belharouak, I.; Li, L.; Lei, Y.; Elam, J. W.; Nie, A.; Chen, X.; Yassar, R. S.; Axelbaum, R. L., Structural and Electrochemical Study of $Al_2O_3$and TiO_2 Coated $Li_{1.2}Ni_{0.13}Mn_{0.54}Co_{0.13}O_2$ Cathode Material Using ALD. Advanced Energy Materials 2013, 3 (10), 1299-1307.

[20] Liu, Y.; Hudak, N. S.; Huber, D. L.; Limmer, S. J.; Sullivan, J. P.; Huang, J. Y., In situ transmission electron microscopy observation of pulverization of aluminum nanowires and evolution of the thin surface Al_2O_3 layers during lithiation-delithiation cycles. Nano Lett 2011, 11 (10), 4188-94.

[21] Patel, R. L.; Xie, H.; Park, J.; Asl, H. Y.; Choudhury, A.; Liang, X., Significant Capacity and Cycle-Life Improvement of Lithium-Ion Batteries through Ultrathin Conductive Film Stabilized Cathode Particles. Advanced Materials Interfaces 2015, 2 (8), 1500046.

[22] Xu, S.; Jacobs, R. M.; Nguyen, H. M.; Hao, S.; Mahanthappa, M.; Wolverton, C.; Morgan, D., Lithium transport through lithium-ion battery cathode coatings. J. Mater. Chem. A 2015, 3 (33), 17248-17272.

[23] Qian, D.; Xu, B.; Cho, H.-M.; Hatsukade, T.; Carroll, K. J.; Meng, Y. S., Lithium Lanthanum Titanium Oxides: A Fast Ionic Conductive Coating for Lithium-Ion Battery Cathodes. Chemistry of Materials 2012, 24 (14), 2744-2751.

[24] Kang, K.; Morgan, D.; Ceder, G., First principles study of Li diffusion inI-Li_2NiO_2structure. Physical Review B 2009, 79 (1).

[25] Van der Ven, A., and G. Ceder, Lithium diffusion mechanisms in layered intercalation compounds. Journal of power sources 2001, 97, 3.

[26] Jung, S. C.; Han, Y.-K., How Do Li Atoms Pass through the Al_2O_3 Coating Layer during Lithiation in Li-ion Batteries? The Journal of Physical Chemistry Letters 2013, 4 (16), 2681-2685.

[27] Jung, S. C.; Han, Y.-K., Ab initio molecular dynamics simulation of lithiation-induced phase-transition of crystalline silicon. Electrochimica Acta 2012, 62, 73-76.

[28] Jung, S. C.; Choi, J. W.; Han, Y. K., Anisotropic volume expansion of crystalline silicon during electrochemical lithium insertion: an atomic level rationale. Nano Lett 2012, 12 (10), 5342-7.

[29] Huang, L.; Han, B.; Han, B.; Derecskei-Kovacs, A.; Xiao, M.; Lei, X.; O'Neill, M. L.; Pearlstein, R. M.; Chandra, H.; Cheng, H., First-Principles Study of a Full Cycle of Atomic Layer Deposition of SiO_2 Thin Films with Di(sec-butylamino)silane and Ozone. The Journal of Physical Chemistry C 2013, 130911145338002.

[30] Kim, S.-Y., and Yue Qi, Property evolution of Al_2O_3 coated and uncoated Si electrodes: A first principles investigation. Journal of the Electrochemical Society 2014, 161 (11), 7.

[31] Leung, K., First-Principles Modeling of the Initial Stages of Organic Solvent Decomposition on $Li_xMn_2O_4$ (100) Surfaces. The Journal of Physical Chemistry C 2012, 116 (18), 9852-9861.

[32] Karim, A.; Fosse, S.; Persson, K. A., Surface structure and equilibrium particle shape of the $LiMn_2O_4$ spinel from first-principles calculations. Physical Review B 2013, 87 (7).

[33] Kevin Tibbetts, C. R. M., Ying S. Meng, and Gerbrand Ceder, An Ab Initio Study of Lithium Diffusion in Titanium Disulfide Nanotubes. Chemistry of Materials 2007, 19, 8.

[34] Benedek, R.; Thackeray, M. M., Simulation of the surface structure of lithium manganese oxide spinel. Physical Review B 2011, 83 (19).

[35] White, D.; Seshadri, K. S.; Dever, D. F.; Mann, D. E.; Linevsky, M. J., Infrared Spectra and the Structures and Thermodynamics of Gaseous LiO, Li_2O, and Li_2O_2. The Journal of Chemical Physics 1963, 39 (10), 2463-2473.

[36] Li, S. F.; Lu, H.; Li, P.; Yang, Z.; Guo, Z. X., First-principles local density approximation (generalized gradient approximation) +U study of catalytic CenOm clusters: U value differs from bulk. J Chem Phys 2008, 128 (16), 164718.

[37] Nagai, Y., Nonaka, T., Suda, A., & Sugiura, M., Structure analysis of CeO_2-ZrO_2 mixed oxides as oxygen storage promoters in automotive catalysts. R&D Rev Toyota CRDL 2002, 37, 8.

[38] G. Kresse, J. F. l., Efficient iterative schemes for ab initio total-energy calculations using a plane-wave basis set. PHYSICAL REVIEW B 1996, 54.

[39] John P. Perdew, K. B., Matthias Ernzerhof, Generalized Gradient Approximation Made Simple. PHYSICAL REVIEW LETTERS 1996, 77.

[40] Jung, S. C.; Kim, H. J.; Choi, J. W.; Han, Y. K., Sodium ion diffusion in Al_2O_3: a distinct perspective compared with lithium ion diffusion. Nano Lett 2014, 14 (11), 6559-63.

[41] Schimmel, H. G.; Kearley, G. J.; Huot, J.; Mulder, F. M., Hydrogen diffusion in magnesium metal (phase) studied by ab initio computer simulations. Journal of Alloys and Compounds 2005, 404-406, 235-237.

[42] Ong, S. P.; Mo, Y.; Richards, W. D.; Miara, L.; Lee, H. S.; Ceder, G., Phase stability, electrochemical stability and ionic conductivity of the $Li_{10\pm1}MP_2X_{12}$(M = Ge, Si, Sn, Al or P, and X = O, S or Se) family of superionic conductors. Energy Environ. Sci. 2013, 6 (1), 148-156.

[43] Sahli, B.; Fichtner, W., Ab initiomolecular dynamics simulation of self-interstitial diffusion in silicon. Physical Review B 2005, 72 (24).

[44] Schoiswohl, J.; Kresse, G.; Surnev, S.; Sock, M.; Ramsey, M. G.; Netzer, F. P., Planar vanadium oxide clusters: two-dimensional evaporation and diffusion on Rh(111). Phys Rev Lett 2004, 92 (20), 206103.

[45] Hocker, S.; Gahler, F., Aluminium diffusion in decagonal quasicrystals. Phys Rev Lett 2004, 93 (7), 075901.

II. DISCOVERY OF AN UNEXPECTED METAL DISSOLUTION RESULT AND ITS THEORETICAL AND EXPERIMENTAL EXPLANATION

ABSTRACT

The degree of metal dissolution of cathode materials is a critical parameter in determining the performance of Lithium-Ion Batteries (LIBs). Ultra-thin coated cathode particles, via Atomic Layer Deposition (ALD), exhibited superior battery performance over that of bare particles. Therefore, it is generally believed that a coating layer protects the particles from the metal dissolution of active materials. However, surprisingly, we have observed that ultra-thin CeO_2 coating intensifies the Mn dissolution of $LiMn_2O_4$ (LMO) during cycling of LIBs, whereas ultrathin Al_2O_3 coating tends to inhibit the Mn dissolution. A detailed Density Functional Theory (DFT) study was carried out to explain these experimental observations. First, the manganese vacancy formation energy was calculated, along with the bonding strengths of Mn-O of uncoated, Al_2O_3 coated, and CeO_2 coated particles via Crystal Orbital Overlap Population (COOP) calculations. Further, the projected Density-of-States (DOS) calculation of Mn was used to confirm the electronic occupancy of the Mn atom for each case. All atomic and electronic analyses were consistent with the experimental observations. This is the first report of finding that coatings can accelerate metal dissolution, and of providing new insights into the impact of ALD coatings on metal dissolution in cathode materials.

1. INTRODUCTION

Interfacial electrochemical activities that steer the maximization of energy density are critical for improving energy storage technology. However, unavoidable side reactions overshadow the necessary surface reactions and lead to the devaluation of batteries. An ideal cathode material should possess high operating potential, superior capacity, a long life cycle, and a sufficiently broad range of working temperatures. Although metal oxide cathodes satisfy the criteria, they suffer from an inevitable degradation process. Manganese is an excellent candidate for intensive study of the fundamental interfacial processes and side reactions at cathode surfaces because of its low toxicity, low cost, and high natural abundance of Mn[1-9]. Despite capacity improvements, poor cycling performance still stands in the way of wide applications of $LiMn_2O_4$ (LMO) material[10-14]. It has been published that Mn dissolution accounts for 23% and 34% of overall capacity degradation at room temperature and at 55 ^oC[15]. The major reason for LMO degradation has been identified as structural changes in the material due to phase transformations, alternation of intrinsic properties (such as electronic and ionic conductivity), dissolution of transition metal ions, and increases in polarization voltage. Previous studies have shown that poor cycling performance can be directly associated with the disproportion reaction of manganese, especially at an elevated temperature[15]. In bulk LMO, a mixed Mn^{3+} and Mn^{4+} oxidation state exists, where Mn^{3+} is the main culprit for dissolution. Several efforts have been made to explore this dissolution mechanism to find a way to minimize the dissolution impact on cycle life. It has been reported that the covalent nature of a Mn-O bond has a direct impact on

metal-ion dissolution[16,17]. The Mn-O bond is distorted, due to the dissolution of the Mn^{2+} ions, resulting in a change in the Mn charge densities. Typically, Mn^{4+} with a t_{2g} electron configuration and MnO_2 are highly stable. A Jahn-Teller distortion is mainly associated with high-spin Mn^{3+} (t_{2g}^3 e_g^1) ions, which induces huge volume changes and severely diminishes capacity.

Several strategies, such as reduction of particle size[18] and surface modification of the active materials powder by coating have been proposed in order to overcome the dissolution process. In particular, surface modification through the atomic layer deposition method, where atomically thin layers of metal oxides can be controlled when deposited[19], has shown significant improvement both in capacity and in life cycle. Stable metal oxides, such as ZnO, ZrO_2, SiO_2, TiO_2, $AlPO_4$, Al_2O_3, and CeO_2 notably improved battery performance[20-40] and, as a result, it is believed that ALD coating strategies may preserve and stabilize cathode particles. For dissolution, although the impact of coating on metal dissolution has not been specifically studied, it is generally believed that it protects particles from dissolution[27,28,41-45]. In literature, first-principles simulations were carried out to study the Mn dissolution of LMO[17,46,47]. For the coating experiments, although the addition of an Al_2O_3 coating layer presumably inhibited Mn dissolution, it was also found that excess Al_2O_3 can sometimes act as an insulator and increase the charge transfer resistance, worsening the performance[48]. Moreover, various metal oxide coating layers have different influences on cycling performance and rate capability, while excessive ALD cycles can lead to lesser rate capability for any metal oxide[42]. A previous work has shown that a CeO_2 coating

enhances battery performance more than an Al_2O_3 coating, and it has been proved that this was due to its higher ionic conductivity and better mechanical protection[25]. However, the coating impact on metal dissolution was not studied.

In this work, we investigated the possible reduction of metal dissolution after CeO_2 and Al_2O_3 ALD coatings. Much to our surprise, we found, from our experimental results, that the CeO_2 coating layer does not suppress metal dissolution but, instead, has a rather complex role in accelerating the dissolution process. In the case of the Al_2O_3 coating, however, the metal dissolution decreased. To date, no observations and no explanations have been made concerning this phenomenon. In order to gain a better understanding of this unexpected result, a detailed Density Functional Theory (DFT) analysis was carried out. First, the manganese vacancy formation energy, which can provide a clear understanding of how Mn atoms easily break their bonds and become isolated from the bulk, was analyzed by comparing the manganese vacancy formation energies of Al_2O_3 and CeO_2 coated and uncoated particles. Next, as the metal dissolution is critically affected by the bonding strength with the surrounding atoms, the Crystal Orbital Overlap Population (COOP) analysis was conducted by focusing on the characterization of their bonding and anti-bonding behavior. Furthermore, the electronic structure of Mn is strongly associated with the metal dissolution and Jahn-Teller distortion. For this, a Projected Density of State (PDOS) analysis was conducted with different coating materials and thickness.

Lastly, to understand the impact of dissolution on battery performance, battery cycling performance was measured by focusing on a high temperature operation, in which metal dissolution was intensified. All experimental observations, including metal

dissolution and battery performance, was consistent with the theoretical explanations. Although our initial observation was unexpected, we have clearly identified the origin of the behavior. This is the first report to identify the effect of coating on dissolution and to provide a theoretical basis for the selection and fabrication of optimal coating material for high performance LIBs.

2. RESULTS AND DISCUSSION

2.1. MN DISSOLUTION EXPERIMENT

The Mn dissolution experiment was conducted with uncoated LMO (U-LMO) particles and different thickness coatings including 1.5nm and 3nm thick Al_2O_3 coated LMO (A-LMO) particles, and 1.5nm and 3nm thick CeO_2 coated LMO (C-LMO) particles. The Transmission Electron Microscopy (TEM) was used to study the microstructure of C-LMO particle surface. TEM image of 100 cycles C-LMO is shown in Fig. 1. From the TEM image, an ultrathin and uniform CeO_2 layer can be clearly observed on the top of the surface of the LMO particle. For the dissolution measurement, a separator was used to wrap powders, which was then soaked in electrolyte. The samples were put at room temperature and 55 °C for two weeks and four weeks, respectively. Then, the Inductively Coupled Plasma - Optical Emission Spectroscopy (ICP-OES) was used to measure the amount of dissolved Mn at different conditions. As shown in Fig. 2A, the Mn concentration of U-LMO was 14.00 –18.00 ppb after 2 weeks and 16.00 – 19.00 ppb after 4 weeks. The Mn concentration of 3 nm A-LMO and 3 nm CLMO ranged in 5.00 – 7.71 ppb, and 34.47 – 43.13 ppb, respectively, after 2 weeks. After 2 weeks more (4 weeks later), the Mn dissolution concentration increased to 6.70 –

9.66 ppb and 53.13 - 68.17 ppb, respectively. Further, as expected, the dissolution increased more at a high temperature than at room temperature. It was observed that the Mn concentrations of U-LMO, ALMO, and C-LMO were in the range of 15.62 – 137.73 ppb, 21.23 – 90.45 ppb, and 71.55 – 542.41 ppb at room temperature, and 245.52 – 349.51 ppb, 282.13 – 240.27 ppb, and 1275.9 – 1462.0 ppb at 55 °C. (Fig. 2B).

The impact of coating thickness on Mn dissolution was also studied by changing ALD coating thickness from 3.0 nm to 1.5 nm. As shown in Fig. 2A, it was observed that the Mn concentrations of 1.5nm A-LMO and 1.5nm C-LMO were 9.00 – 11.00 ppb and 32.00 – 36.00 ppb after 2 weeks, and 10.00 -12.00 ppb and 43.00 – 57.00 ppb after 4 weeks. It was also found that the Mn concentration of U-LMO, 1.5nm A-LMO, and 1.5nm C-LMO were 9.00 – 14.00 ppb, 2.00 – 4.00 ppb, and 37.00 – 51.00 ppb at room temperature, and 1182 – 1781 ppb, 419 – 947 ppb, and 1493 – 2247 ppb at 55 °C (Fig. 2B).

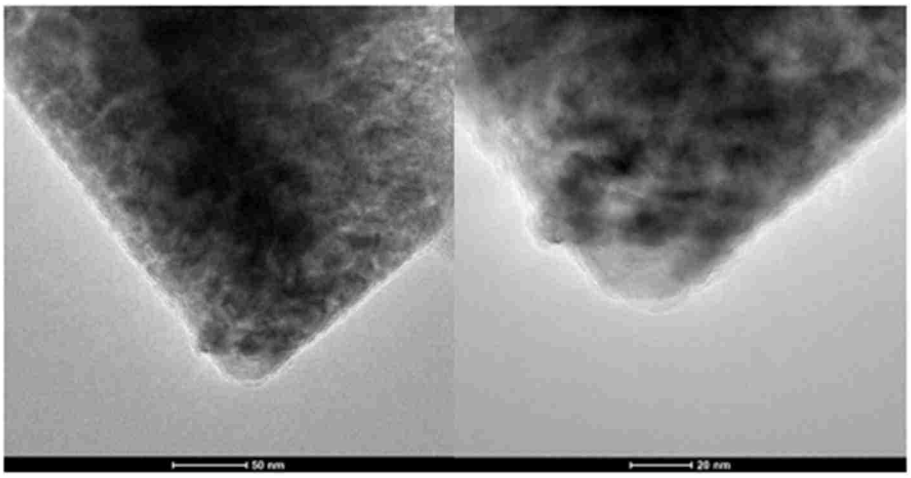

Figure 1. TEM image of LMO coated with 100 cycles (~5 nm thick CeO_2 film) ALD CeO_2 layers.

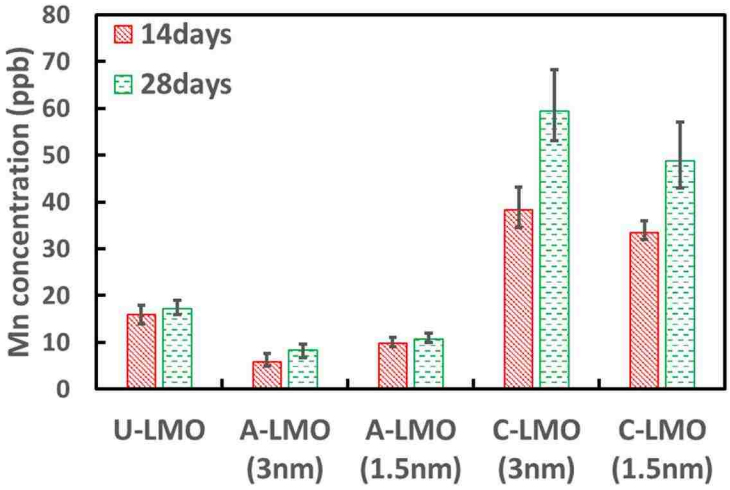

(A)

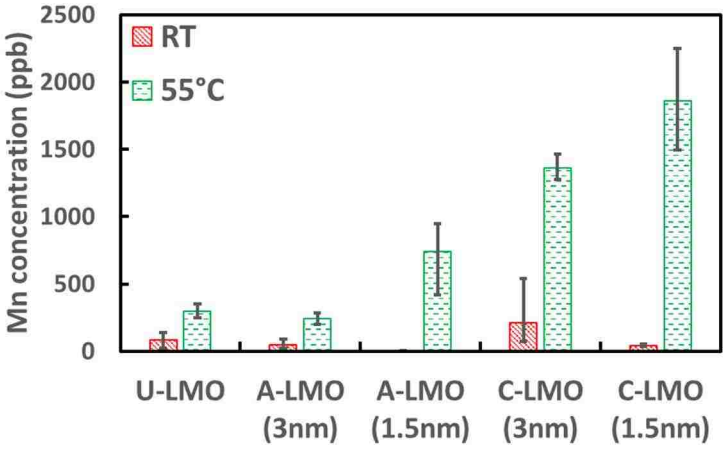

(B)

Figure 2. Mn dissolution experiment for U-LMO, 1.5 (3.0nm) ALD A-LMO and 1.5(3.0nm) ALD C-LMO. (A) Mn concentration after 2 weeks and 4 weeks. (B) Mn dissolution at 25ºC and 55ºC after one week.

In summary, the Mn dissolution of C-LMO was the highest and A-LMO was the lowest for all conditions, including temperature, time, and the thickness of the coating

layer. Also, when the time and temperature increased, the Mn dissolution of all samples increased. For the impact of coating thickness, the Mn dissolution of A-LMO decreased as the ALD coating thickness increased, while Mn dissolution of C-LMO increased as the coating thickness increased. The ALMO had less Mn dissolution than U-LMO did, which agreed with previous studies[48,49]. In the case of C-LMO, however, results differed from those of a previous study[28], although, in that case, the effect of dissolution of CeO_2 coating was found only at a high temperature, and the coating method and thickness were different from those used in this study. To confirm the authenticity of our experimental results and to find out why CeO_2 coating intensifies the Mn dissolution of active material, first-principles calculations were performed.

2.2. SURFACE ENERGY

Surface energy is an indication of the relative stability of different facets and terminations in a material. LMO structure has several possible orientations and terminations[46]. 001 orientation has two possible planes, which consist of Li_2 termination and Mn_4O_8 termination. 110 orientation also has two possible planes which include MnO_2 termination and $LiMnO_2$ termination. 111 orientation has three possible planes which consist of Mn termination, Mn_3 termination, and O_4 termination. A previous study[46] showed that on 001 orientation of LMO structure, the Li_2 termination was more stable than the Mn_4O_8 termination. On 110 orientation of LMO structure, the MnO_2 termination structure was more stable, and the Mn terminated structure was the most stable structure among 111 orientation of LMO. Therefore, in this study, we only considered Li terminated 001 surface, MnO_2 terminated 110 surface, and Mn terminated

111 surface. To study the surface stability of several possible LMO surface orientations, the surface energy of 001_Li_2, 110_MnO_2, and 111_Mn were calculated. The most stable configuration was then used for the Mn vacancy formation energy calculation, COOP analysis, and PDOS analysis. As shown in Table 1, surface energy of (001)LMO, (110)LMO, and (111)LMO structure were 0.557 J/m^2, 1.218 J/m^2, and 0.814 J/m^2 by considering ferromagnetic ordering (FM) and 0.530 J/m^2, 1.267 J/m^2, 0.850 J/m^2 by considering antiferromagnetic ordering (AFM), which were consistent with the previous reported values[46]. By comparing the surface energy of three LMO surface orientations, (001) LMO had the lowest surface energy. Based on those results, Li terminated (001) LMO was identified as the most stable structure among three different surface orientations. Also, the surface energies differences between three different orientations were practically similar by considering FM and AFM order. Therefore, for the next calculation, only FM was considered.

Table 1. The surface energy of LMO with 001, 110 and 111 surface orientation.

Structure	Ferromagnetic ordering (J/m^2)	Antiferromagnetic ordering (J/m^2)
(001)$LiMn_2O_4$	0.557	0.530
(110)$LiMn_2O_4$	1.218	1.267
(111)$LiMn_2O_4$	0.814	0.850

2.3. MN VACANCY FORMATION ENERGY

The Mn vacancy formation energy was used to study the Mn dissolution of the U-LMO, A-LMO, and C-LMO structures. Mn vacancy formation energy is defined as the amount of energy required for a Mn atom to break its bond with the structure. A higher Mn vacancy formation energy indicates that it is harder for a Mn atom to escape from the structure by breaking its bond with the surrounding atoms. Figure 3 is a schematic diagram that depicts the energy required for removal of one Mn atom from the LMO. The U-LMO, A-LMO, one layer C-LMO coated LMO and two layer C-LMO configuration used for calculation are shown in Fig. 4. It was found that the Mn vacancy formation energy of U-LMO, A-LMO, and C- LMO were 8.91eV, 11.71eV, and 6.49eV, respectively (Table 2). The Mn vacancy formation energy of C-LMO was the lowest while that of A-LMO was the highest, which indicated that CeO_2 coating intensified Mn dissolution while Al_2O_3 coating could prevent Mn dissolution of LMO particles. From the Mn dissolution experiment results, we also found that the Mn dissolution varied, depending on the thickness of the ALD coating. To study the fundamental reason behind this, two different CeO_2 coating layers were considered as shown in Fig. 4. It turned out that the Mn vacancy formation energy of the LMO structure with two CeO_2 layers was 6.49eV, which was lower than the 7.40eV for only one CeO_2 layer (Table 3). This suggested that, when CeO_2 coating thickness increased, the Mn dissolution was intensified. This simulation result was consistent with the experimental observation in which a thicker coating layer intensified the dissolution.

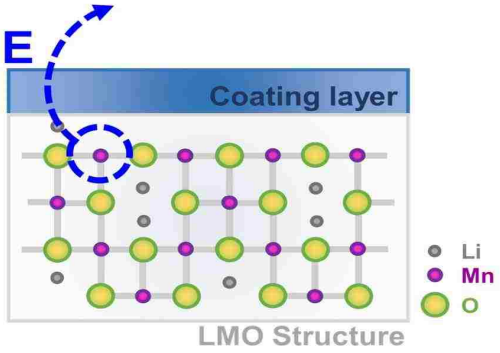

Figure 3. Schematic diagram depicting the energy (E) required for removal of one Mn atom from LMO system.

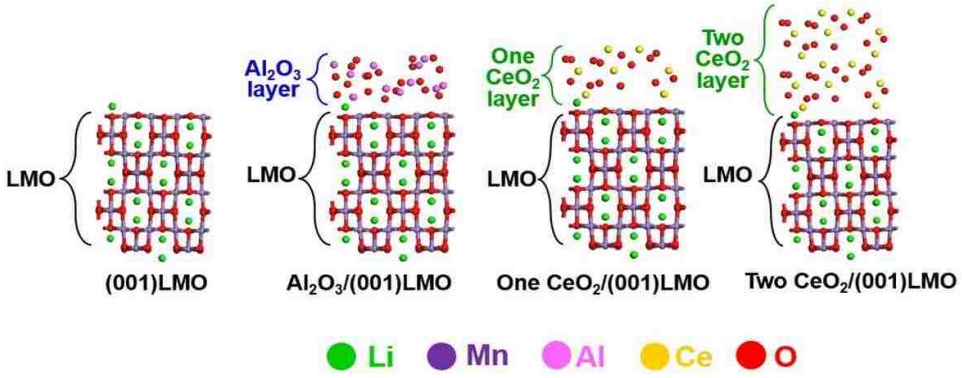

Figure 4. Uncoated LMO, Al_2O_3 layer coated LMO, one CeO_2 layer coated LMO and two CeO_2 layer coated LMO configurations used for calculations.

Table 2. Manganese vacancy formation energy of LMO, A-LMO and C-LMO.

Structure	E_F (eV)
U-LMO	8.91
A-LMO	11.71
C-LMO	6.49

Table 3. Manganese vacancy formation energy of (001) LMO as a function of CeO_2. coating thickness.

Structure	E_F (eV)
One CeO_2 coated LMO	7.40
Two CeO_2 coated LMO	6.49

2.4. COOP (CRYSTAL ORBITAL OVERLAP POPULATION) ANALYSIS

Mn dissolution is significantly affected by its bonding status with surrounding elements[50]. Therefore, first, we measured the bonding lengths between Mn-O, Mn-Mn, and Mn-Li in U-LMO, A-LMO, and C-LMO directly. Figure 5 shows the bonding length between Mn-O around the surface of coating layer for U-LMO, ALMO, and C-LMO. As listed in Table 4, the average Mn-O bond length increased significantly after coated with CeO_2 while that of Al_2O_3 coated LMO decreased. In particular, there was an outstanding difference in bonding length of the atoms on the surface, which indicated the coating strongly impacts the atoms near the coating layer. Next, a COOP and an integrated COOP analysis were conducted to analyze the bonding and antibonding nature of the molecular orbitals for particular pairs of atoms (e.g., Mn-O, Mn-Mn, Mn-Li). For instance, a positive value of COOP means a bonding state, while a negative value means an anti-bonding status. The integrated COOP (ICOOP), at a specific energy level, shows the total bonding strength below this energy level. A higher integrated COOP value means that it has a stronger bonding strength. As shown Fig. 6A, when A-LMO and C-LMO are compared, the COOP value of Mn-O shows that the A-LMO has more bonding state and less antibonding state and, conversely, C-LMO has less bonding state and more

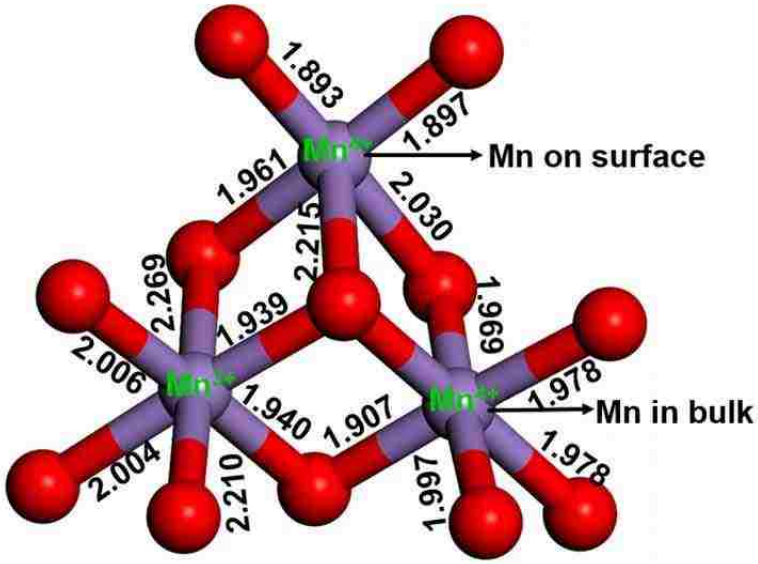

(A) LMO

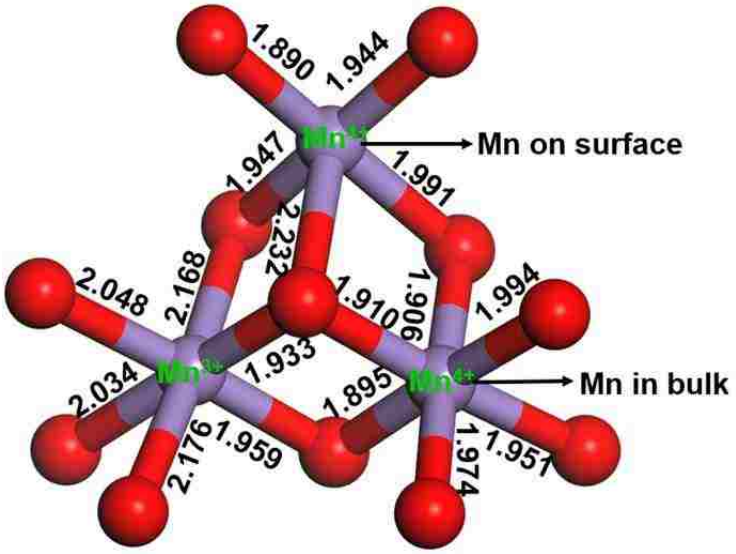

(B) Al_2O_3 coated LMO

Figure 5. Bond length between Mn-O in LMO, Al_2O_3 coated LMO and CeO_2 coated LMO.

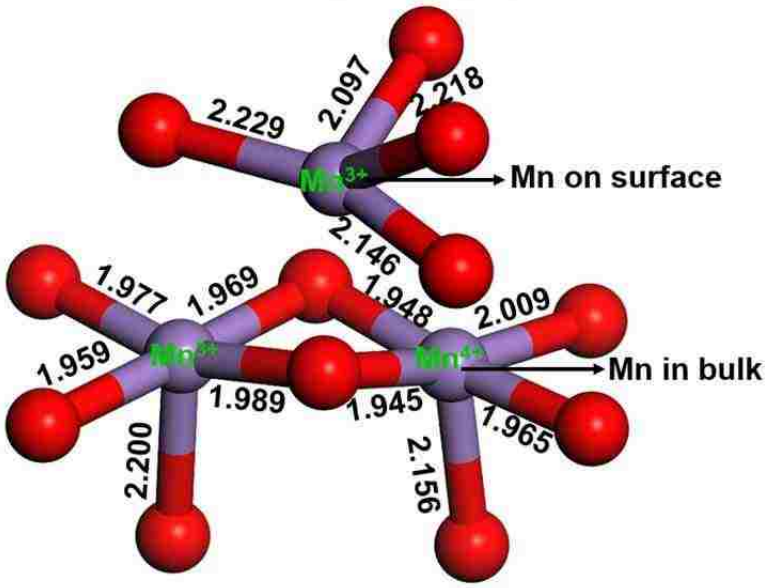

(C) CeO_2 coated LMO

Figure 5. Bond length between Mn-O in LMO, Al_2O_3 coated LMO and CeO_2 coated LMO (cont.).

Table 4. Average bond length of Mn-O in LMO, A-LMO and C-LMO.

Bond length(Å)	U-LMO	A-LMO	C-LMO
Mn on surface	2.000	2.000	2.170
Mn in bulk (average)	2.010	1.995	2.015
Average bond length	2.007	1.997	2.067

antibonding state compared with U-LMO. Figure 6B indicates the same conclusion in overall energy levels. The bonding characterization for other atomic interactions (Mn-Mn, Mn-Li) reached the same conclusions as the Mn-O bonding (supporting materials).

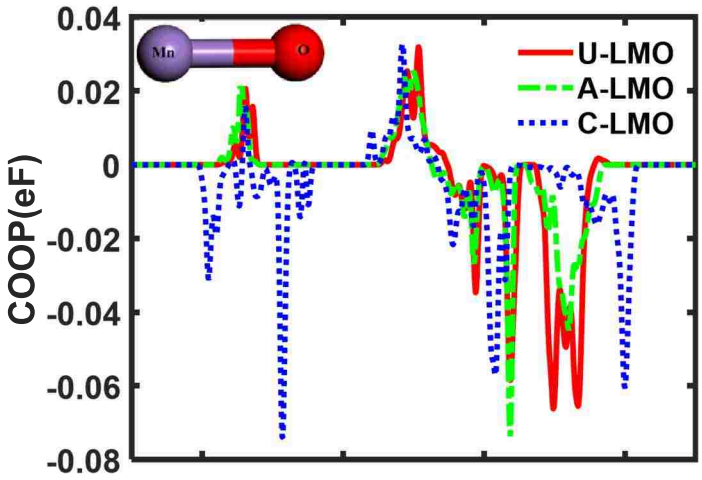

(A)

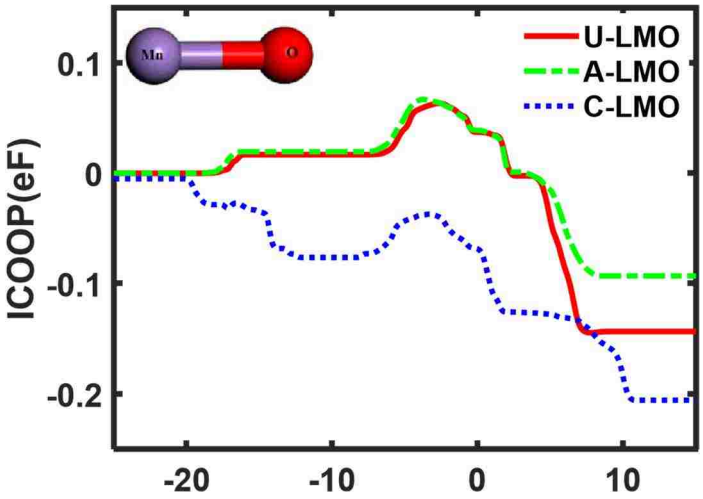

(B)

Figure 6. COOP (A) and ICOOP (Integrated Crystal orbital overlap population) (B) of Mn-O bond of uncoated LMO, Al_2O_3 coated LMO and CeO_2 coated LMO.

2.5. PDOS ANALYSIS

The Mn dissolution is also affected by the electronic property of Mn, as previous studies have reported[17,51-54]. The electronic orbital configuration for oxidation of Mn^{3+} is depicted in Fig. 7. The electronic configuration of Mn^{3+} has three electrons in the t_{2g} orbital and one electron in the e_g orbital. In the e_g orbital, one electron occupies either the d_{x2-y2} or d_{z2} orbital, which causes the degeneracy of the two orbitals broken down, leading to Jahn-Teller distortion. Therefore, the presence of the Mn^{3+} state is strongly related to the dissolution[38–40]. In order to understand the Mn electronic properties of U-LMO, A-LMO, and C-LMO the Projected Density of States (PDOS) analysis based on first-principles calculations was conducted. The DOS describes the number of states per an interval of energy, at a certain energy level where it can be occupied by electrons. In Fig. 8, the positive PDOS value indicates the up-spin direction of the electrons and the negative PDOS value means the down-spin direction of the electrons. In e_g orbitals, it was found that the energy of Mn on U-LMO surface had a PDOS peak of around 4eV, the energy of Mn on A-LMO surface had a PDOS peak of around 4.25eV, while the energy of Mn on C-LMO surface had a PDOS peak of around 3.25eV above the Fermi level. The lower energy of the PDOS peak suggested that it was more likely for an electron to occupy e_g orbital. Therefore, there was a higher probability of Mn^{3+} in the structure. From PDOS analysis, it was confirmed that the CeO_2 coating could heighten Mn dissolution of a LMO active material, while Al_2O_3 coating could diminish Mn dissolution, which corroborates Mn vacancy formation energy results and Mn dissolution experimental results. For the thickness impact, PDOS analysis showed the same results as the experimental observation: as shown in Fig. 2, when ALD CeO_2 coating thickness

increased from 1.5nm to 3.0nm, the amount of dissolved Mn increased. For PDOS case, as shown in Fig. 9, two layers of C-LMO shows a PDOS peak of around 3eV that are lower than that of one layer of C-LMO. Thus, when CeO_2 coating thickness increased, the Mn dissolution increased, which agreed well with the experiment results.

So far, all discussion was focused on the particle level. In order to understand how the particlelevel dissolution affect the cell-level performance, battery cells were fabricated by using LMO, A-LMO, and C-LMO. In the previous work[25], in which C-LMO showed the best performance at room temperature. The improved transport properties and mechanical protection from the CeO_2 coating were the main reasons for that improvement. At high temperatures, however, Mn dissolution significantly accelerates and become the most important degradation mechanism. The discharge capacity of U-LMO, A-LMO, and ALD C-LMO at a 1C rate between 3.4 - 4.5V, at room

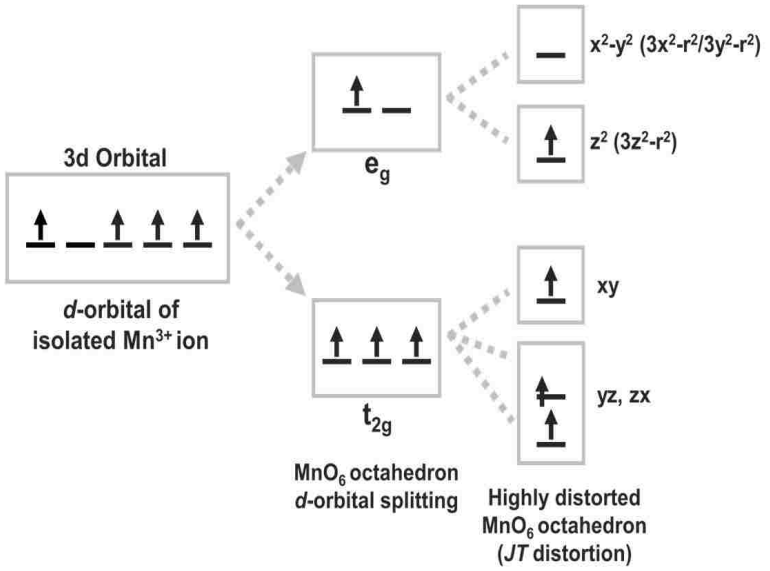

Figure 7. Electronic orbital configuration for oxidation of Mn^{3+}.

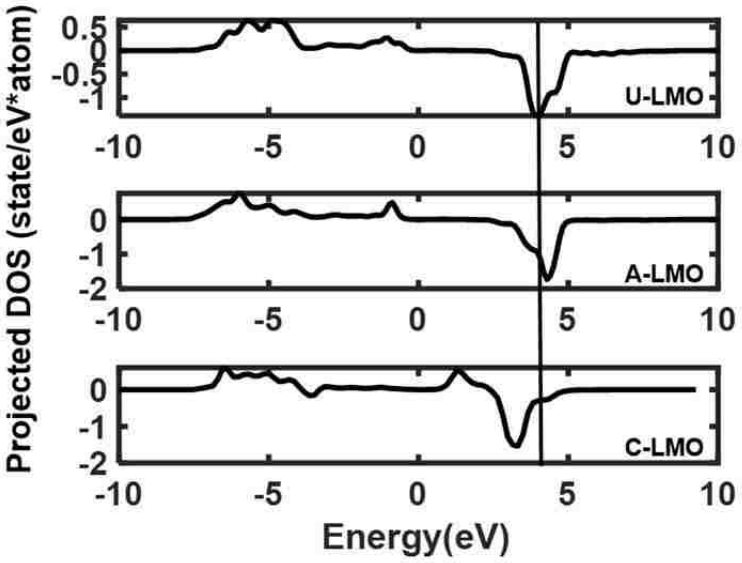

Figure 8. Projected density of state of Mn in uncoated LMO, Al_2O_3 coated LMO and CeO_2 coated LMO surface in e_g orbitals.

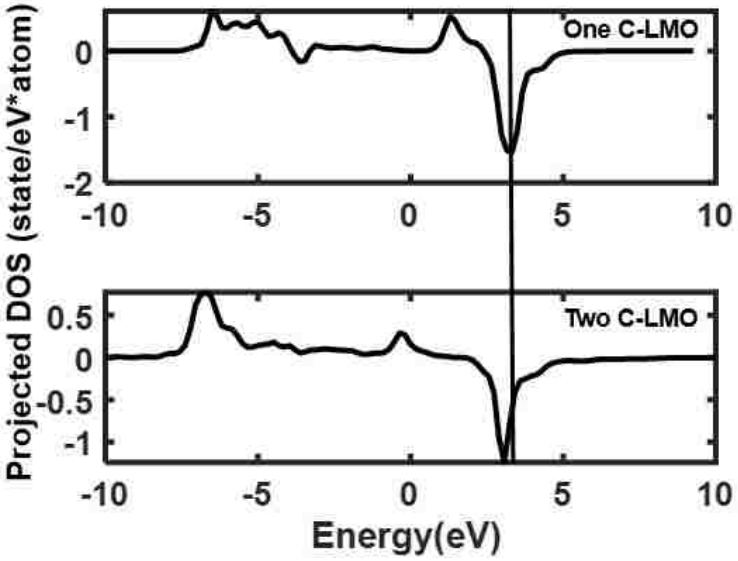

Figure 9. Projected density of state of one CeO_2 layer and two CeO_2 layers coated LMO surface and bulk in e_g orbitals.

temperature and an elevated temperature (55°C), are shown in Fig. 10. First, for all cases, the discharge capacity at 55°C was much lower than the values at room temperature, which was mainly attributed to the accelerated Mn dissolution. Dissolved Mn degrades battery performance in several ways, including capacity loss, reduced transport properties due to loss of contact between particles, and deposition to anode sides. Consequently, the capacity of a battery reduces gradually. A battery composed of LMO cathode material and graphite anode, in general, shows three stages of capacity fade upon long-term cycling: acceleration, stabilization, and saturation[55]. In the first stage, capacity fade mainly results from Solid Electrolyte Interphase (SEI) layer growth. After a SEI layer is stabilized, the cathode Mn dissolution-induced capacity loss outpaces the

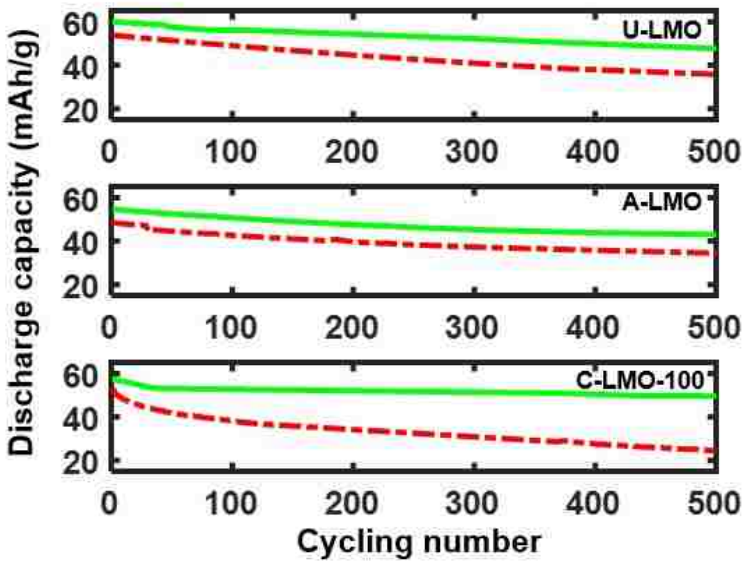

Figure 10. The discharge capacity of uncoated LMO, 5 cycles Al_2O_3 coated LMO and 100 cycles CeO_2 coated LMO at room temperature (green solid line) and 55 °C (red dashed line).

capacity fade due to SEI layer formation and growth. In this saturation stage, cathode capacity degrades further and becomes the limiting factor. However, at high temperature, the Mn dissolution-induced capacity begins to fade at a very early stage. This can be confirmed from Fig. 11, which shows the capacity fade rate for three cases. First, at room temperature, C-LMO showed the lowest degradation rate, which was consistent with the previous measurement[25]. Also, the poor rate performance with A-LMO was observed, as before. However, at an elevated temperature, the accelerated dissolved Mn in C-LMO resulted in the highest capacity fade rate. Meanwhile, unlike the room temperature results, A-LMO showed the lowest capacity rate. This was consistent with the Mn-dissolution measurement results discussed earlier. Therefore, the observed intensified Mn-dissolution, depending on the coating material, was confirmed in several ways,

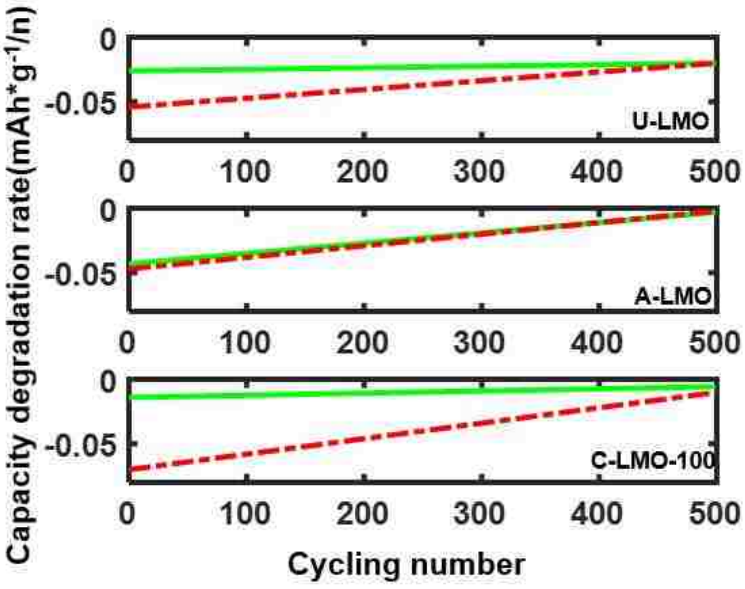

Figure 11. The discharge capacity degradation rate of uncoated LMO, 5 cycles Al_2O_3 coating LMO and 100 cycles CeO_2 coated LMO at room temperature (green solid line) and 55^0C (red dashed line).

including ICP-OES measurement, metal vacancy formation energy calculation, COOP analysis, PDOS analysis, and battery cell performance. This is not only the first report of this observation, but it also provides the explanation for the unexpected results that will serve as very useful guidance for advanced strategies with coatings.

3. METHODOLOGY

3.1. ALD COATING PREPARATION

ALD technology is an ultrathin film deposition technology, which is an experienced method for producing ultra-thin and conformal films at the nanometer scale[56-58]. ALD film deposition is based on two half self-limiting reactions between gas precursor molecules and a solid substrate surface. In this work, ALD was performed in a home-made fluidized-bed reactor[59]. Trimethylaluminum (TMA, Sigma Aldrich) and deionized water precursor were used for ALD Al_2O_3 coating. Tris(i-propylcyclopentadienyl)cerium(III) ($Ce(iPrCp)_3$, Strem Chemicals) and deionized water precursor were used for ALD CeO_2 coating. Surfaces of $LiMn_2O_4$ (LMO) particles served as the depositing substrate. During the Al_2O_3 (CeO_2) ALD process, precursor TMA ($Ce(iPrCp)_3$) was absorbed on the LMO substrate, resulting in the self-termination of one monolayer. The deionized water precursor then reacted with the new substrate, which was deposited as another monolayer. The ALD processes were conducted at 250°C for both ALD Al_2O_3 and CeO_2 films. Through repeating the binary reaction, an appropriate film thickness could be achieved (10 cycles for 1.5nm Al_2O_3, 25 cycles for 3nm Al_2O_3, 30 cycles for 1.5nm CeO_2, and 50 cycles for 3nm CeO_2). During each half-reaction, the precursor was pulsed into the chamber under vacuum for a specified period of time to

allow the precursor to fully react with the substrate surface. For Al_2O_3, TMA and deionized water were evaporated at room temperature without any carrier gas. The feed lines were kept at ~110 °C to avoid any condensation. For CeO_2, $Ce(iPrCp)_3$ was evaporated at 140 °C with N_2 as carrier gas, and the feed lines were kept at ~150 °C.

3.2. MN DISSOLUTION SAMPLE PREPARATION

The Al_2O_3 coated LMO (A-LMO), and CeO_2 coated LMO (C-LMO) samples at varying coating thicknesses were prepared for Mn dissolution testing by wrapping 0.03g of the coated powders in a porous Celgard-2320 separator consisting of a 20 μm thick trilayer film of polypropylene (PP)/polyethylene (PE)/PP. Sixteen samples were prepared for each case, which included uncoated LMO (U-LMO), 1.5nm and 3nm thick A-LMO, and 1.5nm and 3nm thick C-LMO, where four samples from each case were tested for 2 week dissolution, four for 4 week dissolution, four for room temperature dissolution, and four for 55ºC dissolution. All wrapped samples were immersed in 2.5ml tube of $LiPF_6$ electrolyte in a 1:1 volume ratio of ethylene carbonate and dimethyl carbonate. Finally, the solutions were diluted into a ratio of 1:1000 to milli-Q water and an inductively coupled plasma optical emission spectroscopy (ICP-OES) experiment was conducted to measure the amount of dissolved Mn in the electrolyte.

3.3. INDUCTIVELY COUPLED PLASMA OPTICAL EMISSION SPECTROSCOPY (ICP-OES) MEASUREMENT

ICP-OES is an efficient analytical technique used for metal species identification and quantitative analysis at low sample concentration (part per quadrillion, ppq). When operating the ICP-OES machine, the sample solution was delivered to a nebulizer from

tubes via a peristaltic pump. The nebulizer was used to transform the sample solution into a sample aerosol. The sample aerosol was then introduced to the torch, which consisted of induction coil wrapped around a concentric quartz. The argon gas flowed continuously through the torch and a Radio Frequency (RF) generator provided power to the RF coil at oscillating frequencies. The torch spark ionized some of the argon gas, from which the cations and electrons were produced. The cations and electrons collided with other argon molecules at high speed and high temperature was created. The argon gas became electrically conductive, which would then form plasma. The sample aerosol that entered the high temperature plasma and absorbed energy became excited and emitted light at a specific wavelength. This light was collected by a spectrometer and passed through a diffraction grating. The diffracted light was collected by wavelength and converted to an elemental concentration that compared with calibration Mn standards. Mn standards were prepared in 1% HNO_3 with a concentration ranging from 0.01mg/L to 100mg/L.[60,61]

3.4. BATTERY PERFORMANCE MEASUREMENT

The slurry was prepared through mixing a $LiMn_2O_4$ (LMO) active material, carbon black, and polyvinylidene fluoride at a weight ratio of 80:10:10 in N-methyl-2-pyrrolidone solvent. The mixed slurry was cast onto aluminum foil using a doctor blade and then dried in a vacuum oven at 120°C for 8h. The obtained dried cast was punched into a 14mm disk for cell assembly in CR2032 coin cells were assembled to test the electrochemical behaviors of the prepared electrode. Lithium metal foil (Sigma-Aldrich, 99.9%) was used as the counter electrode. A Celgard-2320 separator and 1.0 M $LiPF_6$ in

ethylene carbonate, dimethyl carbonate, and diethyl carbonate (1:1:1 volume ratio) electrolyte were used during cell-assembly. All CR2032 coin cells were assembled in an argon-filled glove box. The prepared cells were tested for charge-discharge cycling performance at 1C rate using a battery tester, from Neware Corporation, at a cut-off voltage of 3.4-4.5V.[25]

3.5. THEORETICAL CALCULATIONS

To study the reason why CeO_2 coating intensifies Mn dissolution, first-principles calculations were performed by using the Vienna Ab initio Simulation Package (VASP) code[62]. The projectoraugmented wave method[63] was used for electron and core interaction. The PBE (Perdew–Burke–Ernzerhof) was used to approximate the exchange and correlation functional. The U value (GGA+U) 4.84 eV was used for LMO in all calculations to correct the delocalization of the 3d electron states of Mn. The LMO slab structure consisted of 16Li, 32Mn and 64O. All calculations were ensured with an energy convergence. A 600 eV cutoff energy was used for all structural relaxation and total energy calculation and 1 × 1 × 1 of a Gamma-centered grid was used. The (001), (110), and (111) surface planes were prepared for the LMO structure. During surface energy calculation, ferromagnetic (FM) and antiferromagnetic (AFM) of Mn atoms were considered. After finding the most stable LMO surface plane, Mn vacancy formation energy, the projected density of states (PDOS), and COOP of Mn were calculated to study the effect of different ALD coating materials and coating thicknesses. When considering the impact of CeO_2 coating thickness on Mn dissolution during simulation,

CeO_2 coatings with different thicknesses were placed on top of the LMO surface. One CeO_2 coating layer included 7Ce, 14O, and one Al_2O_3 coating layer included 12Al, 18O.

3.6. SURFACE ENERGY

Surface energy is the energy difference between slab structure and bulk structure. Smaller surface energies are more energetically stable. To identify the most stable configuration of several possible LMO surface orientations, the surface energy was calculated for 001_Li_2, 110_MnO_2, and 111_Mn, three different surface orientations of LMO structure. Surface energy is expressed as follows[46,64]:

$$\sigma = (E_{slab} - NE_{bulk})/2A \quad (1)$$

where E_{slab} is the total energy of a surface slab with a top and a bottom surface, E_{bulk} is the bulk energy per formula unit, N is the number of chemical formula units in the slab, and A is the surface area of the slab.

3.7. MN VACANCY FORMATION ENERGY

Mn vacancy formation energy is defined as the amount of energy required to break a bond from a structure. A higher Mn vacancy formation energy indicates that it becomes difficult for Mn to break off from the structure. The vacancy formation energy expression is defined as follows[64,65]:

$$E_F = 1/M(E[Li_N Mn_{2N-M} O_{4N}] - NE[LiMn_2 O_4] + u_{Mn} \quad (2)$$

where E_F is the Mn vacancy formation energy, N is the number of chemical formulas in the structure, M is the Mn deficiency number, and u_{Mn} is the chemical potential of Mn.

The average value of chemical potential of Mn at 0 K in the stable region of the Li-Mn-O was about -4.5eV[66].

3.8. COOP (CRYSTAL ORBITAL OVERLAP POPULATION) ANALYSIS

The COOP diagram was used to investigate the bonding property of Mn in structure. The LOBSTER software was used to calculate COOP, using required output files from the VASP package. The COOP was calculated by using static calculation with 6 × 6 × 1 Monkhorst-Pack mesh. The bonding information was obtained from the COOP diagram and integrated COOP diagram. The positive COOP value indicated a bonding state while the negative COOP value suggested an anti-bonding state. Bonding interaction led to lower system energy. Likewise, an antibonding COOP stood for a higher system energy. From the summation of all COOP values under the Fermi energy, which was an indicator of the covalent character of a chemical bonding.[17]

3.9. PDOS ANALYSIS

The electronic properties and oxidation state of Mn in the U-LMO, A-LMO, and C-LMO were investigated using first-principles calculations. Mn dissolution is related to the electronic properties of Mn^{3+}. There are four electrons in d orbital of Mn^{3+}. Three electrons occupy d_{xy}, d_{xz} and d_{yz} orbitals, respectively, in t_{2g} orbital. The one extra electron occupies either d_{x2-y2} or d_{z2} in e_g orbital. Therefore, an electronic property study of Mn^{3+} in eg orbital was sufficient because t_{2g} orbital was almost always stable. PDOS was calculated by using a static calculation with 3 × 3 × 1 Monkhorst-Pack mesh. The impact of the thickness of a CeO_2 coating was also investigated via PDOS.

REFERENCES

[1] Julien, C. M., Alain Mauger, Karim Zaghib, and Henri Groult. . Comparative issues of cathode materials for Li-ion batteries. Inorganics 2, doi: 10.3390/inorganics2020132 (2014).

[2] Lee, M. J., Lee, S., Oh, P., Kim, Y. & Cho, J. High performance $LiMn_2O_4$ cathode materials grown with epitaxial layered nanostructure for Li-ion batteries. Nano Lett 14, 993-999, doi: 10.1021/nl404430e (2014).

[3] Tan, C. L. et al. Performance improvement of $LiMn_2O_4$ as cathode material for lithium ion battery with bismuth modification. Journal of Power Sources 184, 408-413, doi:10.1016/j.jpowsour.2008.04.019 (2008).

[4] Wang, H.-Q. et al. Excellent stability of spinel $LiMn_2O_4$-based cathode materials for lithium-ion batteries. Electrochimica Acta 177, 290-297, doi:10.1016/j.electacta.2015.02.027 (2015).

[5] He, X., Li, J., Cai, Y., Jiang, C. & Wan, C. Preparation of spherical spinel $LiMn_2O_4$ cathode material for Li-ion batteries. Materials Chemistry and Physics 95, 105-108, doi:10.1016/j.matchemphys.2005.06.006 (2006).

[6] Thackeray, M. M., & De Kock, A. Synthesis of γ-MnO_2 from $LiMn_2O_4$ forLi/MnO_2 battery applications. Journal of Solid State Chemistry 74, 5 (1988).

[7] Rao, M. M., Jayalakshmi, M., Schäf, O., Wulff, H., Guth, U., & Scholz, F. Electrochemical behaviour of solid lithium cobaltate ($LiCoO_2$) and lithium manganate ($LiMn_2O_4$) in an aqueous electrolyte system. Journal of Solid State Electrochemistry 5, 7 (2001).

[8] Zhao, R., Li, Q., Wang, C. & Yin, L. Highly ordered mesoporous spinel $ZnCo_2O_4$ as a high-performance anode material for lithium-ion batteries. Electrochimica Acta 197, 58-67, doi:10.1016/j.electacta.2016.03.047 (2016).

[9] Cabana, J. et al. Enhanced high rate performance of $LiMn_2O_4$ spinel nanoparticles synthesized by a hard-template route. Journal of Power Sources 166, 492-498, doi:10.1016/j.jpowsour.2006.12.107 (2007).

[10] Myung, S.-T., and Hoon-Taek Chung. Preparation and characterization of $LiMn_2O_4$ powders by the emulsion drying method. Journal of Power Sources 84 (1999).

[11] Song, M. Y., Dong Su Ahn, and Hye Ryoung Park. Capacity fading of spinel phase $LiMn_2O_4$ with cycling. Journal of Power Sources, 83 (1999).

[12] Park, S. B., Shin, H. C., Lee, W.-G., Cho, W. I. & Jang, H. Improvement of capacity fading resistance of $LiMn_2O_4$ by amphoteric oxides. Journal of Power Sources 180, 597-601, doi:10.1016/j.jpowsour.2008.01.051 (2008).

[13] Chung, K. Y., Lee, H. S., Yoon, W.-S., McBreen, J. & Yang, X.-Q. Studies of $LiMn_2O_4$ Capacity Fading at Elevated Temperature Using In Situ Synchrotron X-Ray Diffraction. Journal of The Electrochemical Society 153, A774, doi:10.1149/1.2172565 (2006).

[14] Choi, H. J., Ki‐Min Lee, Gyeung‐Ho Kim, and June‐Gunn Lee. Mechanochemical synthesis and electrochemical properties of $LiMn_2O_4$. Journal of the American Ceramic Society 84 (2001).

[15] Xia, Y., Yunhong Zhou, and Masaki Yoshio. Capacity fading on cycling of 4 V Li/LiMn2 O 4 Cells. Journal of The Electrochemical Society 144 (1997).

[16] Lee, Y. K. Effects of Transition Metal Dissolution and Deposition on LI-Ion Batteries: A Multi-Scale Approach. (2015).

[17] Kim, Y., Lim, J. & Kang, S. Investigation on the dissolution of Mn ions from LiMn2O4cathode in the application of lithium ion batteries: First principle molecular orbital method. International Journal of Quantum Chemistry 113, 148-154, doi:10.1002/qua.24314 (2013).

[18] Xia, H., Luo, Z. & Xie, J. Nanostructured $LiMn_2O_4$ and their composites as high-performance cathodes for lithium-ion batteries. Progress in Natural Science: Materials International 22, 572-584, doi:10.1016/j.pnsc.2012.11.014 (2012).

[19] Zheng, H. et al. Barrier Modification of Metal-contact on Silicon by Sub-2 nm Platinum Nanoparticles and Thin Dielectrics. Sci Rep 6, 25234, doi: 10.1038/srep25234 (2016).

[20] Li, Q.-L., Xu, W.-Q., Bai, H.-L., Guo, J.-M. & Su, C.-W. ZnO-coated $LiMn_2O_4$ cathode material for lithium-ion batteries synthesized by a combustion method. Ionics 22, 1343-1351, doi: 10.1007/s11581-016-1655-8 (2016).

[21] Zhao, J., Qu, G., Flake, J. C. & Wang, Y. Low temperature preparation of crystalline ZrO_2 coatings for improved elevated-temperature performances of Li-ion battery cathodes. Chem Commun (Camb) 48, 8108-8110, doi: 10.1039/c2cc33522k (2012).

[22] Yu, L., Qiu, X., Xi, J., Zhu, W. & Chen, L. Enhanced high-potential and elevated-temperature cycling stability of $LiMn_2O_4$ cathode by TiO_2 modification for Li-ion battery. Electrochimica Acta 51, 6406-6411, doi:10.1016/j.electacta.2006.04.054 (2006).

[23] Li, C. et al. Cathode materials modified by surface coating for lithium ion batteries. Electrochimica Acta 51, 3872-3883, doi:10.1016/j.electacta.2005.11.015 (2006).

[24] Guan, D., Chuan Cai, and Ying Wang. Enhanced Cycleability of $LiMn_2O_4$ Cathodes by Atomic Layer Deposition of Al_2O_3 Coatings. In Green Technologies Conference (2011).

[25] Patel, R. L. et al. Significant Capacity and Cycle-Life Improvement of Lithium-Ion Batteries through Ultrathin Conductive Film Stabilized Cathode Particles. Advanced Materials Interfaces 2, 1500046, doi:10.1002/admi.201500046 (2015).

[26] Sarkar, S., Patel, R. L., Liang, X. & Park, J. Unveiling the Role of CeO_2 Atomic Layer Deposition Coatings on $LiMn_2O_4$ Cathode Materials: An Experimental and Theoretical Study. ACS Appl Mater Interfaces 9, 30599-30607, doi:10.1021/acsami.7b06988 (2017).

[27] Cho, M.-Y., Roh, K.-C., Park, S.-M. & Lee, J.-W. Effects of CeO_2 coating uniformity on high temperature cycle life performance of $LiMn_2O_4$. Materials Letters 65, 2011-2014, doi:10.1016/j.matlet.2011.03.100 (2011).

[28] Ha, H.-W., Nan Ji Yun, and Keon Kim. Improvement of electrochemical stability of $LiMn_2O_4$ by CeO_2 coating for lithium-ion batteries. Electrochimica Acta 52, doi:10.1016/j.electacta.2006.09.066 (2007).

[29] Arumugam, D. & Kalaignan, G. P. Synthesis and electrochemical characterization of nano-CeO_2-coated nanostructure $LiMn_2O_4$ cathode materials for rechargeable lithium batteries. Electrochimica Acta 55, 8709-8716, doi:10.1016/j.electacta.2010.08.016 (2010).

[30] Yuan, W., Zhang, H. Z., Liu, Q., Li, G. R. & Gao, X. P. Surface modification of $Li(Li_{0.17}Ni_{0.2}Co_{0.05}Mn_{0.58})O_2$ with CeO_2 as cathode material for Li-ion batteries. Electrochimica Acta 135, 199-207, doi:10.1016/j.electacta.2014.04.181 (2014).

[31] Michalska, M. et al. Influence of $LiMn_2O_4$ modification with CeO_2 on electrode performance. Electrochimica Acta 136, 286-291, doi:10.1016/j.electacta.2014.05.108 (2014).

[32] Wang, J. et al. Al_2O_3 Coated Concentration-Gradient $Li[Ni_{0.73}Co_{0.12}Mn_{0.15}]O_2$ Cathode Material by Freeze Drying for Long-Life Lithium Ion Batteries. Electrochimica Acta 174, 1185-1191, doi:10.1016/j.electacta.2015.06.112 (2015).

[33] Qiu, Q., Huang, X., Chen, Y., Tan, Y. & Lv, W. Al_2O_3 coated $LiNi_{1/3}Co_{1/3}Mn_{1/3}O_2$ cathode material by sol–gel method: Preparation and characterization. Ceramics International 40, 10511-10516, doi:10.1016/j.ceramint.2014.03.023 (2014).

[34] Liu, K., Yang, G.-L., Dong, Y., Shi, T. & Chen, L. Enhanced cycling stability and rate performance of Li[Ni $_{0.5}$C $_{0.2}$Mn$_{0.3}$]O_2 by CeO_2 coating at high cut-off voltage. Journal of Power Sources 281, 370-377, doi:10.1016/j.jpowsour.2014.12.131 (2015).

[35] Wise, A. M. et al. Effect of Al_2O_3 Coating on Stabilizing $LiNi_{0.4}Mn_{0.4}Co_{0.2}O_2$ Cathodes. Chemistry of Materials 27, 6146-6154, doi:10.1021/acs.chemmater.5b02952 (2015).

[36] Yan, P. et al. Atomic to Nanoscale Investigation of Functionalities of an Al_2O_3 Coating Layer on a Cathode for Enhanced Battery Performance. Chemistry of Materials 28, 857-863, doi:10.1021/acs.chemmater.5b04301 (2016).

[37] Su, Y. et al. Enhancing the High-Voltage Cycling Performance of LiNi(0.5)Mn(0.3)Co(0.2)O2 by Retarding Its Interfacial Reaction with an Electrolyte by Atomic-Layer-Deposited Al_2O_3. ACS Appl Mater Interfaces 7, 25105-25112, doi:10.1021/acsami.5b05500 (2015).

[38] Jung, Y. S., Andrew S. Cavanagh, Yanfa Yan, Steven M. George, and Arumugam Manthiram. Effects of atomic layer deposition of Al_2O_3 on the Li [$Li_{0.20}Mn_{0.54}Ni_{0.13}Co_{0.13}$] O_2 cathode for lithium-ion batteries. Journal of the Electrochemical Society 158, doi:10.1149/2.030112jes] (2011).

[39] Wang, M., Wu, F., Su, Y. & Chen, S. Modification of $LiCo_{1/3}Ni_{1/3}Mn_{1/3}O_2$ cathode material by CeO_2-coating. Science in China Series E: Technological Sciences 52, 2737-2741, doi: 10.1007/s11431-008-0306-3 (2008).

[40] Zhang, X. et al. Structural and Electrochemical Study of Al_2O_3 and TiO_2 Coated $Li_{1.2}Ni_{0.13}Mn_{0.54}Co_{0.13}O_2$ Cathode Material Using ALD. Advanced Energy Materials 3, 1299-1307, doi:10.1002/aenm.201300269 (2013).

[41] Wu, F., Wang, M., Su, Y., Bao, L. & Chen, S. Surface of $LiCo_{1/3}Ni_{1/3}Mn_{1/3}O_2$ modified by CeO_2-coating. Electrochimica Acta 54, 6803-6807, doi:10.1016/j.electacta.2009.06.075 (2009).

[42] Li, X. et al. Significant impact on cathode performance of lithium-ion batteries by precisely controlled metal oxide nanocoatings via atomic layer deposition. Journal of Power Sources 247, 57-69, doi:10.1016/j.jpowsour.2013.08.042 (2014).

[43] Kim, J. W. et al. Surface chemistry of $LiNi_{0.5}Mn_{1.5}O_4$ particles coated by Al_2O_3 using atomic layer deposition for lithium-ion batteries. Journal of Power Sources 274, 1254-1262, doi:10.1016/j.jpowsour.2014.10.207 (2015).

[44] Ha, H.-W., Yun, N. J., Kim, M. H., Woo, M. H. & Kim, K. Enhanced electrochemical and thermal stability of surface-modified $LiCoO_2$ cathode by CeO_2 coating. Electrochimica Acta 51, 3297-3302, doi:10.1016/j.electacta.2005.09.023 (2006).

[45] Chen, Z., Qin, Y., Amine, K. & Sun, Y. K. Role of surface coating on cathode materials for lithium-ion batteries. Journal of Materials Chemistry 20, 7606, doi: 10.1039/c0jm00154f (2010).

[46] Lee, Y. K., Jonghyun Park, and Wei Lu. Electronic and Bonding Properties of $LiMn_2O_4$ Spinel with Different Surface Orientations and Doping Elements and Their Effects on Manganese Dissolution. Journal of The Electrochemical Society 163, doi:10.1149/2.0991607jes] (2016).

[47] Leung, K. First-Principles Modeling of Mn (II) Migration above and Dissolution from $Li_xMn_2O_4$ (001) Surfaces. Chemistry of Materials 29, 2550-2562, doi:10.1021/acs.chemmater.6b04429 (2016).

[48] Kim, W.-K., Dong-Wook Han, Won-Hee Ryu, Sung-Jin Lim, and Hyuk-Sang Kwon. Al_2O_3 coating on $LiMn_2O_4$ by electrostatic attraction forces and its effects on the high temperature cyclic performance. Electrochimica Acta 71, doi:10.1016/j.electacta.2012.03.090 (2012).

[49] Ouyang, C. Y., X. M. Zeng, Z. Sljivancanin, and A. Baldereschi. Oxidation states of Mn atoms at clean and Al2O3-covered $LiMn_2O_4$ (001) surfaces. The Journal of Physical Chemistry C 114 (2010).

[50] Tarascon, J. M., E. Wang, F. K. Shokoohi, W. R. McKinnon, and S. Colson. The spinel phase of $LiMn_2O_4$ as a cathode in secondary lithium cells. Journal of the Electrochemical Society 138 (1991).

[51] Jang, D. H., and Seung M. Oh. Electrolyte Effects on Spinel Dissolution and Cathodic Capacity Losses in 4 V $Li/Li_xMn_2O_4$ Rechargeable Cells. Journal of The Electrochemical Society 144 (1997).

[52] Jang, D. H., Young J. Shin, and Seung M. Oh. Dissolution of spinel oxides and capacity losses in 4 V $li/li_xMn_2O_4$ cells. Journal of The Electrochemical Society 143 (1996).

[53] Kang, J. & Han, B. First-Principles Study on the Thermal Stability of $LiNiO_2$ Materials Coated by Amorphous Al_2O_3 with Atomic Layer Thickness. ACS Appl Mater Interfaces 7, 11599-11603, doi:10.1021/acsami.5b02572 (2015).

[54] Hasegawa, A., Kazunari Yoshizawa, and Tokio Yamabe. Crystal Orbital Overlap Population Analysis of the Capacity Fading of Metal‐Substituted Spinel Lithium Manganate $LiMn_2O_4$. Journal of the Electrochemical Society 147 (2000).

[55] Lin, X., Jonghyun Park, Lin Liu, Yoonkoo Lee, A. M. Sastry, and Wei Lu. A comprehensive capacity fade model and analysis for Li-ion batteries. Journal of The Electrochemical Society 160, doi:10.1149/2.040310jes] (2013).

[56] Hoivik, N. D., Jeffrey W. Elam, Ryan J. Linderman, Victor M. Bright, Steven M. George, and Y. C. Lee. Atomic layer deposited protective coatings for micro-electromechanical systems. Sensors and Actuators A: Physical 103 (2003).

[57] Johnson, R. W., Hultqvist, A. & Bent, S. F. A brief review of atomic layer deposition: from fundamentals to applications. Materials Today 17, 236-246, doi:10.1016/j.mattod.2014.04.026 (2014).

[58] Wank, J. R., Steven M. George, and Alan W. Weimer. . Coating fine nickel particles with Al_2O_3 utilizing an atomic layer deposition ‐ fluidized bed reactor (ALD ‐ FBR). Journal of the American Ceramic Society 87 (2004).

[59] Liang, X. et al. Novel Processing to Produce Polymer/Ceramic Nanocomposites by Atomic Layer Deposition. Journal of the American Ceramic Society 90, 57-63, doi:10.1111/j.1551-2916.2006.01359.x (2007).

[60] Bazilio, A., and J. Weinrich. The Easy Guide to: Inductively Coupled Plasma-Mass Spectrometry (ICP-MS). (2012).

[61] Warra, A. A., and W. L. O. Jimoh. OVERVIEW OF AN INDUCTIVELY COUPLED PLASMA (ICP) SYSTEM. International Journal of Chemical Research 3 (2011).

[62] Kresse, G., & Furthmüller, J. Efficient iterative schemes for ab initio total-energy calculations using a plane-wave basis set. Physical review B 54 (1996).

[63] Perdew, J. P., Burke, K. Generalized gradient approximation made simple. Physical review letters 77 (1996).

[64] Tompsett, D. A., Parker, S. C. & Islam, M. S. Rutile (beta-)MnO_2 surfaces and vacancy formation for high electrochemical and catalytic performance. J Am Chem Soc 136, 1418-1426, doi: 10.1021/ja4092962 (2014).

[65] Dawson, J. A., Chen, H. & Tanaka, I. First-principles calculations of oxygen vacancy formation and metallic behavior at a beta-MnO_2 grain boundary. ACS Appl Mater Interfaces 7, 1726-1734, doi: 10.1021/am507273c (2015).

[66] Hoang, K. Understanding the electronic and ionic conduction and lithium over-stoichiometry in $LiMn_2O_4$ spinel. J. Mater. Chem. A 2, 18271-18280, doi: 10.1039/c4ta04116j (2014).

III. FIRST-PRINCIPLES STUDY OF ATOMIC LAYER DEPOSITED FILM COATING THICKNESS IMPACT ON LITHIUM ION DIFFUSIVITY

ABSTRACT

Li ion diffusivity is one of the most crucial factors that determine Lithium-ion Battery (LIB) performance. Ultrathin film coating prepared via Atomic Layer Deposition (ALD) technology have been extensively employed as an engineering layer that can enhance the Li ion diffusivity of active particles. Several investigations have experimentally observed that the thickness of the ALD coating influences the effective diffusion of coated particles and that there exists an optimal thickness for the highest diffusivity. Despite these examinations, there is no clear mechanism that explains these experimental observations and the relationship between coating thickness and Li ion diffusivity. In this work, an investigation is conducted to elucidate the role of the ALD coating thickness on Li ion diffusivity in CeO2 coated cathode particles via first-principles calculations. The simulation results demonstrated that a combination of surface/bulk diffusion and structural change determines the overall diffusivity in the coated particles. The bulk diffusion becomes important as the thickness increases leading to a decrease in diffusivity, while the preferred amorphous structure at higher thickness enhances the diffusivity compared to the crystal structure. An increase of diffusivity of the coating material near the bulk surface is observed and identified to be caused by the interaction with the bulk material where surface orientation and termination are important factors. Further, it is demonstrated that the revealed mechanism can be utilized to enhance the effective diffusivity by forming a thin amorphous coating layer. This is the first report elucidating how the coating thickness affects the overall diffusivity of coated

particles, which gives an insight into efficient utilization of ALD coatings to improve LIB performance.

1. INTRODUCTION

Lithium-Ion Batteries (LIBs) have attracted great attention as an advanced secondary energy storage media due to its high energy efficiency, long cycle life, and portability. However, current LIBs cannot keep pace with the growing requirements for sustainable energy storage systems, especially in portable devices, transportation, and large energy storage. The increasing demands for LIBs have accelerated the development of advanced active materials to serve as cathodes, where an ideal cathode material should possess high reversible storage capacity for Li ion transportation. However, a crucial issue of cathode materials is material degradation that ultimately leads to poor performance and eventual battery failure. For example, the Mn-based LIBs cathodes such as $LiMn_2O_4$ (LMO), $LiMn_{1.5}Ni_{0.5}O_4$ (LMNO), and $LiNiMnCoO_2$ (NMC) suffer from chemical and electrochemical degradations during cycling, causing structural and chemical changes that impede Li ion diffusivity.[1-4] There are several strategies to improve Li diffusivity, some of which focus on improvement at the structural level including designing new cathode material structure[5-6] and modifying cathode material micro-structure during electrode fabrication.[7] Another effective approach to improve Li ion diffusivity is through coating with ALD film on the cathode material surface.[8-10]

The ALD coating technology has been employed as an effective surface coating method to improve active material performance via deposition of an ultrathin film on the particle surface. Through self-limiting surface reactions, the ALD process can deposit

coating thicknesses at the nanoscale level.[9, 11-13] The ALD film coating plays an important role in improving the capacity retention, thermal stability, rate capability and Li ion conductivity of electrode materials. Several ALD coating materials have been studied. It was demonstrated that 3 nm CeO_2 coated LMO showed the best capacity and cycling performance over uncoated, Al_2O_3 coated and ZrO_2 coated samples at room temperature and 55 °C, which is attributed to the suppression of the impedance increase and the facile transport of Li ions.[8] The conformal layer of Al_2O_3 helped to prevent $LiNi_{1/3}Mn_{1/3}Co_{1/3}O_2$ particles from dissolution and the electrochemical performance was significantly improved[14] and contributed to the best cycling stability of $LiCoO_2$[15], LMO and $LiLi_{0.2}Mn_{0.54}Ni_{0.13}Co_{0.13}O_2$ cathodes.[16-17] The TiO_2 nanotubes with uniform wall thickness have demonstrated excellent rate capability and cycling response.[18] The 8 layers of ALD deposited ZnO demonstrated greatly improved discharge capacity and cycling response compared with uncoated $LiNi_{0.5}Co_{0.2}Mn_{0.3}O_2$.[19] ZrO_2 ALD modified $LiMn_2O_4$ nanoparticles showed greatly improved specific capacity and cycleability at 55 °C.[20] The 5.8 nm ALD-TiN coated LTO nanoparticle anode showed a remarkably improved performance.[21] The ALD deposited TiN coating was found to limit growth of the Solid Electrolyte Interphase (SEI) layer, which improved the performance of any nanostructured LIB electrode that suffers from SEI layer formation.[22] The ALD Al_2O_3 coating demonstrated significantly enhanced columbic efficiency and capacity retention.[23-24] The $LiAlO_2$ showed improved electrochemical stability of $LiNi_{0.5}Mn_{1.5}O_4$/graphite LIBs.[25]

A critical aspect of this technology is that the enhancement and performance of ALD coating layers is closely related to the thickness of the deposited layer.

Experimentally, it has been demonstrated that varying the thickness of the coating layer also changes the performance behavior of the coating, and that for a particular material there is an optimal coating thickness that yields the best effects. For example, the 1-2 nm ALD carbon coated $LiFePO_4$/C composite improved the reversible capacity that delivered about 80% of the theoretical capacity with a current density of 170mA/g.[26] Furthermore, a ZnO ALD coating was shown to improve the cycling performance of $LiMn_2O_4$ (LMO) particles significantly among different ALD coating thicknesses, where a 1.02 nm layer thickness showed the best results.[27] The 2 cycle (~3-4 Å thick) ALD Al_2O_3 coated cathode particles exhibited better electrochemical performance than 6 cycles and 10 cycles (~2 nm) due to the restricted electron transport and slower Li ion diffusion in the ALD Al_2O_3 layer when the thickness increases.[14, 28-29] In particular, the previous work experimentally observed that the Li ion diffusivity varies with differing CeO_2 coating thickness but the mechanism behind this observation was unclear. Despite the numerous demonstrations that indicate a strong correlation between ALD coating thickness and Li diffusivity through active particles, there has yet to be a clear understanding that reveals the fundamental reason why a certain thickness in an ALD coating material is better than others.

Therefore, in this work, we focused on understanding the fundamental mechanism of ALD CeO_2 coating impact on Li ion diffusivity, in terms of coating thickness and structural changes, via performing the first-principles calculation. The fundamental hypothesis for this study is that the phase transition of ALD coating and the thickness-dependent surface diffusion and bulk diffusion determine the effective diffusivity of ALD coated particles. First, the diffusion barrier for Li diffusion on the LMO surface, LMO

bulk, CeO_2 surface, and CeO_2 bulk was examined by the climbing-image nudged elastic band (CINEB) method. Furthermore, it has been observed that when ALD coating thickness increases, the coating structure undergoes a phase transition, which was similar to an observation in which the ALD Al_2O_3 process showed a phase transition from the corundum-type crystalline (c-Al_2O_3) to amorphous (aAl_2O_3) structures as the coating thickness reaches 0.88nm.[30] Thus, to determine the phase transition impact on Li ion diffusivity, the diffusion barrier between crystal CeO2 coated and amorphous CeO2 coated LMO were compared via CINEB. Lastly, the ALD coating thickness impact on Li diffusivity was investigated by inspecting the Li ion diffusivity in amorphous and crystal CeO_2 coated LMO at different thicknesses via performing Ab initio MD simulation. This work reveals the fundamental relationship between ALD coating thickness, structural property, and Li ion diffusivity, providing deeper insight into efficient implementation of ALD coating to substantially improve LIB performance.

2. COMPUTATIONAL DETAILS

2.1. THEORETICAL CALCULATIONS

First-principles calculations were performed based on the Density Functional Theory (DFT) using Vienna Ab initio Simulation Package (VASP).[31] Projector-augmented wave method [32] was used to approximate electron and core interaction, where the valence electrons are expanded in a plane wave basis set. The Perdew–Burke–Ernzerhof (PBE) functional was used to approximate the exchange and correlation functional. A 1 × 1 × 1 of Gamma-centered grid was used and all calculations were ensured with a total system energy convergence. The cutoff energy of 600 eV and 400 eV

was applied to represent the electronic wave functions of valence electrons for LMO system and CeO_2 system, respectively. The convergence criterion of the energy in the structure optimization was set to 10^{-4} eV.

2.2. CLIMBING-IMAGE NUDGED ELASTIC BAND (CINEB) METHOD

Climbing-image Nudged Elastic Band (CINEB) method [33-36] was used to determine the diffusion barrier for Li diffusion on LMO surface, LMO bulk, CeO_2 surface and CeO_2 bulk. The LMO structure consisted of 1Li, 16Mn and 32O. The CeO_2 bulk and surface constant contained 1Li, 32 Ce and 64O. In addition, to understand the phase transition impact on Li diffusivity, the crystal CeO_2 coated LMO and amorphous CeO_2 coated LMO were compared using CINEB method. Li terminated 001_LMO structure was used during NEB calculation. One amorphous CeO_2 layer includes 7Ce and 14O while one crystal CeO_2 layer includes 8Ce and 16O. The crystal CeO_2 coated LMO contains 23Li, 32Mn, 80O and 8Ce. The amorphous CeO_2 coated LMO includes 27Li, 32Mn, 78O and 7Ce. The Li ion diffusivity in LMO and CeO_2 were estimated according to the Arrhenius law[37]:

$$D = a^2 v \exp(-E_D/k_B T) \quad (1)$$

where a is the hop distance; v is the phonon frequency v=10^{13} Hz; ED is barrier energy; k_B is Boltzmann constant and T is temperature.

2.3. LI ION DIFFUSIVITY IN ALD COATED LMO

To investigate ALD coating thickness impact on Li ion diffusivity in ALD coated LMO, the Li ion diffusivity in amorphous and crystal CeO_2 coated LMO were inspected.

The crystal CeO_2 coating ranged from 0.55 nm to 3.19 nm. The amorphous CeO_2 coating ranged from 0.79 nm to 4.39 nm. The one amorphous coating layer was prepared by quenching process. The initial random structure was heated from 300 K to 3000 K, then the structure was equilibrated for 1 ps at 3000 K, and finally, the structure was cooled from 3000 K to 300 K. The prepared amorphous structure was put on top of the Li terminated 001 orientated LMO. The Ab initio MD simulation was performed at 300 K to obtain the mean square displacement. The Li ion diffusivity was obtained at 300 K based on the Einstein relation, which is described as follows:

$$r^2(t) = 6Dt \tag{2}$$

where r^2 is mean square displacement; D is Li ion diffusivity; t is diffusion time.

3. RESULTS AND DISCUSSION

3.1. LI ION DIFFUSIVITY IN LMO

Li ion diffusivity in uncoated LMO was inspected first, which will be used to compare with coated particles. Figure 1 shows the initial and final configuration of LMO for CINEB calculation, in which the Li ions were positioned on the 8a tetrahedral site and manganese ions were located on the 16d sites. The CINEB predicted the minimum energy pathway for Li ion migration from the 8a tetrahedral site to its nearest tetrahedral site. The barrier energy of the diffusion pathway was calculated for Li diffusion in LMO bulk and LMO surface respectively. Figure 1 shows that a Li ion must overcome 0.46 eV barrier energy on the diffusion pathway. The Li ion diffusivity in bulk was $2.40e^{-10}$ cm^2/s based on Arrhenius law, which is in the range of the reported value[38]. To calculate the Li diffusion on LMO surface, a LMO slab structure with two Li ions terminated 001 plane

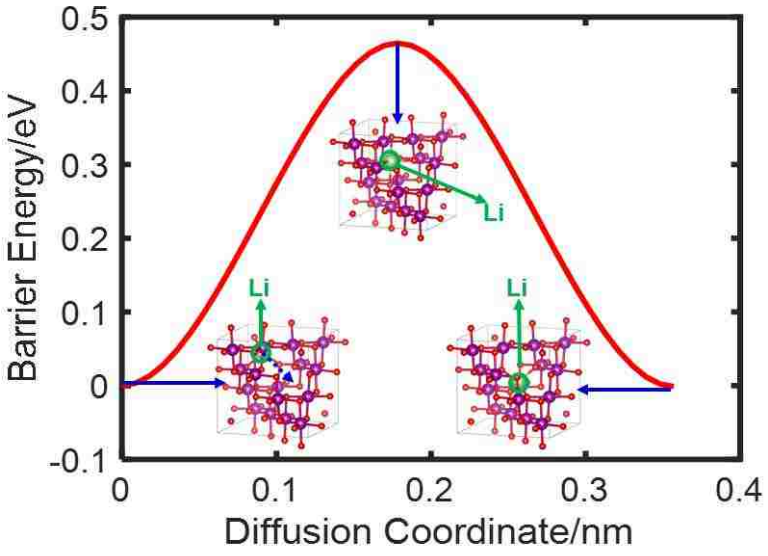

Figure 1. The barrier energy of Li diffusion in LMO bulk using CINEB calculations.

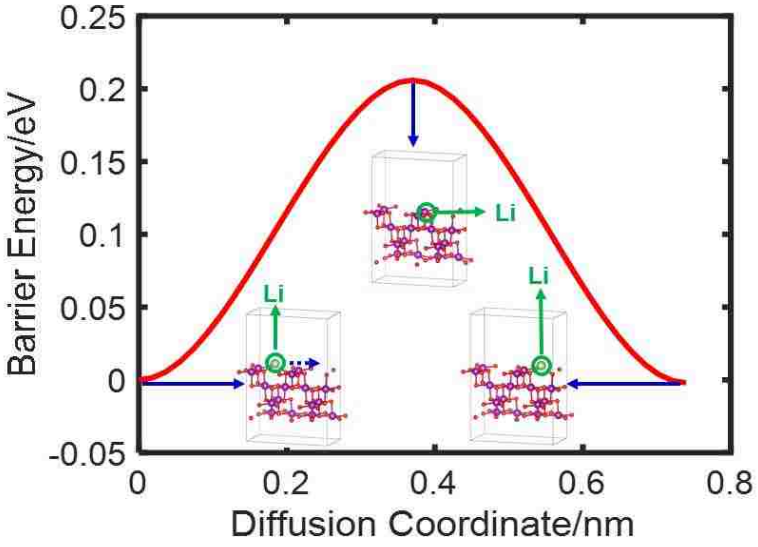

Figure 2. The barrier energy of Li diffusion on LMO surface using CINEB calculations.

was created where Li ion diffuses from one tetrahedral site to the other tetrahedral site on LMO surface. Figure 2 shows the initial and final configurations of Li diffusion on LMO surface. Based on CINEB calculation, as shown in Fig. 2, the barrier energy was determined as 0.21 eV. Thus, the corresponding Li ion diffusivity was $1.63e^{-05}$ cm^2/s, which is about five orders of magnitude higher than Li diffusion in bulk LMO. This comparison of Li ion diffusivity in bulk LMO and LMO surface indicated that Li ions can more easily transfer on the surface than in the bulk due to the surface's lower diffusion barrier energy.

3.2. LI ION DIFFUSIVITY IN CRYSTAL CEO_2 COATING

Then, Li ion diffusivity in CeO_2 coating was investigated to understand the CeO_2 coating thickness impact on Li ion diffusivity by comparing Li ion diffusivity in CeO_2 coating and LMO active material. The barrier energy of Li ion diffusion in CeO_2 bulk and surface were calculated via the same CINEB method. The initial and final configurations of CeO_2 bulk that were used for CINEB calculation are shown in Fig. 3, which indicated the barrier energy of Li ion diffusion in crystal CeO_2 bulk was 0.457 eV. Then according to Arrhenius law, the calculated Li ion diffusivity in CeO_2 bulk was 2.26e-09 cm^2/s. Figure 4 displays the Li ion initial site and final site on CeO_2 coating surface. There was 0.42 eV barrier energy for Li ion to overcome when diffusing on CeO_2 surface and the corresponding Li ion diffusion on CeO_2 surface was 1.79e-08 cm^2/s. Similar to LMO, Li ion diffuses faster on CeO_2 surface than in CeO_2 bulk due to the lower barrier energy. The Li ion diffusivity in amorphous CeO_2 was calculated via ab initio MD simulation from our previous work.[40] The mean square displacement of Li ion was obtained from ab

initio MD simulation. The Li ion diffusivity in amorphous CeO_2 bulk was calculated as 1.74e-08 cm^2/s based on the Einstein relation.

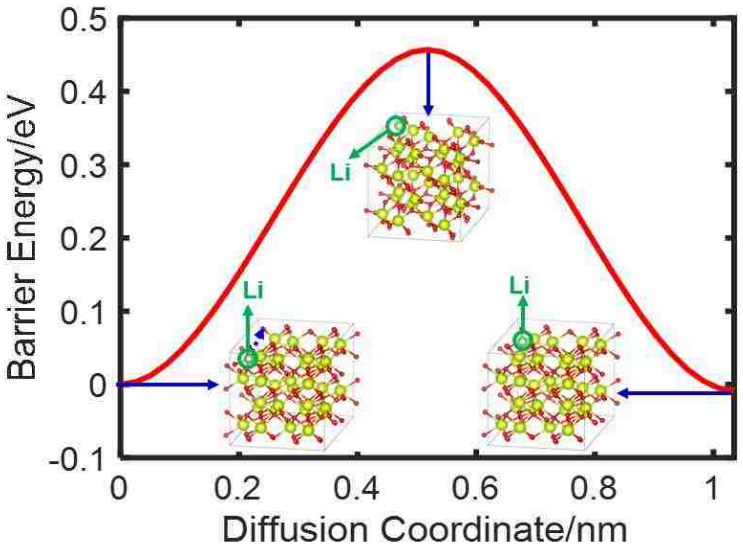

Figure 3. The barrier energy of Li diffusion on CeO_2 bulk using CINEB calculations.

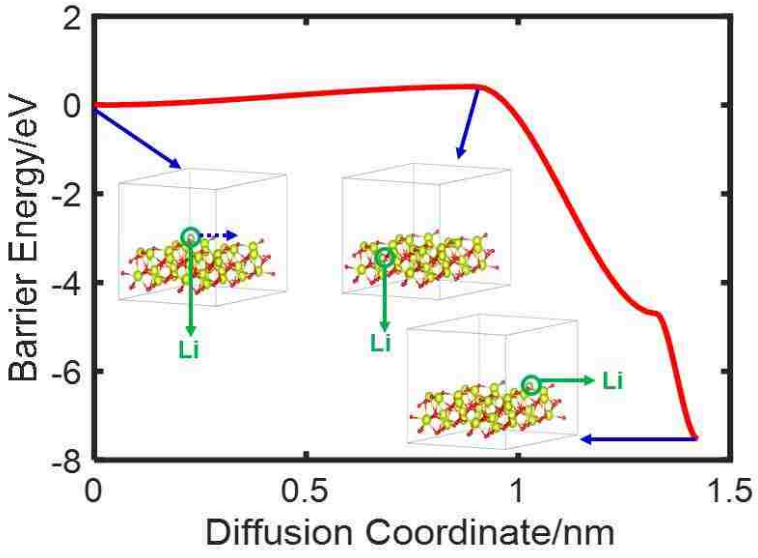

Figure 4. The barrier energy of Li diffusion on CeO_2 surface using CINEB calculations.

3.3. LI ION DIFFUSIVITY IN DIFFERENT STRUCTURE COATED LMO PARTICLES

It has been previously reported that different coating structures can be formed by varying the coating thickness, which may impact Li ion diffusivity of the coating layer.[30] To understand the ALD CeO_2 coating thickness impact on Li ion diffusivity in different structure coated LMO particles, the Li ion diffusivity in crystal CeO_2 coated LMO and amorphous CeO_2 coated LMO with different ALD coating thickness were compared. As shown in Fig. 5, the amorphous CeO_2 coating thickness ranged from 0.79 nm to 4.39 nm and the crystal CeO2 coating thickness ranged from 0.55 nm to 3.19 nm, both of which were inspected via performing ab initio MD simulation. As shown in Fig. 6, it was observed that the Li ion diffusivity when amorphous CeO_2 coating thickness increased from 0.79 nm to 3.49 nm. When coating thickness was further increased, the Li diffusivity remained at a relatively constant value. Similarly, the Li ion diffusivity decreased when crystal coating thickness increased from 0.55 nm to 2.53 nm and after the coating thickness increased further, the Li ion diffusivity reached stability.

It was observed that as the coating thickness increases, the coating layer preferred to form an amorphous structure, and that a crystal structure was more preferentially formed with ultrathin layers. Therefore, when coating thickness increases, the Li ion diffusivity can also increase due to the preferred formation of the higher diffusivity amorphous structure. To further confirm the phase transition of coating thickness impact on Li ion diffusivity, the total energy of relaxed five crystal CeO_2 layer coated LMO (56Li, 32Mn, 144O and 40Ce), three amorphous CeO_2 coated LMO (56Li, 32Mn, 106O and 21Ce) and four amorphous CeO_2 layer coated LMO (70Li, 32Mn, 120O and 28Ce) were inspected. As shown in Table 1, the amorphous CeO_2 layer coated LMO had a

lower energy than crystal CeO2 layer coated LMO, suggesting that the crystal CeO_2 layer tended to transform into an amorphous CeO2 coating structure at increased layer thickness. As the coating thickness increased, the Li ion diffusivity in amorphous CeO_2 coated LMO was higher than Li ion diffusivity in crystal CeO_2 coated LMO. It was then revealed that the thinnest CeO_2 coating had the highest Li ion diffusivity, which can be explained by the dominant lower energy barrier surface diffusion while the coating thickness was very thin. On the other hand, with a coating thickness increase, the low bulk diffusion and high energy barrier caused the decrease of Li ion diffusivity. These

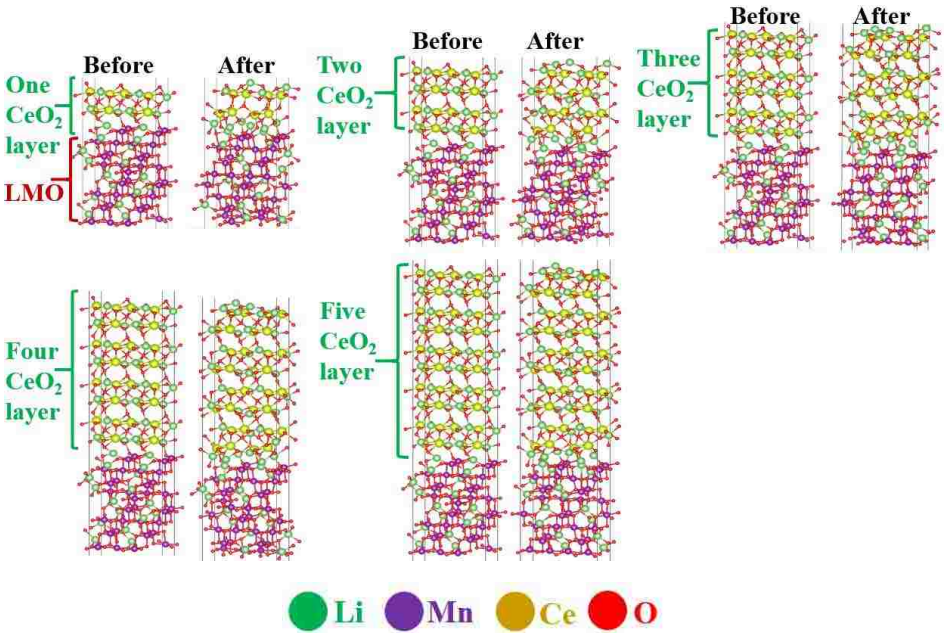

(A)

Figure 5. (A) Initial and final relaxed crystal structures by changing the number of layers from one to five, (B) initial and final relaxed amorphous structures by changing the number of layers from one to five.

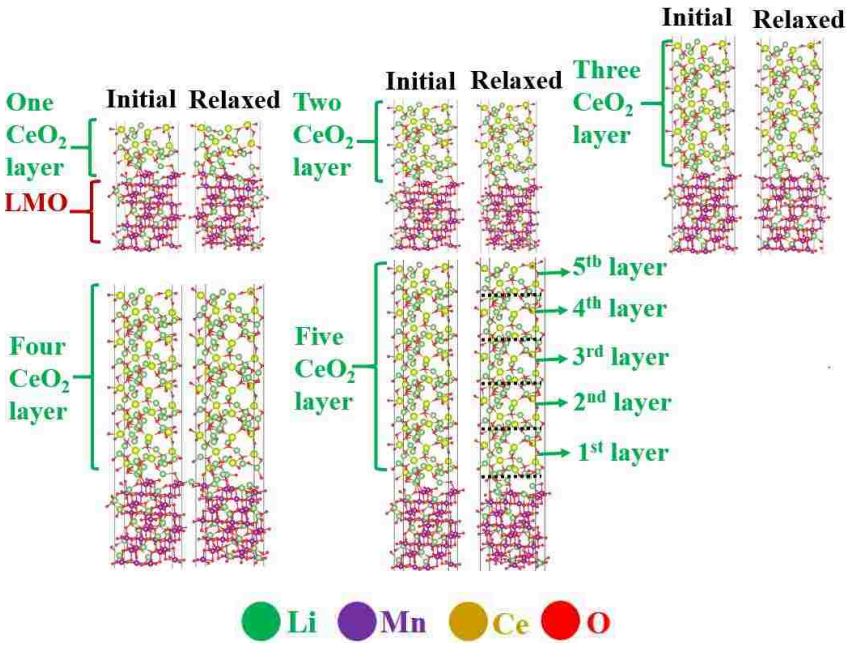

(B)

Figure 5. (A) Initial and final relaxed crystal structures by changing the number of layers from one to five, (B) initial and final relaxed amorphous structures by changing the number of layers from one to five (cont.).

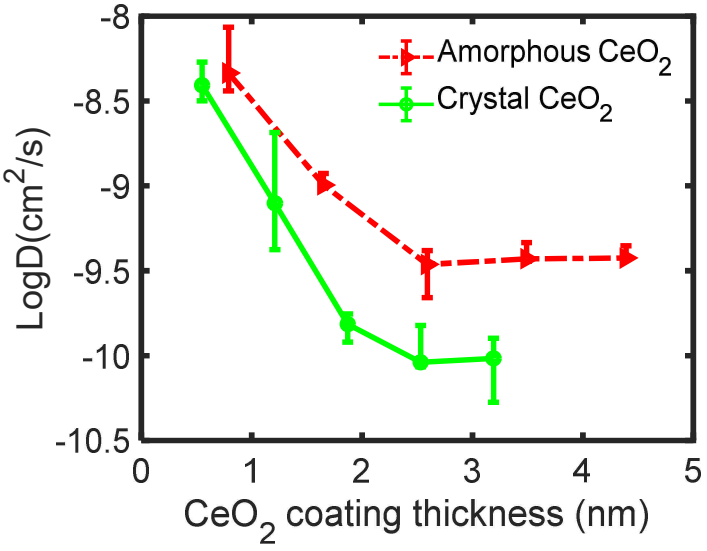

Figure 6. Li diffusivity of LMO coated with crystal CeO_2 and amorphous CeO_2.

combined phenomena could explain the experimental observation that the Li ion diffusivity increased first as the coating thickness increased, then it decreased as the thickness increased further after reaching the maximum diffusivity.

Table 1. The total energy of crystal and amorphous CeO_2 layer coated LMO.

Structure	Energy (eV)
3.19 nm crystal CeO_2 layer coated LMO	-1908.37
2.59 nm amorphous CeO_2 layer coated LMO	-1939.50
3.49 nm amorphous CeO_2 layer coated LMO	-2284.22

3.4. PHASE TRANSITION IMPACT ON LI ION DIFFUSIVITY

To explain the higher Li ion diffusivity in amorphous CeO_2 coating compared to crystal CeO_2, the phase transition impact on the Li diffusivity was investigated by calculating the mean square displacement of Li in different crystal CeO_2 coating layer. As shown in Fig. 5C, five amorphous CeO_2 coating layers were added on the top of LMO. As shown in Figure 7A, the mean square displacement of Li in the first and fifth layer was higher than second, third and fourth layer. Then, the Li ion diffusivity was calculated according to Einstein relation. As shown in Fig. 7B, the Li ion diffusivity in the first and fifth layer yielded a higher Li ion diffusivity compared to that in the second, third, and fourth layer from the ab initio molecular dynamic (MD) simulation. The high Li ion diffusivity in fifth layer can be explained by the higher surface diffusion compared to that of bulk diffusion. Furthermore, the Li ion diffusivity in the first layer was higher than the

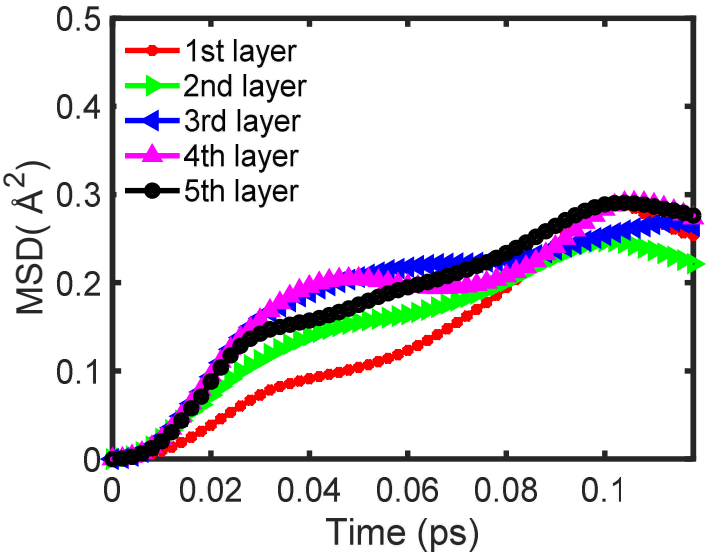

(A)

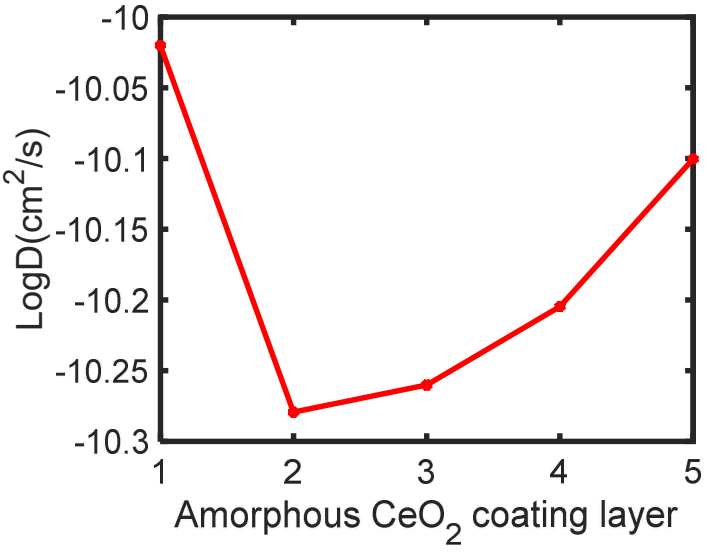

(B)

Figure 7. Mean square displacement (A) and diffusion coefficient (B) of Li in the first, the second, the third, the fourth and the fifth amorphous CeO_2 layer coated LMO after relaxation.

second, third and fourth layer because the LMO structure was Li terminated 001 surface orientation slab structure, creating a gap between LMO and CeO_2 coatings that provided the opportune chance for Li ion diffusion on surface thus contributing to high Li ion diffusivity.

4. DISCUSSION

From our results, it was found that the Li ion diffusivity in the first layer of the five amorphous CeO2 layer coated LMO was higher than that of the middle layers. To identify the mechanism, the bonding status of Li-O was inspected at the surface first layer and bulk third layer, as Li ions have an affinity to O atoms due to the latter's high electronegativity. The bond length of Li-O was calculated within 2.5 Å in the first layer,

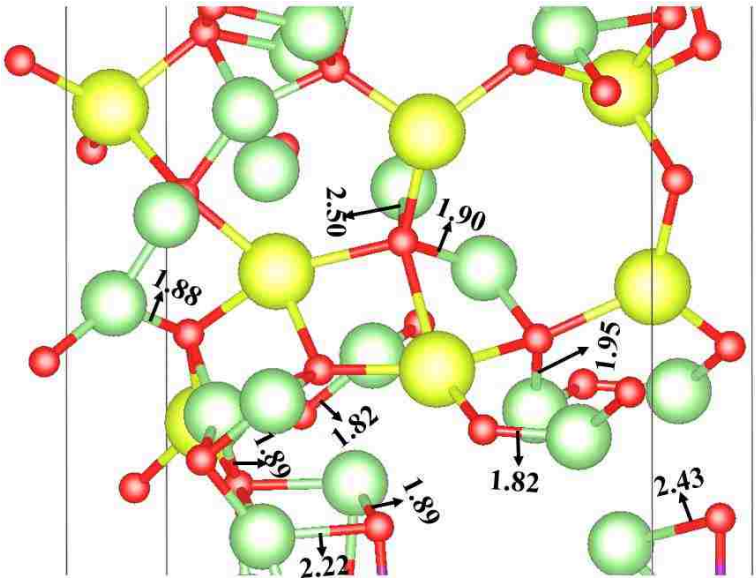

(A)

Figure 8. The bond length of Li-O in the first (A) and the third CeO_2 coating layer (B) of the five amorphous CeO_2 layer coated LMO.

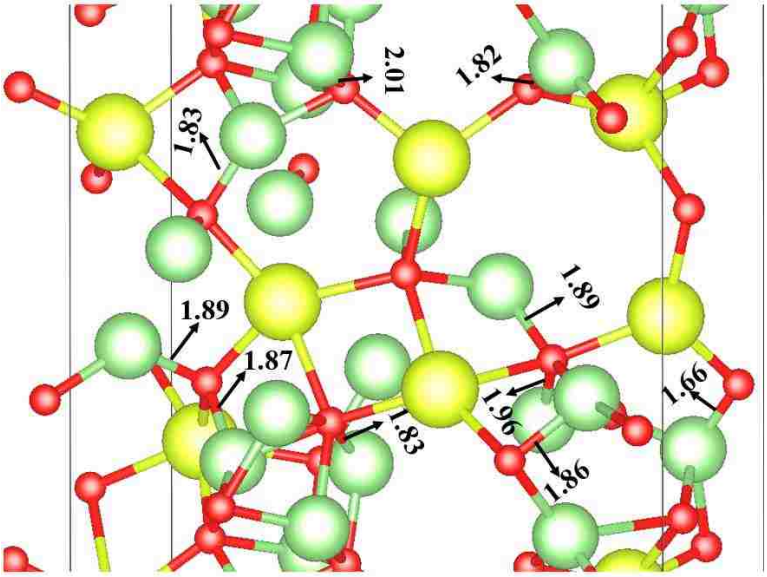

(B)

Figure 8. The bond length of Li-O in the first (A) and the third CeO_2 coating layer (B) of the five amorphous CeO_2 layer coated LMO (cont.).

Table 2. The average bond length of the first and the third CeO_2 coating layer of the five amorphous CeO_2 layer coated LMO.

Coating layer	Bond length (Å)
The first coating layer	2.04
The third coating layer	1.86

representing the surface, (Fig. 8a) and third layer, representing the bulk, (Fig. 8b) were measured by using Material Studio. The averaged bond length of Li-O in the first layer was 2.04 Å (Table 2). Figure 8B showed the bond length of Li-O in the third layer and the averaged bond length of Li-O in the third layer was 1.86 Å (Table 2), which was much shorter than the bond length in the first coating layer. The longer bond length implied weak interaction between Li and O and, therefore, higher freedom for Li ion diffusion.

Therefore, the bonding interaction analysis could explain why Li ion on the surface layer diffuse faster than in the bulk coating layer.

From the analysis above it, was found that amorphous structure was preferred than crystal structure at high thicknesses and showed higher diffusivity than a crystal structure. However, the overall diffusivity decreased as the thickness increased, which can imply that an ultrathin amorphous layer may enhance the diffusivity most effectively. A thermal treatment during coating process can change the structure.[20, 39-41] Thus, to investigate this possibility, the surface diffusion on amorphous CeO_2 coated LMO was compared to the surface diffusion on crystal CeO_2 coated LMO. To determine the minimum diffusion pathway of surface diffusion on crystal CeO2 and amorphous CeO2

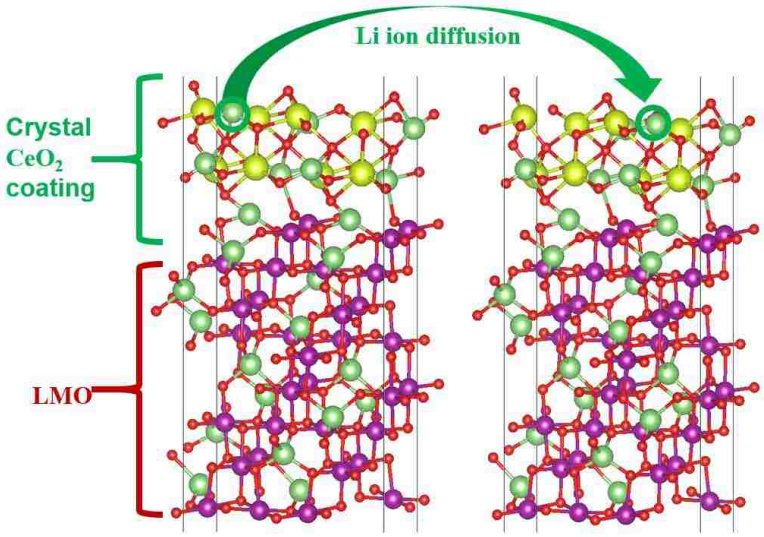

(A)

Figure 9. Initial and final configuration of crystal CeO_2 coated LMO for CINEB calculation (A); the barrier energy of Li diffusion on crystal CeO_2 coated LMO using CINEB calculations (B).

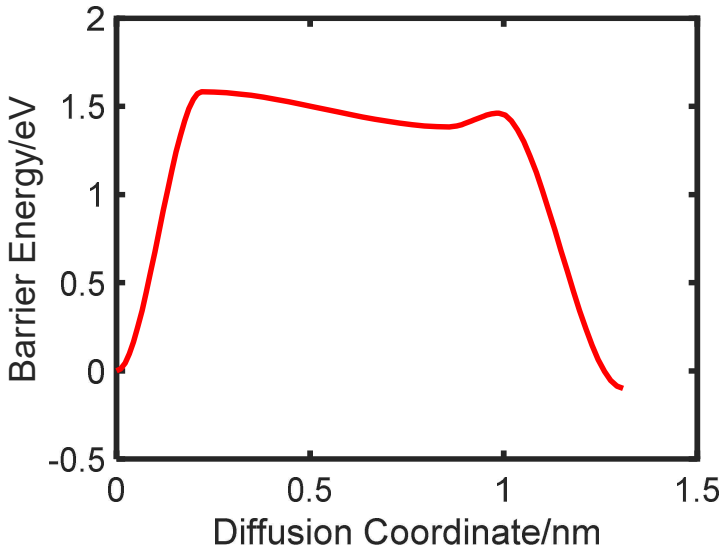

(B)

Figure 9. Initial and final configuration of crystal CeO_2 coated LMO for CINEB calculation (A); the barrier energy of Li diffusion on crystal CeO_2 coated LMO using CINEB calculations (B) (cont.).

surface, the Li ion diffusivity was calculated via the CINEB method. Before performing CINEB simulation, the initial and final crystal (Fig. 9a) and amorphous CeO_2 (Fig. 9b) coated LMO configurations were fully relaxed. When Li ion diffused from the initial position to the final position, the CINEB calculation can find the minimum energy pathway successfully. The barrier energy can be obtained via monitoring the changes of the total energy of initial, intermediate and final configurations. The barrier energy was 1.58 eV when Li diffused on crystal CeO_2 surface (Fig. 9b) while the barrier energy was 0.915 eV when Li ion diffused on amorphous CeO_2 surface (Fig. 10b). Thus, the lower barrier energy observed in the amorphous CeO_2 surface can explain why Li ions diffuse faster in ultrathin amorphous CeO_2 coating than in ultrathin crystal CeO_2 coating.

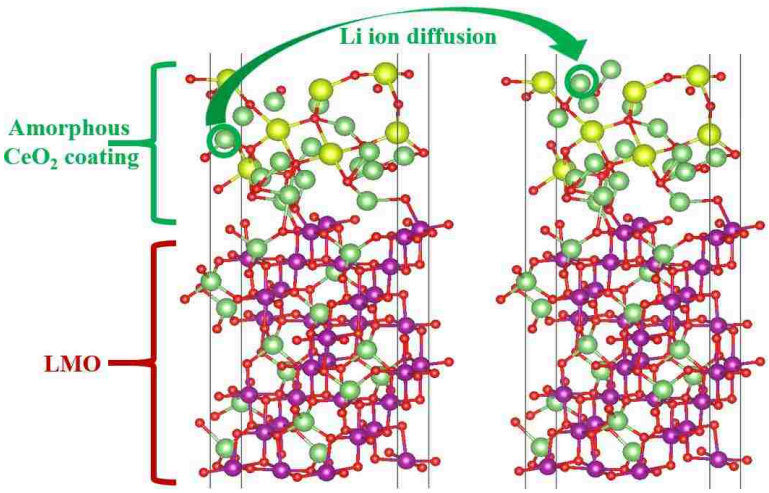

(A)

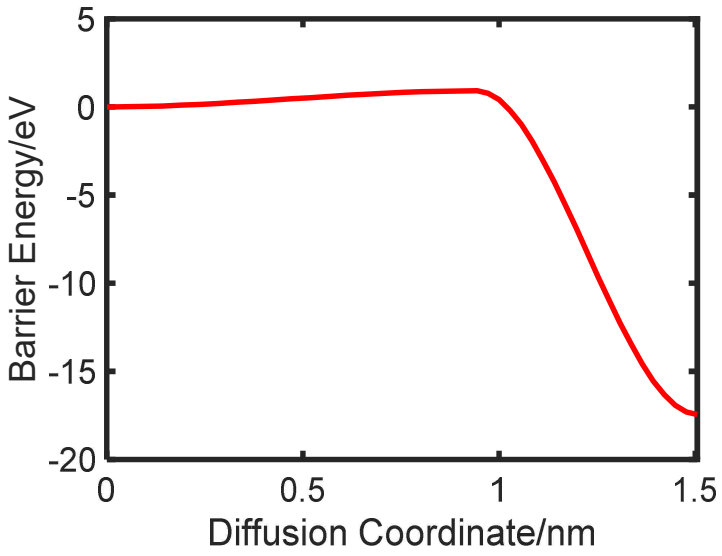

(B)

Figure 10. Initial and final configuration of amorphous CeO_2 coated LMO for CINEB calculation (A); the barrier energy of Li diffusion on amorphous CeO_2 coated LMO using CINEB calculations (B).

5. CONCLUSIONS

In this work, the fundamental mechanism of ALD coating thickness impact on Li ion diffusivity in CeO_2 coated LMO was investigated. It was found that the Li ion diffusivity on LMO and CeO2 coating surface was much higher than in bulk due to the lower barrier energy to Li diffusion in the coating layer. Through comparison of Li ion diffusivity between LMO material and CeO_2 coating, we found that Li ion diffused faster in CeO_2 coating than in LMO active material. The one layer CeO_2 coating exhibited the highest Li ion diffusivity, explained by the predominating influence of surface diffusion. With coating thickness increases, the bulk diffusion domination caused a decrease in Li ion diffusivity until a certain point, where it reached a stable value. Furthermore, the results indicated that crystal structure CeO2 coated LMO was preferred at ultrathin coating layer and, the amorphous structure was preferred at thick CeO2 coating thickness. When the coating thickness increased, the crystal CeO2 coating tended to transform into amorphous structure, which can explain the experimental observation that the Li ion diffusivity increased with coating thickness.

Finally, this work found that the Li ion diffusivity in the first and fifth layer were very high, which can be explained by the higher surface diffusion compared to the bulk diffusion in the fifth layer. The Li ion diffusivity in the first layer was higher because of the weak bonding interaction between LMO particles and CeO_2 coating layer allowing more freedom for Li ion mobility. This is the first report for ALD coating thickness impact on Li ion diffusivity in cathode particles from the atomic level, providing a reason why there is an optimal ALD CeO2 coating thickness and insight into the mechanisms of

CeO_2 coating thickness impact on Li ion diffusivity of CeO2 coated LMO for Li ion diffusivity improvement.

REFERENCES

[1] Amine, K.; Liu, J.; Kang, S.; Belharouak, I.; Hyung, Y.; Vissers, D.; Henriksen, G., Improved lithium manganese oxide spinel/graphite Li-ion cells for high-power applications. Journal of power sources 2004, 129 (1), 14-19.

[2] Park, S.-C.; Kim, Y.-M.; Han, S.-C.; Ahn, S.; Ku, C.-H.; Lee, J.-Y., The elevated temperature performance of LiMn2O4 coated with LiNi1− XCoXO2 (X= 0.2 and 1). Journal of power sources 2002, 107 (1), 42-47.

[3] Xia, Y.; Zhou, Y.; Yoshio, M., Capacity fading on cycling of 4 V Li/LiMn2 O 4 Cells. Journal of The Electrochemical Society 1997, 144 (8), 2593-2600.

[4] Aurbach, D.; Levi, M.; Gamulski, K.; Markovsky, B.; Salitra, G.; Levi, E.; Heider, U.; Heider, L.; Oesten, R., Capacity fading of LixMn2O4 spinel electrodes studied by XRD and electroanalytical techniques. Journal of Power Sources 1999, 81, 472-479.

[5] Kang, K.; Meng, Y. S.; Bréger, J.; Grey, C. P.; Ceder, G., Electrodes with high power and high capacity for rechargeable lithium batteries. Science 2006, 311 (5763), 977-980.

[6] Li, J.; Leu, M. C.; Panat, R.; Park, J., A hybrid three-dimensionally structured electrode for lithium-ion batteries via 3D printing. Materials & Design 2017, 119, 417-424.

[7] Li, J.; Liang, X.; Liou, F.; Park, J., Macro-/micro-controlled 3D lithium-ion batteries via additive manufacturing and electric field processing. Scientific reports 2018, 8 (1), 1846.

[8] Patel, R. L.; Xie, H.; Park, J.; Asl, H. Y.; Choudhury, A.; Liang, X., Significant Capacity and Cycle-Life Improvement of Lithium-Ion Batteries through Ultrathin Conductive Film Stabilized Cathode Particles. Advanced Materials Interfaces 2015, 2 (8), 1500046.

[9] George, S. M., Atomic layer deposition: an overview. Chemical reviews 2009, 110 (1), 111-131.

[10] Leskelä, M.; Ritala, M., Atomic layer deposition (ALD): from precursors to thin film structures. Thin solid films 2002, 409 (1), 138-146.

[11] Jung, Y. S.; Cavanagh, A. S.; Riley, L. A.; Kang, S. H.; Dillon, A. C.; Groner, M. D.; George, S. M.; Lee, S. H., Ultrathin direct atomic layer deposition on composite electrodes for highly durable and safe Li‐ion batteries. Advanced Materials 2010, 22 (19), 2172-2176.

[12] George, S.; Ott, A.; Klaus, J., Surface chemistry for atomic layer growth. The Journal of Physical Chemistry 1996, 100 (31), 13121-13131.

[13] Leskelä, M.; Ritala, M., Atomic layer deposition chemistry: recent developments and future challenges. Angewandte Chemie International Edition 2003, 42 (45), 5548-5554.

[14] Riley, L. A.; Van Atta, S.; Cavanagh, A. S.; Yan, Y.; George, S. M.; Liu, P.; Dillon, A. C.; Lee, S.-H., Electrochemical effects of ALD surface modification on combustion synthesized LiNi1/3Mn1/3Co1/3O2 as a layered-cathode material. Journal of Power Sources 2011, 196 (6), 3317-3324.

[15] Li, X.; Liu, J.; Meng, X.; Tang, Y.; Banis, M. N.; Yang, J.; Hu, Y.; Li, R.; Cai, M.; Sun, X., Significant impact on cathode performance of lithium-ion batteries by precisely controlled metal oxide nanocoatings via atomic layer deposition. Journal of Power Sources 2014, 247, 57-69.

[16] Guan, D.; Jeevarajan, J. A.; Wang, Y., Enhanced cycleability of LiMn2O4 cathodes by atomic layer deposition of nanosized-thin Al2O3 coatings. Nanoscale 2011, 3 (4), 1465-9.

[17] Jung, Y. S.; Cavanagh, A. S.; Yan, Y.; George, S. M.; Manthiram, A., Effects of atomic layer deposition of Al2O3 on the Li [Li0. 20Mn0. 54Ni0. 13Co0. 13] O2 cathode for lithium-ion batteries. Journal of the Electrochemical Society 2011, 158 (12), A1298-A1302.

[18] Panda, S. K.; Yoon, Y.; Jung, H. S.; Yoon, W.-S.; Shin, H., Nanoscale size effect of titania (anatase) nanotubes with uniform wall thickness as high performance anode for lithium-ion secondary battery. Journal of Power Sources 2012, 204, 162-167.

[19] Kong, J.-Z.; Ren, C.; Tai, G.-A.; Zhang, X.; Li, A.-D.; Wu, D.; Li, H.; Zhou, F., Ultrathin ZnO coating for improved electrochemical performance of LiNi0.5Co0.2Mn0.3O2 cathode material. Journal of Power Sources 2014, 266, 433-439.

[20] Zhao, J.; Wang, Y., Atomic layer deposition of epitaxial ZrO2 coating on LiMn2O4 nanoparticles for high-rate lithium ion batteries at elevated temperature. Nano Energy 2013, 2 (5), 882-889.

[21] Snyder, M. Q.; Trebukhova, S. A.; Ravdel, B.; Wheeler, M. C.; DiCarlo, J.; Tripp, C. P.; DeSisto, W. J., Synthesis and characterization of atomic layer deposited titanium nitride thin films on lithium titanate spinel powder as a lithium-ion battery anode. Journal of power sources 2007, 165 (1), 379-385.

[22] Kohandehghan, A.; Kalisvaart, P.; Cui, K.; Kupsta, M.; Memarzadeh, E.; Mitlin, D., Silicon nanowire lithium-ion battery anodes with ALD deposited TiN coatings demonstrate a major improvement in cycling performance. Journal of Materials Chemistry A 2013, 1 (41), 12850.

[23] Li, Y.; Sun, Y.; Xu, G.; Lu, Y.; Zhang, S.; Xue, L.; Jur, J. S.; Zhang, X., Tuning electrochemical performance of Si-based anodes for lithium-ion batteries by employing atomic layer deposition alumina coating. J. Mater. Chem. A 2014, 2 (29), 11417-11425.

[24] Jung, Y. S.; Cavanagh, A. S.; Riley, L. A.; Kang, S. H.; Dillon, A. C.; Groner, M. D.; George, S. M.; Lee, S. H., Ultrathin direct atomic layer deposition on composite electrodes for highly durable and safe Li-ion batteries. Adv Mater 2010, 22 (19), 2172-6.

[25] Park, J. S.; Meng, X.; Elam, J. W.; Hao, S.; Wolverton, C.; Kim, C.; Cabana, J., Ultrathin Lithium-Ion Conducting Coatings for Increased Interfacial Stability in High Voltage Lithium-Ion Batteries. Chemistry of Materials 2014, 26 (10), 3128-3134.

[26] Dominko, R.; Bele, M.; Gaberscek, M.; Remskar, M.; Hanzel, D.; Pejovnik, S.; Jamnik, J., Impact of the carbon coating thickness on the electrochemical performance of LiFePO4/C composites. Journal of the Electrochemical Society 2005, 152 (3), A607-A610.

[27] Zhao, J.; Wang, Y., Ultrathin Surface Coatings for Improved Electrochemical Performance of Lithium Ion Battery Electrodes at Elevated Temperature. The Journal of Physical Chemistry C 2012, 116 (22), 11867-11876.

[28] Scott, I. D.; Jung, Y. S.; Cavanagh, A. S.; Yan, Y.; Dillon, A. C.; George, S. M.; Lee, S.-H., Ultrathin coatings on nano-LiCoO2 for Li-ion vehicular applications. Nano letters 2010, 11 (2), 414-418.

[29] Jung, Y. S.; Cavanagh, A. S.; Dillon, A. C.; Groner, M. D.; George, S. M.; Lee, S.-H., Enhanced stability of LiCoO2 cathodes in lithium-ion batteries using surface modification by atomic layer deposition. Journal of The Electrochemical Society 2010, 157 (1), A75-A81.

[30] Kang, J.; Han, B., First-principles study on the thermal stability of LiNiO2 materials coated by amorphous Al2O3 with atomic layer thickness. ACS applied materials & interfaces 2015, 7 (21), 11599-11603.

[31] Kresse, G.; Furthmüller, J., Efficient iterative schemes for ab initio total-energy calculations using a plane-wave basis set. Physical review B 1996, 54 (16), 11169.

[32] Perdew, J. P.; Burke, K.; Ernzerhof, M., Generalized gradient approximation made simple. Physical review letters 1996, 77 (18), 3865.

[33] Yang, J.-H.; Park, J.-S.; Kang, J.; Wei, S.-H., First-principles multiple-barrier diffusion theory: The case study of interstitial diffusion in CdTe. Physical Review B 2015, 91 (7), 075202.

[34] Wang, Z.; Su, Q.; Deng, H.; He, W.; Lin, J.; Fu, Y. Q., Modelling and simulation of electron-rich effect on Li diffusion in group IVA elements (Si, Ge and Sn) for Li ion batteries. Journal of Materials Chemistry A 2014, 2 (34), 13976-13982.

[35] Ning, F.; Li, S.; Xu, B.; Ouyang, C., Strain tuned Li diffusion in LiCoO2 material for Li ion batteries: A first principles study. Solid State Ionics 2014, 263, 46-48.

[36] Tian, H.; Seh, Z. W.; Yan, K.; Fu, Z.; Tang, P.; Lu, Y.; Zhang, R.; Legut, D.; Cui, Y.; Zhang, Q., Theoretical Investigation of 2D Layered Materials as Protective Films for Lithium and Sodium Metal Anodes. Advanced Energy Materials 2017, 7 (13), 1602528.

[37] Xu, S.; Jacobs, R. M.; Nguyen, H. M.; Hao, S.; Mahanthappa, M.; Wolverton, C.; Morgan, D., Lithium transport through lithium-ion battery cathode coatings. Journal of Materials Chemistry A 2015, 3 (33), 17248-17272.

[38] Tang, X.-C.; Song, X.-W.; Shen, P.-Z.; Jia, D.-Z., Capacity intermittent titration technique (CITT): A novel technique for determination of Li+ solid diffusion coefficient of LiMn2O4. Electrochimica Acta 2005, 50 (28), 5581-5587.

[39] Han, B.; Paulauskas, T.; Key, B.; Peebles, C.; Park, J. S.; Klie, R. F.; Vaughey, J. T.; Dogan, F., Understanding the role of temperature and cathode composition on interface and bulk: Optimizing aluminum oxide coatings for Li-ion cathodes. ACS applied materials & interfaces 2017, 9 (17), 14769-14778.

[40] Wang, J.-H.; Wang, Y.; Guo, Y.-Z.; Ren, Z.-Y.; Liu, C.-W., Effect of heat-treatment on the surface structure and electrochemical behavior of AlPO 4-coated LiNi 1/3 Co 1/3 Mn 1/3 O 2 cathode materials. Journal of Materials Chemistry A 2013, 1 (15), 4879-4884.

[41] Zhao, J.; Wang, Y., Surface modifications of Li-ion battery electrodes with various ultrathin amphoteric oxide coatings for enhanced cycleability. Journal of Solid State Electrochemistry 2013, 17 (4), 1049-1058.

IV. FIRST-PRINCIPLES STUDY OF THE INTERFACIAL PROPERTY OF SOLID ELECTROLYTE INTERPHASE (SEI) LAYER COMPONENTS IN LITHIUM-ION BATTERIES

ABSTRACT

The Solid-Electrolyte Interphase (SEI) layer serves as a crucial function in protecting active material particles in anode electrodes for Lithium-ion batteries from the electrolyte decomposition. However, under several Li (de)intercalation cycles, active material particles undergo significant volume changes that create stresses in the SEI layer, eventually leading to mechanical failure of the layer. To date, its mechanical failure mechanism, in particular, the interface toughness among the constituents in SEI layer, which is composed of numerous organic and inorganic products, is unclear. In this work, two aspects of interfacial properties have been focused including mechanical bonding strength and electron transport among the constituent materials. For the mechanical aspect, we investigated the mechanical adherence property and separation response of SEI layer components between inorganic-inorganic (LiF/Li_2CO_3 and LiF/Li_2O), inorganic-organic (LiF/Li_2EC) and organic-organic (Li_2EC/Li_2EDC) by first-principles calculations. The maximum theoretical stress of LiF/Li_2CO_3, LiF/Li_2O and Li_2EC/Li_2EDC interfaces were 0.0094GPa, 0.0085GPa and 0.0037GPa, respectively, which indicated the fracture strength of inorganic-inorganic components was higher than organic-organic components. For the electron transport, LiF/Li_2EC interface showed the highest tunneling barrier energy, while Li_2EC/Li_2EDC showed the lowest tunneling barrier energy, which suggested that it was difficult for electrons to pass through the inorganic interface compared to the organic components interface. The understanding on

the mechanical stability and electronic transport properties of the SEI layer constituent materials provides insight into failure mechanism of layers and their optimal configurations.

1. INTRODUCTION

The interface chemistry of electrode and electrolyte is critical for Lithium ion Battery (LIB) performance[1-6]. Most electrolyte solvents are not electrochemically stable, which degrade electrode surfaces into decomposition products to form a passivation layer called the Solid Electrolyte Interphase (SEI) layer. During initial cycles, the SEI layer serves as an ionic conductor for Li ions while blocking the transfer of electrons, thus protecting electrode materials from further decomposition. However, the SEI layer does not keep its initial configuration and properties due to continual growth of the layer over numerous cycles and may become non-uniform and defective. As Li ions continuously migrate through the bulk of the SEI to deposit onto and strip from the electrode surface[2], the continuous decomposition reactions will cause large volumetric variations which pulverize the SEI layer and exposes electrode materials to further decomposition. Over time, new decomposition products that allow electrons and solvents to pass through the defective SEI layer can form, further aggravating electrolyte decomposition. These ultimately result in capacity loss and accelerated LIB capacity fade[7-9], increased interfacial resistance, reduced cycle life, and the critical safety issue of short circuiting[4, 9-13].

The SEI layer is composed of numerous organic and inorganic components that behave in different ways. One work showed that the SEI layer components Li_2EDC and

Li_2BDC precipitate either in amorphous or ordered phases at lower temperature[14], where slower SEI formation was expected from the ordered phase while fast SEI formation would lead to more disordered and glass-like SEI[14]. In another study, the capacity loss was found to be proportional to the surface area of the SEI layer, and that thicker SEI layers would increase resistance to Li ion transport[3, 15]. The results of another model showed that the maximum stress in the active layer increased with respect to decreasing SEI thickness, and the mechanical stability of the SEI could be improved by reducing the modulus of the SEI layer[16]. The SEI layer component and its elastic property has been extensively investigated in order to obtain the behavior of the layer during cell operation[8, 17-18]. The SEI layer on an electrode consists of an inner layer and outer layer, where the inner layer was comprised of the inorganic components, such as Li_2CO_3[19], Li_2O[20], and LiF[21-24] and the outer layer was composed of organic constituents, which consisted of alkyl dicarbonate species[25-28] such as Li_2EC, Li_2EDC, and Li_2BDC. It is reported that the Young's modulus of SEI layer components ranged from 2.4GPa to 58.1GPa in the order of organic, inorganic components, where the crystalline inorganic component LiF showed the highest value (135GPa) among SEI species[29], which indicated that the inorganic components were more stiff than inorganic components thus making it more difficult for electrons to pass through. Furthermore, the three-dimensional multi-layer SEI structure and its mechanical properties were measured by scanning force spectroscopy[30], which showed that the SEI layer on a silicon anode was highly inhomogeneous with single-, double-, and multi-layered, porous and sandwiched structures, and the thickness of the SEI layer widely varied from 0-90 nm during the charge and discharge process.

While numerous works concerning the SEI layer have been done that reveal its formation and growth mechanisms and properties on the subsequent impact on battery performance, the interfacial mechanical property, including interfacial stability and toughness, between different SEI layer components (such as inorganic-inorganic, inorganic-organic and organic-organic interface) has yet to be investigated. Without this knowledge, the failure mechanisms related to the mechanical and interfacial properties of the SEI cannot be effectively addressed. Therefore, the fundamental understanding of the behavior between SEI layer components can reveal critical mechanical and interfacial property of SEI that can be utilized to enhance battery performance. To address the complex interactions between electrode, electrolyte, and formed SEI components, and lack of reliable experimental technologies[6] to observe them, computational modelling has been an efficient method to predict the fundamental SEI layer formation mechanism and mechanical properties[14]. Therefore, in this work, first-principles calculations were performed to predict the interfacial mechanical property of SEI layer components via a dynamic separation response study. The interfacial mechanical property can be predicted via traction-separation curve, which has previously been used to simulate fracture employing cohesive zones[31] to study crack formation and also be used to interpret bonding property. Furthermore, the interfacial property between the inorganic and organic SEI components may possess electronic properties that impact electron transport. Therefore, the electron transport property at the interface of inorganic and organic SEI components was examined via Density of State (DOS) calculation. The results of this work reveal the mechanical and electronic interaction between SEI components at their interface which provides critical insight into SEI mechanical failure.

2. COMPUTATIONAL DETAILS

2.1. THEORETICAL CALCULATIONS

First-principles calculations in this work were performed using Vienna Ab-initio Simulation (VASP) Package[32-33]. The exchange and correlation functionals were treated with the Generalized Gradient Approximation (GGA) of Perdew−Burke−Ernzerhof (PBE). The Projector Augmented Wave (PAW) method was applied for electron-ion interaction[34], and the electronic wave functions were expanded on a plane wave basis set of 400 eV for all systems. The SEI layer components between inorganic-inorganic, organic-organic, organic-inorganic were investigated. For inorganic-inorganic components interaction, the LiF/Li_2CO_3 and LiF/Li_2O are considered. For inorganic-organic interaction, the LiF/Li_2EC is considered. While for organic and organic interaction, the Li_2EC/Li_2EDC component is considered. The LiF, Li_2O and Li_2CO_3 slab structure with 001 surface oriented were created. The Li_2EC and Li_2EDC structures were prepared using material studio. Then, the quenching process was applied to prepare amorphous Li_2EC and Li_2EDC. The LiF/Li_2CO_3, LiF/Li_2O, LiF/Li_2EC and Li_2EC/Li_2EDC interface configurations were created via combining two free slab structures together. During the SEI layer components separation process, all systems are fully relaxed to reach the required accuracy. The structure optimization was used to force and energy convergence until 0.02 eV/Å, 10^{-4} eV/supercell respectively.

2.2. THE BINDING ENERGY CALCULATION

For each two layer components of the SEI, the separation distance was set at 1 Å, 2 Å, 3 Å, 4 Å, and 5 Å. The binding energy expression is given as follows[35-36]:

$$E_b = \frac{E_{slabA} + E_{slabB} - E_{AB}}{2A} \quad (1)$$

where E_A and E_B are the total energy of surface A and surface B respectively. E_{AB} is the total energy of combination of surface A and surface B.

2.3. THE THEORETICAL STRESS AND FINAL SEPARATION CALCULATION

An important fundamental quantity that controls the mechanical strength of SEI components interface is the maximum theoretical stress. The theoretical stress is a measure of the deformation of two components upon applying internal and external force on the interface, which can be obtained according to the derivative of energy-displacement data[31] calculated by

$$\sigma_{th} = \frac{dE_b}{d\Delta}$$

where Δ is the displacement from the equilibrium inter-planar distance.

The final separation σ_f is the displacement at which the two surface are complete separated, which can be expressed by following formula[31]:

$$\sigma_f = \frac{2WoS}{\sigma_{th}}$$

where WoS is the work of separation, which equals the absolute value of binding energy.

2.4. THE DOS CALCULATION OF INTERFACES OF SEI COMPONENTS

The oxidation of anode particles is affected by the electronic property of SEI layer interface. The higher electronic resistant interface could block electron transport from electrolyte to anode particle surface. Therefore, the electronic property of SEI layer interface was investigated via performing density of state calculations. PDOS was

calculated through using a static calculation with 3 × 3 × 1 Monkhorst-Pack mesh. The electronic wave functions were expanded on a plane wave basis set of 400 eV and the energy convergence until 10^{-4} eV/supercell.

3. RESULTS AND DISCUSSION

3.1. THE BINDING ENERGY AND TRACTION OF INTERFACES OF SEI COMPONENTS

The mechanical property of SEI layer components was investigated via a traction-separation law. From the traction-separation curve, the fracture strength and final separation of different SEI layer interfaces can be obtained. The traction-separation was calculated based on energy-displacement curve. Thus, the binding energy of LiF/Li_2CO_3, LiF/Li_2O, LiF/Li_2EC and Li_2EC/Li_2EDC were calculated as a function of separation distance. The LiF/Li_2CO_3, LiF/Li_2O, LiF/Li_2EC and Li_2EC/Li_2EDC structure are shown in Fig. 1. The binding energy of LiF/Li_2CO_3 decreased from 1 Å to 3 Å, where the binding energy of LiF/Li_2CO_3 reached the minimum energy of -0.062 eV at the separation distance of 3 Å (Fig. 2A), suggesting that the LiF/Li_2CO_3 interface reached its most stable state at this distance. After reaching the minimum value, the binding energy increased with increasing separation distance. The traction as a function of separation distance of LiF/Li_2CO_3 is shown in Fig. 3, which was calculated by taking the derivative of the energy-displacement curve. The theoretical stress of LiF/Li_2CO_3 was 0.0094 GPa (Fig. 3), indicating that the stress on LiF/Li_2CO_3 should not be exceeded as a higher value will cause LiF/Li_2CO_3 interface fracture, accelerating LIB degradation.

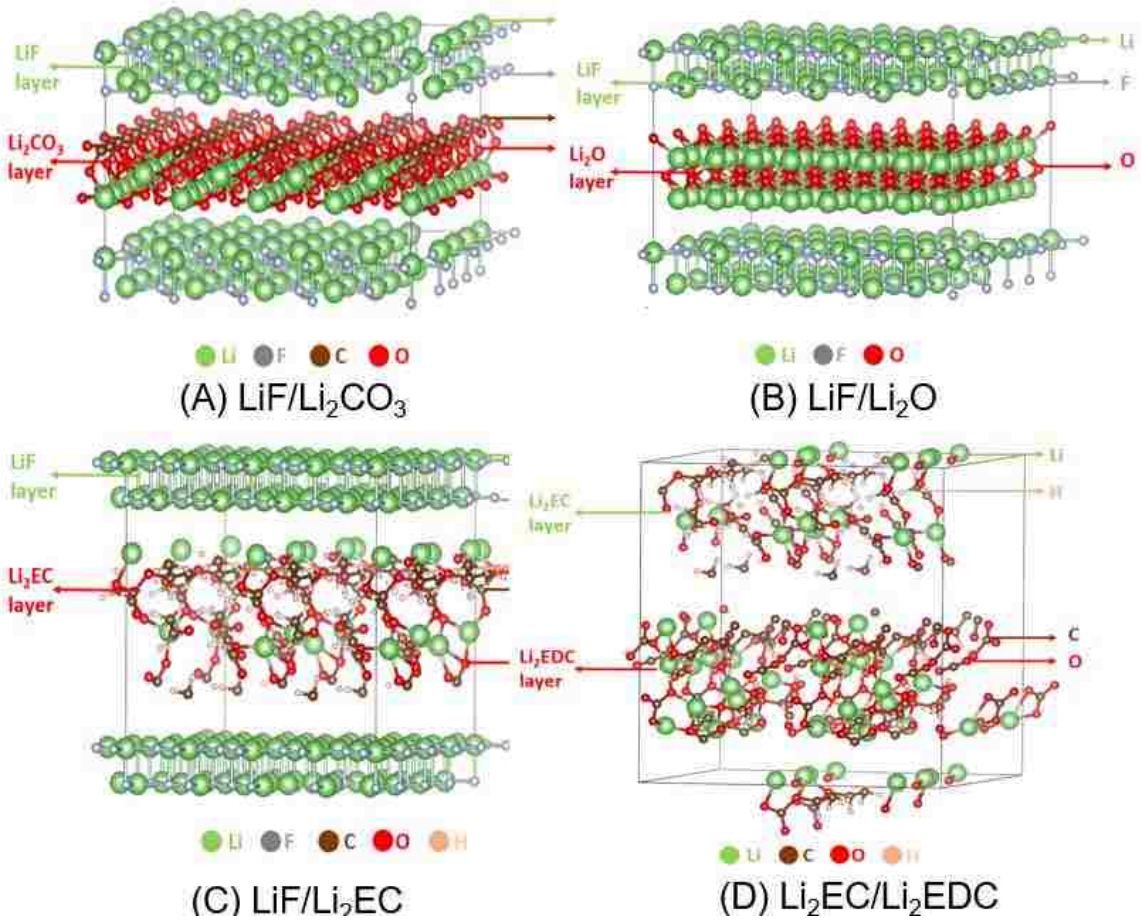

Figure 1. The LiF/Li_2CO_3 (A), LiF/Li_2O (B), LiF/Li_2EC (C) and Li_2EC/Li_2EDC (D) interfacial structures.

The other different inorganic-inorganic SEI layer components LiF/Li_2O were then investigated. The binding energy of LiF/Li_2O decreased from 1 Å to 2 Å (Fig. 2B), after which it increased with increasing separation distance. The interface of LiF/Li_2O reached the most stable state at 2 Å, at which the binding energy reached a minimum -0.0985 eV. Therefore, the work of separation is 0.0985 eV, meaning that this energy value is needed

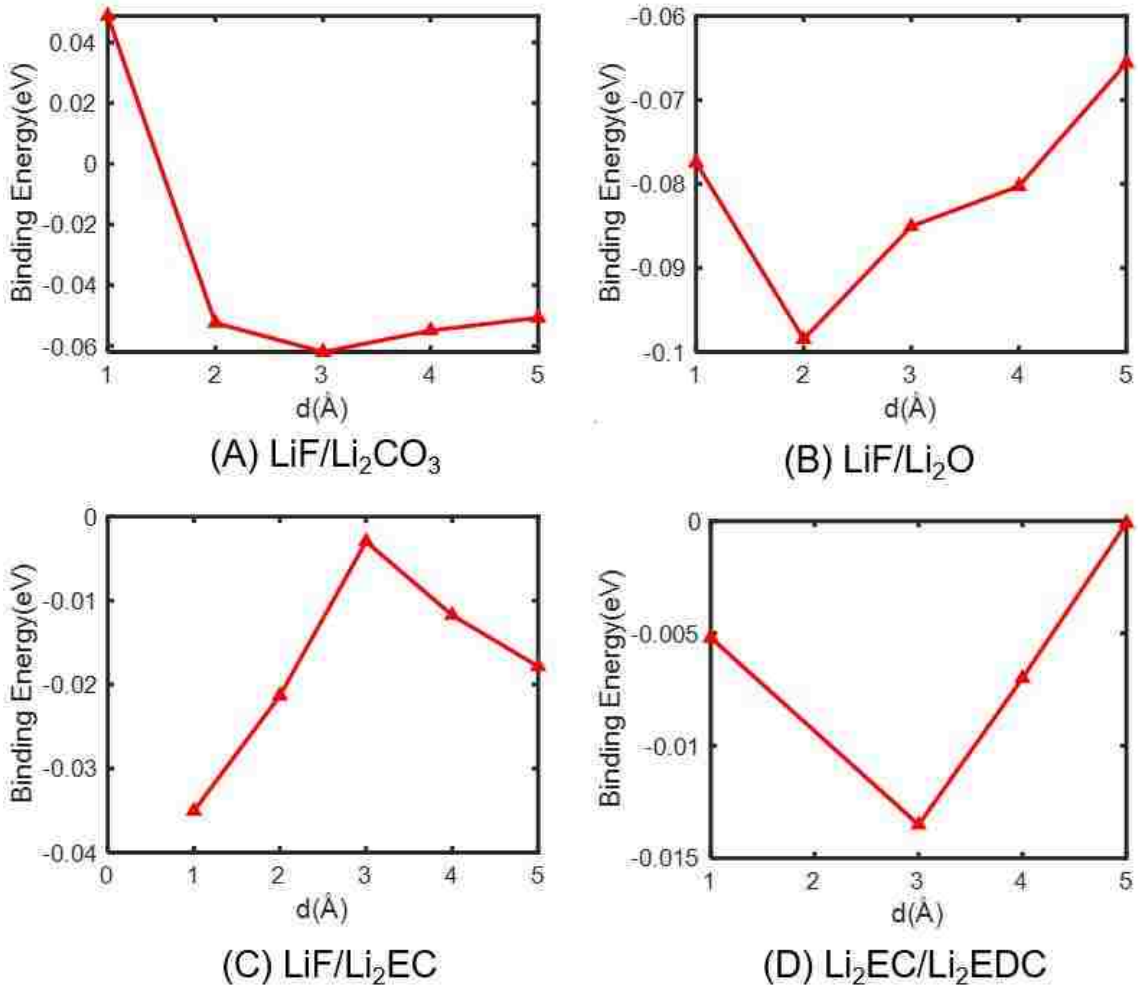

Figure 2. The binding energy of LiF/Li_2CO_3 (A), LiF/Li_2O (B), LiF/Li_2EC (C) and Li_2EC/Li_2EDC (D) as a function of separation distance.

to separate LiF and Li_2O into two components. Based on the energy-distance curve, the traction as a function of separation distance is shown in Fig. 3. We found the theoretical stress was 0.0085 GPa, which was slightly lower than that of LiF/Li_2CO_3 components stress of 0.0095 GPa (Fig. 3) but comparable. The binding energy and traction of inorganic-organic components as a function of separation distance was then inspected. Surprisingly, as shown in Fig. 2C, we found that the binding energy of LiF/Li_2EDC

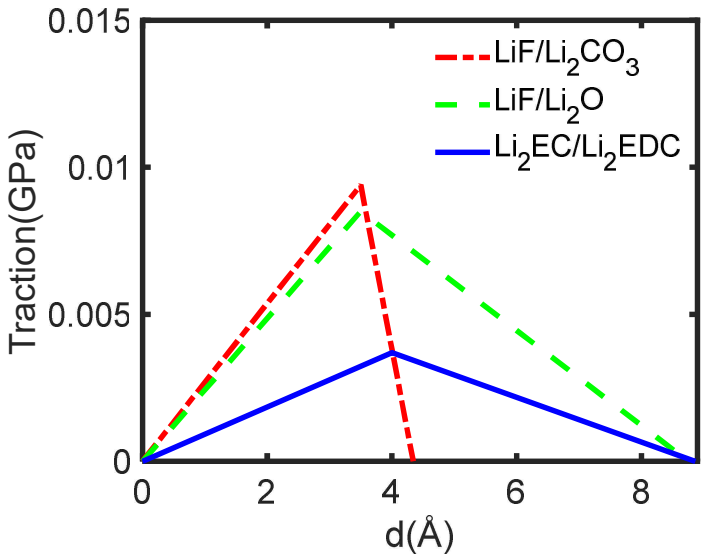

Figure 3. The traction response of LiF/Li_2CO_3 interface, LiF/Li_2O interface and Li_2EC/Li_2EDC interface.

increased with the separation distance until it reached 3 Å. Then it decreased with further increase in the separation distance, which indicated that the interaction between LiF and Li_2EC was repulsive. The inorganic-organic bonding was not energetically favorable, suggesting that after the initial inorganic components are formed on anode particles surface, the formation of organic components on the inorganic components' surface was difficult. This is the first finding for inorganic and organic interface formation phenomena, which can signal that the defect SEI layer formation can be prevented via adding additive material after initial SEI layer formation. Furthermore, the organic-organic interface property was investigated. Li_2EC and Li_2EDC are two organic components found in the SEI layer, and were thus used for the organic-organic separation response in this work. As shown in Fig. 2D, the binding energy decreased with increasing separation distance until 3 Å. The binding energy at equilibrium distance was -0.0135 eV, thus the work of separation of Li_2EC/Li_2EDC was 0.0135eV, which is needed to be

reached to separate Li_2EC/Li_2EDC into two components. The interface of Li_2EC/Li_2EDC is the most stable when separation distance is 3 Å. Then, the binding energy increases with increasing separation distance. The traction as a function of separation distance is shown in Fig. 3. The theoretical stress is 0.0037 GPa, which indicates that the fracture strength of organic interface is lower than inorganic interface. From traction-separation curve, the final separation displacement can be obtained. The area under traction-separation curve equals the work of separation. As is shown in Fig. 3, the final separation distance of LiF/Li_2CO_3, LiF/Li_2O and Li_2EC/Li_2EDC interface are 4.34 Å, 8.75 Å and 8.86 Å respectively, suggesting that the fracture distance of organic components is larger than inorganic components.

3.2. THE DOS OF INTERFACES OF SEI COMPONENTS

During LIB operation, it is required that electrons do not pass through the SEI layer to reach anode surface and cause the oxidation of anode. Therefore, investigation of the electronic property of SEI layer interface is necessary. The Density of State (DOS) of inorganic-inorganic components (LiF/Li_2CO_3 and LiF/Li_2O), inorganic-organic components (LiF/Li_2EC) and organic-organic components (Li_2EC/Li_2EDC) was examined, where the electron tunneling barrier was obtained directly from DOS profiles by taking the difference of conduction band minimum and Fermi level (0eV) [37]. The electron tunneling barrier from Li_2CO_3 to LiF was calculated to be close to 0.9 eV (Fig. 4a) while Li_2O to LiF (Fig. 4b) was 0.54 eV, and the electron tunneling barrier from Li_2EC to LiF is 2.21 eV (Fig. 4c). However, the electron tunneling barrier from Li_2EC to Li_2EDC (Fig. 4d) was close to 0 eV. From the electronic property examination of SEI

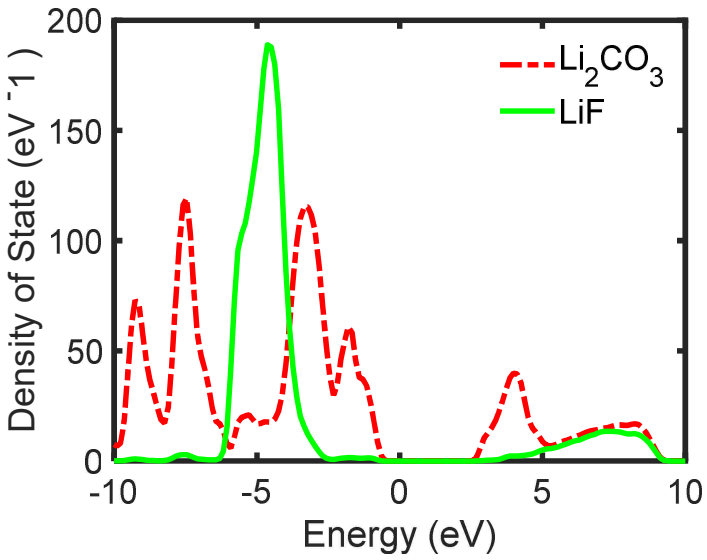

(A)

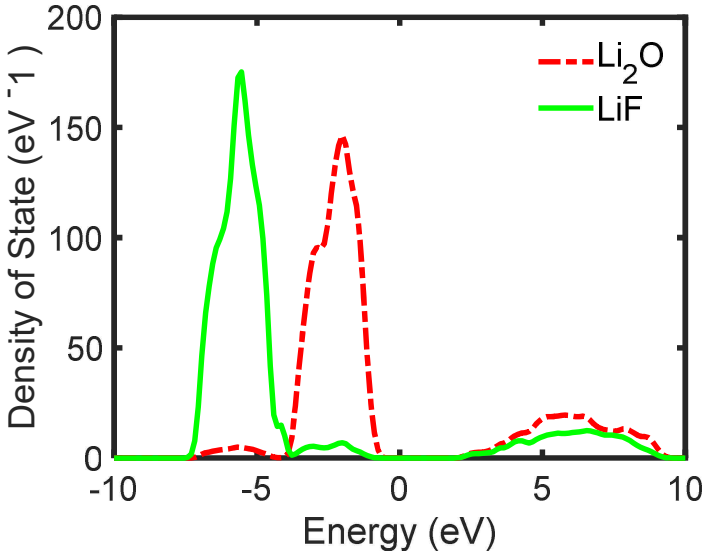

(B)

Figure 4. Density of state of LiF/Li_2CO_3 (A), LiF/Li_2O (B), LiF/Li_2EC (C), and Li_2EDC/Li_2EC (D).

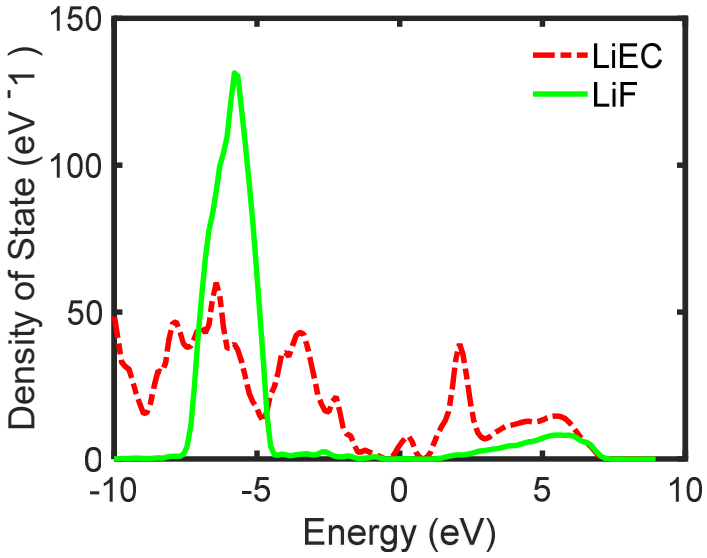

(C)

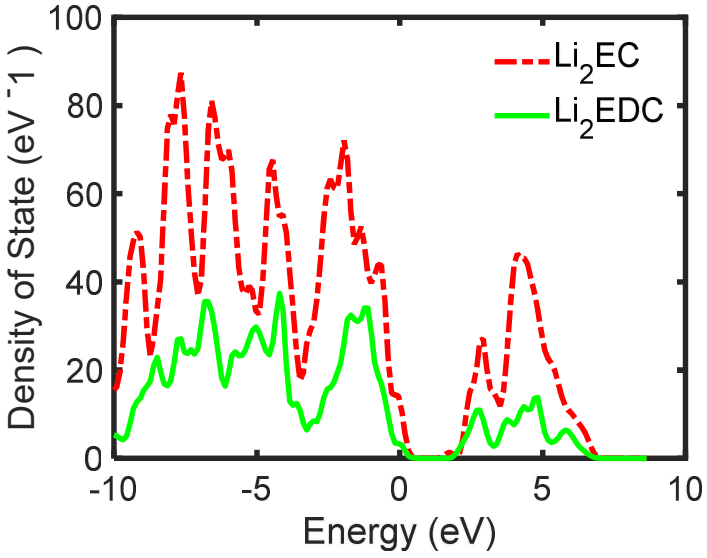

(D)

Figure 4. Density of state of LiF/Li_2CO_3 (A), LiF/Li_2O (B), LiF/Li_2EC (C), and Li_2EDC/Li_2EC (D) (cont.).

components, we found that the electron tunneling barrier from organic Li_2EC to inorganic LiF components was the highest, while the electron tunneling barrier from organic Li_2EC to organic Li_2EDC was the lowest, which indicated that electrons can easily pass through organic-organic components, as opposed to inorganic-inorganic components, where a higher resistance for electron transport was found. Thus, inorganic components can more effectively block electrons from reaching anode particles thus protecting electrode materials from further decomposition.

4. CONCLUSION

In this work, the interfacial property of SEI layer components was investigated to reveal their fundamental interfacial behavior and impact on mechanical failure of the overall SEI layer. To study the interfacial stability of SEI layer components, the binding energy of LiF/Li_2CO_3, LiF/Li_2O, LiF/Li_2EC and Li_2EC/Li_2EDC was inspected as a function of separation distance. We found that the binding energy of LiF/Li_2CO_3, LiF/Li_2O, and Li_2EC/Li_2EDC reached the minimum energy of -0.062 eV, -0.0985 eV, -0.0135 eV respectively, indicating that the interface between inorganic interfaces was more stable than organic interfaces. Furthermore, the theoretical stresses of LiF/Li_2CO_3, LiF/Li_2O, and Li_2EC/Li_2EDC were 0.0094 GPa, 0.0085 GPa and 0.0037 GPa respectively, implying that the fracture strength between inorganic was higher than organic components and that inorganic interfaces were more stable. Besides, the failure displacement of organic-organic components were higher than inorganic. Furthermore, we found that the binding energy curve of LiF/Li_2EC could not reach a minimum, indicating that the interaction between LiF and Li_2EC is repulsive, indicating that the

inorganic-organic interface was unstable. The electron transport mechanism of SEI layer was investigated via DOS calculation, where the electron tunneling barrier from organic Li_2EC to inorganic LiF components was the highest, while the electron tunneling barrier from organic Li_2EC to organic Li_2EDC was 0 eV, which suggested that inorganic components could effectively block electrons to protect active material from further decomposition. This work revealed the interfacial stability and fracture strength of SEI layer components and provided critical insight into the behavior of the SEI layer that can be utilized to improve the performance of LIBs.

REFERENCES

[1] Aurbach, D., M. Moshkovich, Y. Cohen, and A. Schechter, The study of surface film formation on noble-metal electrodes in alkyl carbonates/Li salt solutions, using simultaneous in situ AFM, EQCM, FTIR, and EIS. Langmuir 1999, 15 (8).

[2] Peled, E., The electrochemical behavior of alkali and alkaline earth metals in nonaqueous battery systems—the solid electrolyte interphase model. Journal of the Electrochemical Society 1979, 126 (12).

[3] Lee, Y. M.; Lee, J. Y.; Shim, H.-T.; Lee, J. K.; Park, J.-K., SEI Layer Formation on Amorphous Si Thin Electrode during Precycling. Journal of the Electrochemical Society 2007, 154 (6), A515.

[4] Cheng, X. B.; Zhang, R.; Zhao, C. Z.; Wei, F.; Zhang, J. G.; Zhang, Q., A Review of Solid Electrolyte Interphases on Lithium Metal Anode. Adv Sci (Weinh) 2016, 3 (3), 1500213.

[5] Liu, Z., Y. Qi, Y. X. Lin, L. Chen, P. Lu, and L. Q. Chen, Interfacial study on solid electrolyte interphase at Li metal anode: implication for Li dendrite growth. Journal of the Electrochemical Society 2016, 163 (3).

[6] Wang, A.; Kadam, S.; Li, H.; Shi, S.; Qi, Y., Review on modeling of the anode solid electrolyte interphase (SEI) for lithium-ion batteries. npj Computational Materials 2018, 4 (1).

[7] Vetter, J.; Novák, P.; Wagner, M. R.; Veit, C.; Möller, K. C.; Besenhard, J. O.; Winter, M.; Wohlfahrt-Mehrens, M.; Vogler, C.; Hammouche, A., Ageing mechanisms in lithium-ion batteries. Journal of Power Sources 2005, 147 (1-2), 269-281.

[8] Gauthier, M.; Carney, T. J.; Grimaud, A.; Giordano, L.; Pour, N.; Chang, H. H.; Fenning, D. P.; Lux, S. F.; Paschos, O.; Bauer, C.; Maglia, F.; Lupart, S.; Lamp, P.; Shao-Horn, Y., Electrode-electrolyte interface in Li-ion batteries: current understanding and new insights. J Phys Chem Lett 2015, 6 (22), 4653-72.

[9] Yoshida, T.; Takahashi, M.; Morikawa, S.; Ihara, C.; Katsukawa, H.; Shiratsuchi, T.; Yamaki, J.-i., Degradation Mechanism and Life Prediction of Lithium-Ion Batteries. Journal of The Electrochemical Society 2006, 153 (3), A576.

[10] Yazami, R., and Yvan F. Reynier, Mechanism of self-discharge in graphite–lithium anode. Electrochimica Acta 2002, 47 (8).

[11] Inaba, M., Hanako Tomiyasu, Akimasa Tasaka, Soon-Ki Jeong, and Zempachi Ogumi, Atomic force microscopy study on the stability of a surface film formed on a graphite negative electrode at elevated temperatures. Langmuir 2004, 20 (4).

[12] Smith, A. J., J. Chris Burns, Xuemei Zhao, Deijun Xiong, and J. R. Dahn, A high precision coulometry study of the SEI growth in Li/graphite cells. Journal of The Electrochemical Society 2011, 158 (5).

[13] Lee, Y. K., Jonghyun Park, and Wei Lu, Electronic and Bonding Properties of LiMn2O4 Spinel with Different Surface Orientations and Doping Elements and Their Effects on Manganese Dissolution. Journal of The Electrochemical Society 2016, 163 (7).

[14] Bedrov, D.; Borodin, O.; Hooper, J. B., Li+ Transport and Mechanical Properties of Model Solid Electrolyte Interphases (SEI): Insight from Atomistic Molecular Dynamics Simulations. The Journal of Physical Chemistry C 2017, 121 (30), 16098-16109.

[15] Fong, R., Ulrich Von Sacken, and Jeff R. Dahn, Studies of lithium intercalation into carbons using nonaqueous electrochemical cells. Journal of The Electrochemical Society 1990, 137 (7).

[16] He, Y.; Hu, H., Analysis of lithium ion concentration and stress in the solid electrolyte interphase on the graphite anode. Phys Chem Chem Phys 2015, 17 (36), 23565-72.

[17] Ogumi, Z., Interfacial Reactions of Lithium-Ion Batteries. Electrochemistry 2010, 78, 317.

[18] Yang, H.-W.; Lee, D. I.; Kang, N.; Kang, W. S.; Kim, S.-J., Formation of physically durable and performance sensitive solid-electrolyte interphase of SiO_x anode for lithium-ion battery. Materials Research Letters 2018, 7 (3), 89-96.

[19] Yang, C. R., Y. Y. Wang, and C. C. Wan., Composition analysis of the passive film on the carbon electrode of a lithium-ion battery with an EC-based electrolyte. Journal of power sources 1998, 72 (1).

[20] Kanamura, K., Hiroshi Tamura, Soshi Shiraishi, and Zen‐ichiro Takehara, XPS analysis of lithium surfaces following immersion in various solvents containing $LiBF_4$. Journal of the Electrochemical Society 1995, 142 (2).

[21] Lu, Y.; Tu, Z.; Shu, J.; Archer, L. A., Stable lithium electrodeposition in salt-reinforced electrolytes. Journal of Power Sources 2015, 279, 413-418.

[22] Lu, Y.; Tu, Z.; Archer, L. A., Stable lithium electrodeposition in liquid and nanoporous solid electrolytes. Nat Mater 2014, 13 (10), 961-9.

[23] Kim, H.; Wu, F.; Lee, J. T.; Nitta, N.; Lin, H.-T.; Oschatz, M.; Cho, W. I.; Kaskel, S.; Borodin, O.; Yushin, G., In Situ Formation of Protective Coatings on Sulfur Cathodes in Lithium Batteries with LiFSI-Based Organic Electrolytes. Advanced Energy Materials 2015, 5 (6), 1401792.

[24] Miao, R.; Yang, J.; Feng, X.; Jia, H.; Wang, J.; Nuli, Y., Novel dual-salts electrolyte solution for dendrite-free lithium-metal based rechargeable batteries with high cycle reversibility. Journal of Power Sources 2014, 271, 291-297.

[25] Zorba, V.; Syzdek, J.; Mao, X.; Russo, R. E.; Kostecki, R., Ultrafast laser induced breakdown spectroscopy of electrode/electrolyte interfaces. Applied Physics Letters 2012, 100 (23), 234101.

[26] Aurbach, D., Yair Ein‐Ely, and Arie Zaban, The surface chemistry of lithium electrodes in alkyl carbonate solutions. Journal of the Electrochemical Society 1994, 141 (1).

[27] Aurbach, D., Arie Zaban, Alexander Schechter, Yair Ein‐Eli, Ella Zinigrad, and Boris Markovsky, The study of electrolyte solutions based on ethylene and diethyl carbonates for rechargeable Li batteries I. Li metal anodes. Journal of the Electrochemical Society 1995, 142 (9).

[28] Aurbach, D., Yair Ein‐Eli, Boris Markovsky, Arie Zaban, S. Luski, Y. Carmeli, and H. Yamin, The study of electrolyte solutions based on ethylene and diethyl carbonates for rechargeable Li batteries II. Graphite electrodes. Journal of The Electrochemical Society 1995, 142 (9).

[29] Shin, H.; Park, J.; Han, S.; Sastry, A. M.; Lu, W., Component-/structure-dependent elasticity of solid electrolyte interphase layer in Li-ion batteries: Experimental and computational studies. Journal of Power Sources 2015, 277, 169-179.

[30] Zheng, J.; Zheng, H.; Wang, R.; Ben, L.; Lu, W.; Chen, L.; Chen, L.; Li, H., 3D visualization of inhomogeneous multi-layered structure and Young's modulus of the solid electrolyte interphase (SEI) on silicon anodes for lithium ion batteries. Phys Chem Chem Phys 2014, 16 (26), 13229-38.

[31] Tahir, A. M.; Janisch, R.; Hartmaier, A., Ab initiocalculation of traction separation laws for a grain boundary in molybdenum with segregated C impurites. Modelling and Simulation in Materials Science and Engineering 2013, 21 (7), 075005.

[32] G. Kresse, J. F. l., Efficient iterative schemes for ab initio total-energy calculations using a plane-wave basis set. PHYSICAL REVIEW B 1996, 54.

[33] Kresse, G.; Furthmüller, J., Efficient iterative schemes for ab initio total-energy calculations using a plane-wave basis set. Physical review B 1996, 54 (16), 11169.

[34] Perdew, J. P., Kieron Burke, and Matthias Ernzerhof, Generalized gradient approximation made simple. Physical review letters 1996, 77 (18).

[35] Tahir, A.; Janisch, R.; Hartmaier, A., Ab initio calculation of traction separation laws for a grain boundary in molybdenum with segregated C impurites. Modelling and Simulation in Materials Science and Engineering 2013, 21 (7), 075005.

[36] Jiang, Y.; Wei, Y.; Smith, J. R.; Hutchinson, J. W.; Evans, A. G., First principles based predictions of the toughness of a metal/oxide interface. International Journal of Materials Research 2010, 101 (1), 8-15.

[37] Liu, Z.; Qi, Y.; Lin, Y.; Chen, L.; Lu, P.; Chen, L., Interfacial study on solid electrolyte interphase at Li metal anode: implication for Li dendrite growth. Journal of The Electrochemical Society 2016, 163 (3), A592-A598.

SECTION

2. SUMMARIES AND CONCLUSIONS

This research focused on ALD coating material impact on Li ions intercalation mechanism of coated cathode particles, ALD coating material impact on the metal dissolution of cathode particles, ALD coating thickness impact on Li ions diffusivity in coated particles, and the interfacial property of SEI layer components via the first-principles study.

In Paper I, the study of amorphous Al_2O_3 and CeO_2-coated $LiMn_2O_4$ demonstrated sufficient reasoning behind the improved performance of CeO_2-coated active material over that of Al_2O_3-coated active material. In view of the lower formation energy of Li_xCeO_2 than that of $Li_xAl_2O_3$, Li ions can effortlessly intercalate into CeO_2 coating than Al_2O_3 coating. Considering the $LiMn_2O_4$ active material along with Al_2O_3 and CeO_2 coating layers, energy change during Li ion intercalation was calculated to find that two ions start to intercalate into $LiMn_2O_4$ after passing through Al_2O_3 and CeO_2 coating. However, there is barrier energy to overcome. Our finding shows that the barrier energy of Li ion transportation from CeO_2 coating to active material is lower than that of Al_2O_3 coating, suggesting easy intercalation of Li ions in $LiMn_2O_4$ from CeO_2 coating than Al_2O_3 coating. As a result, more Li ions stay behind in $LiMn_2O_4$ cathode when it is coated with the Al_2O_3 layer, leading to the volume expansion observed experimentally. Kinetically, Li ions in Li_xCeO_2 coating diffuse faster than in $Li_xAl_2O_3$ coating, resulting in better performance at the cell level. In summary, this work yielded a clear reason into why ALD coatings are beneficial to LIB and also gives evidence as to why CeO_2 ALD

coating has improved performance over other binary coating materials during the lithiation process from the fundamental study at the electronic level.

In Paper II, the Mn dissolution experiment was conducted. Surprisingly, we found that CeO_2 coating will intensify Mn dissolution. To study the fundamental metal dissolution mechanism, the first-principles calculation was performed via Manganese vacancy formation energy, COOP analysis, and PDOS analysis. Our work found that the formation energy of Al_2O_3/LMO is highest while CeO_2/LMO is lowest, which means CeO_2 coating will intensity Mn dissolution. This Mn vacancy formation energy is consistent with experimental results. The bonding length and the crystal orbital overlap population were calculated to examine the bonding strength of uncoated LMO, Al_2O_3 coated, and CeO_2 coated LMO. The projected density of state of Mn has also been calculated for uncoated, Al_2O_3 and CeO_2 coated LMO structure. The energy of CeO_2 coated LMO has a DOS peak at the lowest energy state and the energy of Al_2O_3/ LMO has a DOS peak at the highest energy state. Therefore, the CeO_2 coating may intensify Mn dissolution of LMO particles. The CeO_2 coating thickness impact on Mn dissolution has been investigated. We found that LMO particles will suffer more Mn dissolution with increasing CeO_2 coating. Finally, from cell-level, the discharge performance of U-LMO, A-LMO and C-LMO were studied at room temperature and elevated temperature. We found the Mn dissolution was intensified at high temperature, especially for CeO_2 coating.

In Paper III, we found that Li ions diffuse faster on LMO surface than in LMO bulk and Li ions diffuse faster in CeO_2 coating than in LMO active material. In addition, the Li diffusivity decreases with increasing crystal structure and remained at a relatively

constant value due to the bulk domination with thick CeO_2 coating, and that Li ions diffuse faster in amorphous CeO_2 coating with lower thicknesses than in crystal CeO_2 coated LMO. The relationship between ALD coating thickness, phase transition, and Li ion diffusivity is revealed in this work. It provides us a clue as to why Li diffusivity is improved via ALD coating on cathode particles in the lithium-ion battery from the atomic level.

Paper IV investigated the interfacial property of SEI layer components via first-principles calculation. The fracture strength of SEI layer components (such as LiF/Li_2CO_3, LiF/LiO, LiF/Li_2EC, and Li_2EC/Li_2EDC) was studied via traction-separation law. The interface between organic-inorganic components is unstable. The electronic property of SEI layer was investigated via DOS calculation. We found that the electron tunneling barrier of LiF/Li_2EC interface is the highest, while Li_2EC/Li_2EDC is the lowest. Thus, LiF/Li_2EC interface can block electrons transport effectively. This work revealed the interface stability of between different SEI components and showed the traction separation response of SEI components. The derived SEI layer traction-separation can be applied in continuum modeling of cohesive zones fracture.

APPENDIX A.

FIRST-PRINCIPLES STUDY OF ULTRATHIN FILM COATINGS ON CATHODE PARTICLES IN LITHIUM ION BATTERIES

Despite the periodic boundary conditions, the system size can affect the results. We have compared the system sizes of Li_xCeO_2 and $Li_xAl_2O_3$ to make sure the system size is sufficient. To find the minimum system size showing a converged energy, the unit sizes were changed and the convergence was checked. Amorphous Al_2O_3 with 2, 10, 20

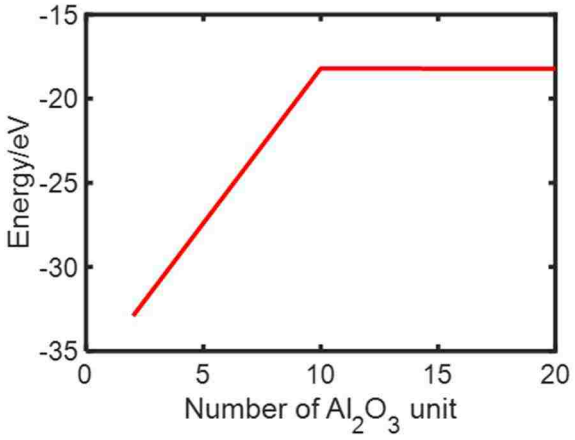

(A)

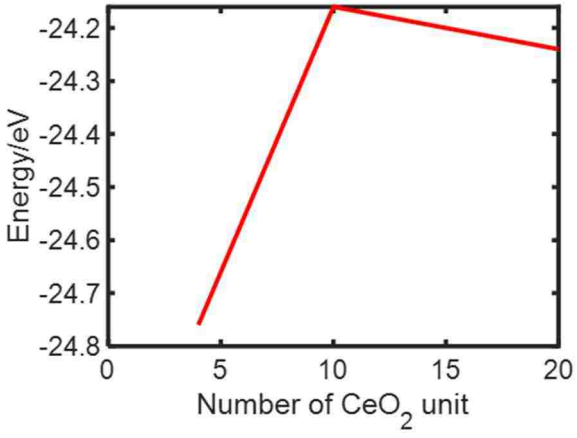

(B)

Figure S1. Energy convergence test of Al_2O_3 (A) and CeO_2 (B) coating.

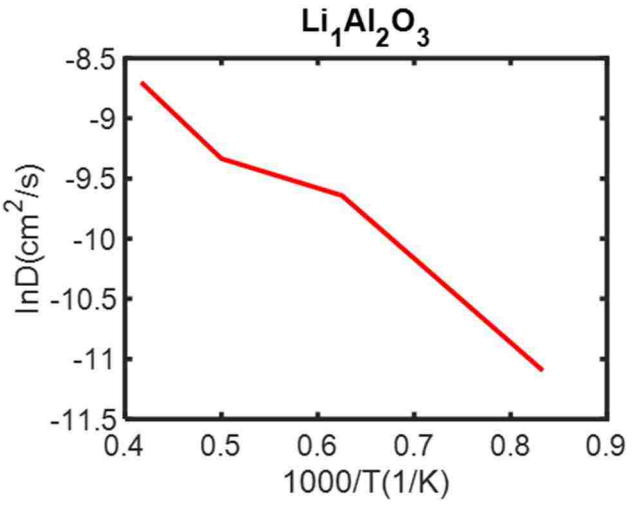

Figure S2. Li diffusivity of $Li_1Al_2O_3$ vs Temperature (1/T).

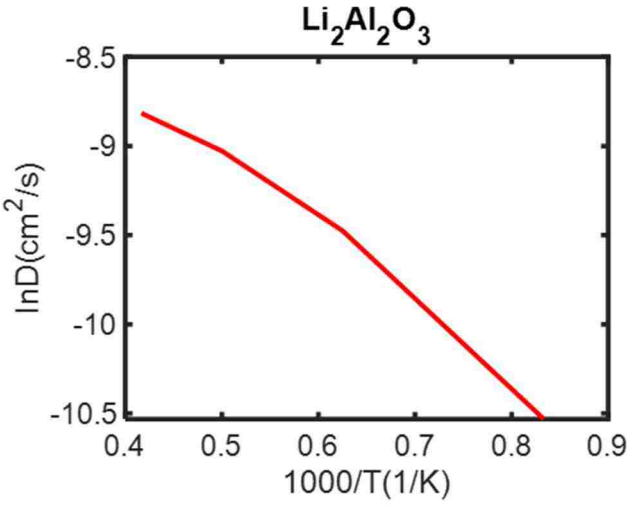

Figure S3. Li diffusivity of $Li_2Al_2O_3$ vs Temperature (1/T).

unit and amorphous CeO_2 with 4, 10, 20 unit were tested, which showed that 10 unit of Al_2O_3 and CeO_2 were enough to reach an energy convergence (Figure S1). Therefore,

10x Li, 20 Al and 30 O were distributed in initial $Li_xAl_2O_3$ structure and 10x Li, 10 Ce, and 20 O were distributed in initial Li_xCeO_2 structure.

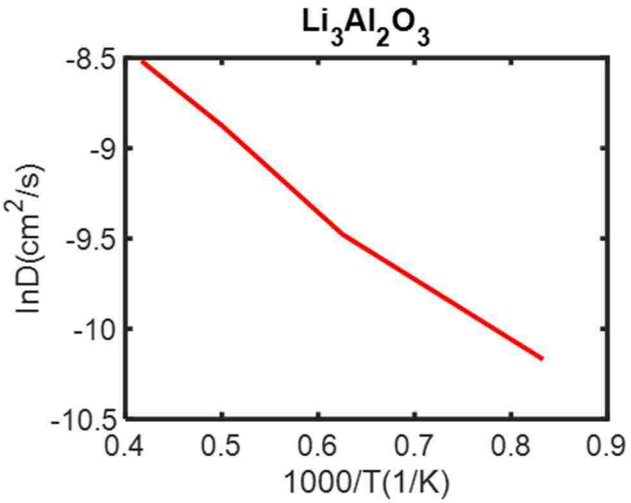

Figure S4. Li diffusivity of $Li_3Al_2O_3$ vs Temperature (1/T).

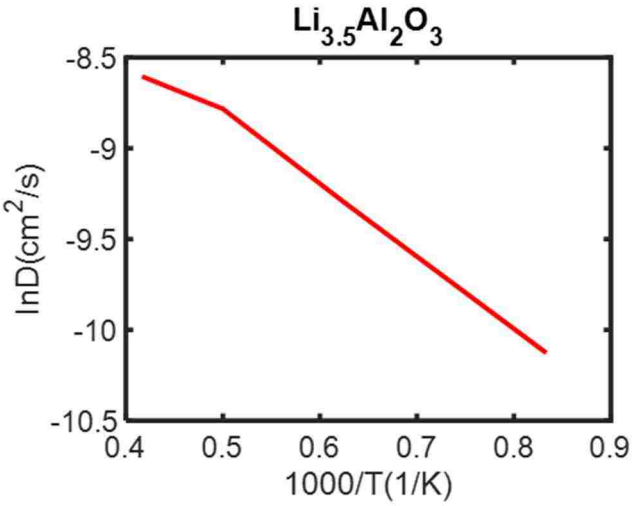

Figure S5. Li diffusivity of $Li_{3.5}Al_2O_3$ vs Temperature (1/T).

Li ion diffusivity in $Li_xAl_2O_3$ and Li_xCeO_2 coatings as a function of Li ion concentration (x= 1.0, 2.0, 3.0, 3.5, 4.0) was calculated. Li ion diffusion at different

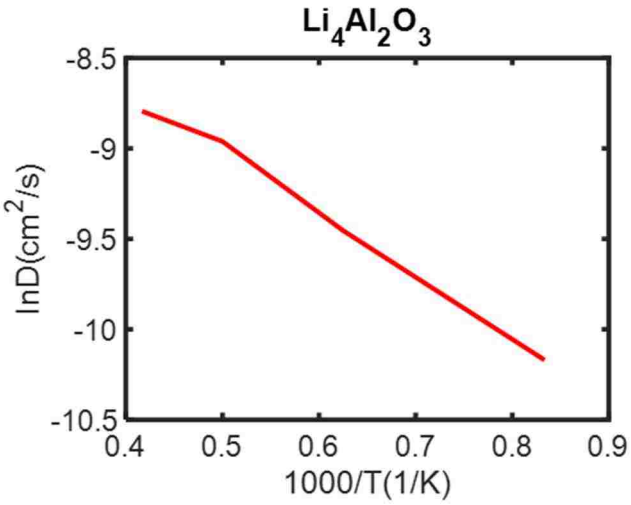

Figure S6. Li diffusivity of $Li_4Al_2O_3$ vs Temperature (1/T).

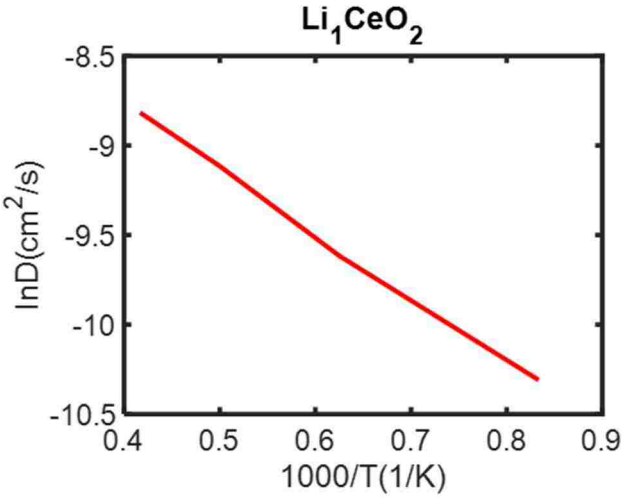

Figure S7. Li diffusivity of Li_1CeO_2 vs Temperature (1/T).

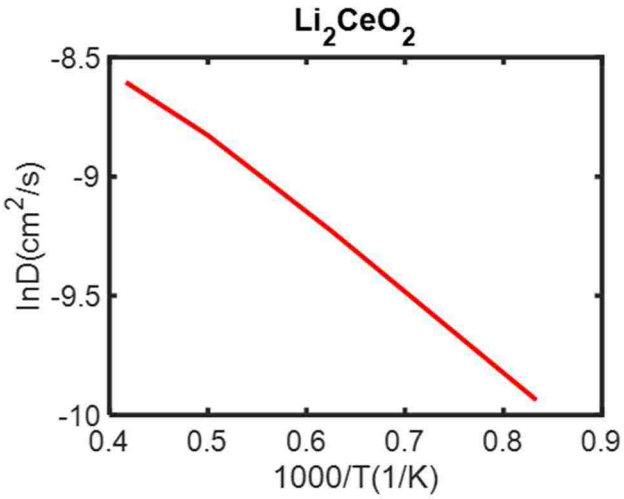

Figure S8. Li diffusivity of Li_2CeO_2 vs Temperature (1/T).

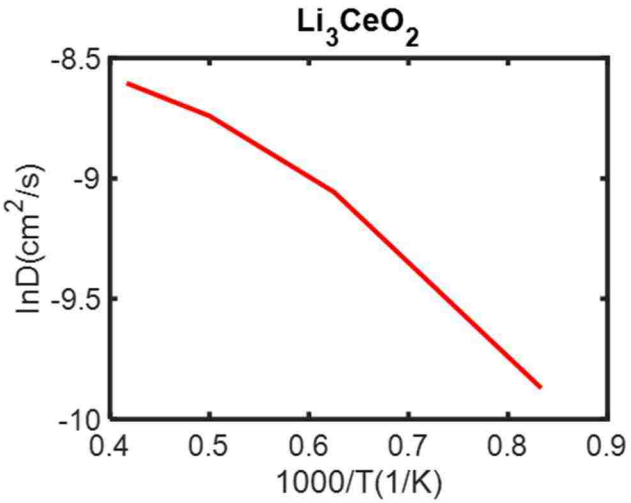

Figure S9. Li diffusivity of Li_3CeO_2 vs Temperature (1/T).

temperatures with different Li-ion concentrations for $Li_xAl_2O_3$ and Li_xCeO_2 are shown in Figure S2-11. Based on these results, the final diffusivity of $Li_xAl_2O_3$ and Li_xCeO_2 at 300K are shown in Table S1.

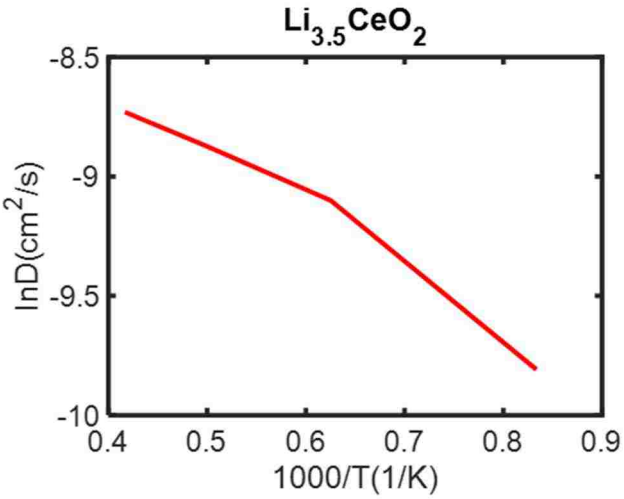

Figure S10. Li diffusivity of $Li_{3.5}CeO_2$ vs Temperature (1/T).

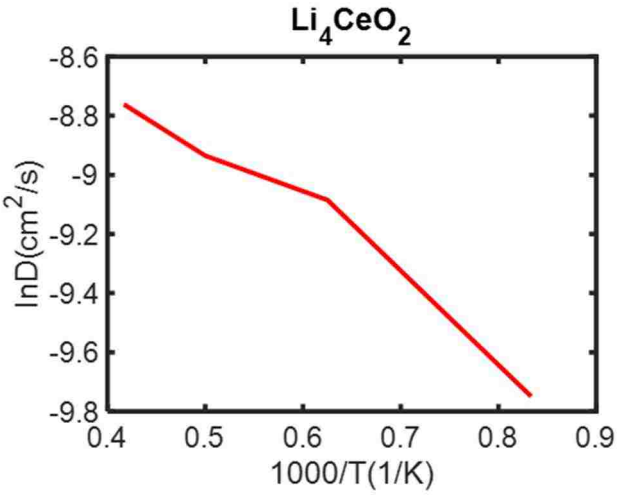

Figure S11. Li diffusivity of Li_4CeO_2 vs Temperature (1/T)

Table S1. The diffusion coefficient of $Li_xAl_2O_3$ at 300K (A); the diffusion coefficient of Li_xCeO_2 at 300K (B).

(A)

x	atom	D (cm^2/s)
1.0	Li	1.81E-11
2.0	Li	7.58E-10
3.0	Li	1.63E-09
3.5	Li	2.88E-09
4.0	Li	8.08E-09

(B)

x	atom	D (cm^2/s)
1.0	Li	4.15E-09
2.0	Li	1.74E-08
3.0	Li	2.43E-08
3.5	Li	8.62E-08
4.0	Li	2.12E-07

APPENDIX B.

DISCOVERY OF AN UNEXPECTED METAL DISSOLUTION OF THIN-COATED CATHODE PARTICLES AND ITS THEORETICAL EXPLANATION

The COOP values of Mn-Mn, Mn-Li are also inspected for U-LMO, A-LMO and C-LMO. The COOP values of Mn-Mn in C-LMO has more antibonding state and less bonding state than U-LMO and A-LMO (Fig. S1). The integrated COOP values of Mn-Mn of U-LMO and A-LMO are very close, while the ICOOP values of C-LMO is the lowest (Fig. S2). Also, the COOP values of Mn-Li in C-LMO has less bonding state and more antibonding state than that of U-LMO and A-LMO (Fig. S3). The integrated COOP values of Mn-Li in A-LMO is the strongest, while ICOOP values in C-LMO is the lowest (Fig. S4).

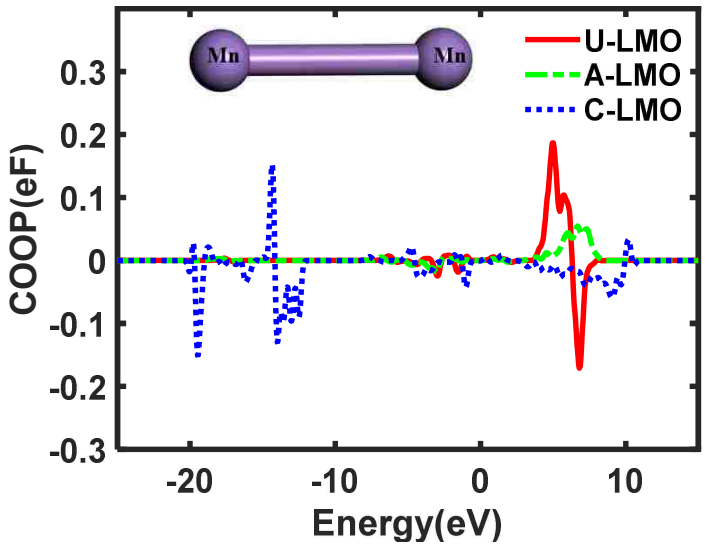

Figure S1. COOP (Crystal orbital overlap population) of Mn-Mn bond of uncoated LMO, Al_2O_3 coated LMO and CeO_2 coated LMO.

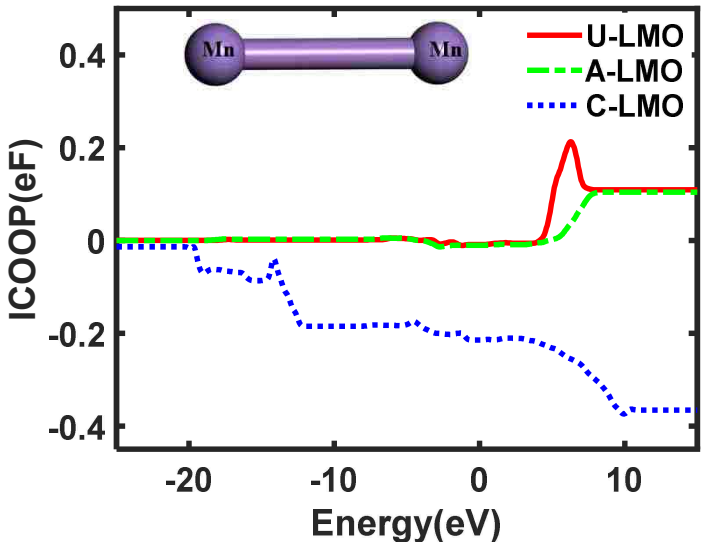

Figure S2. ICOOP (Integrated Crystal orbital overlap population) of Mn-Mn bond of uncoated LMO, Al_2O_3 coated LMO and CeO_2 coated LMO.

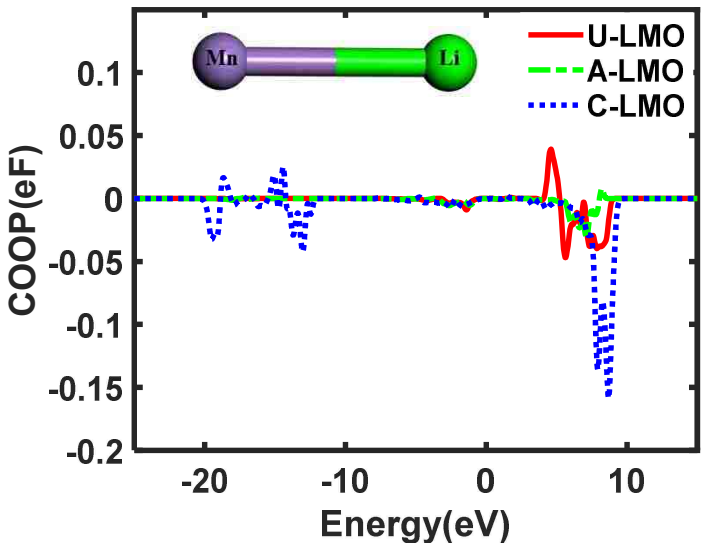

Figure S3. COOP (Crystal orbital overlap population) of Mn-Li bond of uncoated LMO, Al_2O_3 coated LMO and CeO_2 coated LMO.

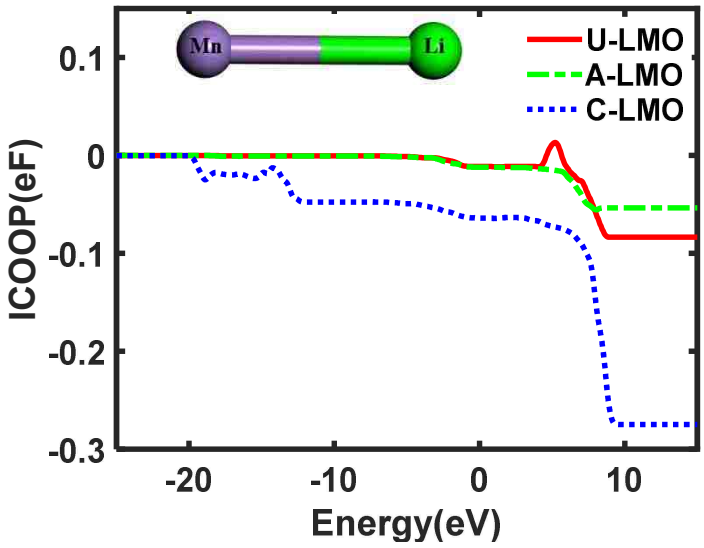

(B)

Figure S4. ICOOP (Integrated Crystal orbital overlap population) of Mn-Li bond of uncoated LMO, Al_2O_3 coated LMO and CeO_2 coated LMO.

The electronic property of Mn on U-LMO, A-LMO and C-LMO surface and bulk were compared. In e_g orbitals, the energy of Mn on U-LMO surface had a PDOS peak of around 4eV, the energy of Mn on A-LMO surface had a PDOS peak of around 4.25eV, while the energy of Mn on C-LMO surface had a PDOS peak of around 3.25eV above the Fermi level (Fig. S5). Besides, the energy of Mn on surface has lower PDOS peak than that of in bulk. In particular, the energy of Mn on C-LMO surface has much lower PDOS peak than that of Mn in C-LMO bulk, while the energy of Mn on surface of A-LMO is only slightly lower PDOS peak than that of Mn in A-LMO bulk (Fig. S5). Therefore, Mn ions on surface are more sensitive to ALD coating impact.

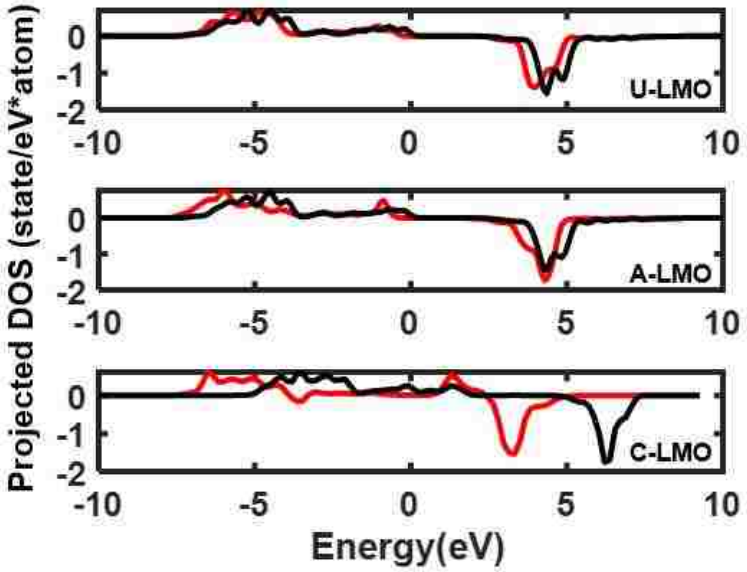

Figure S5. Projected density of state of Mn in uncoated LMO, Al_2O_3 coated LMO and CeO_2 coated LMO surface (red solid line) and bulk (black solid line) in e_g orbitals.

VITA

Yufang He was born in Hunan, China. She received her bachelor degree in Mechanical Engineering in 2015 from Beijing Technology and Business University, Beijing, P.R. China. She began her Ph.D. degree at Missouri University of Science and Technology in August 2015. She worked on Lithium ion battery performance improvement via first-principles calculation and experimental study. In December 2019, she received her Ph.D. degree in Mechanical Engineering from Missouri University of Science and Technology. After her graduation, she dedicated herself to the field of battery performance improvement.